Sede Amministrativa: Università degli Studi di Padova

Dipartimento di Ingegneria dell’Informazione

SCUOLA DI DOTTORATO DI RICERCA IN: **INGEGNERIA DELL’INFORMAZIONE**

INDIRIZZO: **SCIENZA E TECNOLOGIA DELL’INFORMAZIONE**

CICLO **XXVII**

RELIABILTIY OF DEVICES AND TECHNOLOGIES FOR SOLID-STATE LIGHTING

Direttore della Scuola: Ch.mo Prof. Matteo Bertocco

Coordinatore d’indirizzo: Ch.mo Prof. Carlo Ferrari

Supervisore: Ch.mo Prof. Enrico Zanoni

Dottorando: Matteo Dal Lago

Contents

Abstract 4
Sommario 6
List of publications 8
International journal papers 8
Papers on international conference proceedings 9
Other publications 10
Introduction 11
Chapter 1: LED basics 14
1.1 History 14
1.2 Physical mechanisms 16
1.2.1 Electrons and holes recombinations 17
1.2.2 Radiative recombination and absorption 17
1.2.3 Non-radiative recombination in the bulk 20
1.3 LED die structures 24
1.3.1 Homojunction LEDs 24
1.3.2 Heterojunction LEDs 25
1.3.3 Quantum well structures 33
1.4 Electrical properties of LEDs 35
1.4.1 Current-voltage (I-V) characteristic 36
1.4.2 Deviations from the ideal current-voltage characteristic 38
1.4.3 Temperature dependence of I-V characteristic 44
1.5 LED packaging 46
1.5.1 SMD LEDs 48
1.5.2 Chip-on-board (COB) modules 51
Chapter 2: LED metrology 53
2.1 Human vision 53
2.2 Photometry 54
2.3 Colorimetry 56
2.4 Color rendering 57
2.4.1 Metamerism 57
2.4.2 CIE Color Rendering Index (CRI) 57
2.4.3 The CRI problems and the Color Quality Scale 59
2.4.4 Recent studies 60
Chapter 3: LED reliability 61
3.1 Generation of non-radiative defects 62
3.2 Degradation of the ohmic contacts 64

3.3 Changes in the optical properties of the encapsulant material 66
3.4 Chemical compatibility 68
3.5 Degradation of the phosphorus encapsulant 70
Chapter 4: "Hot-plug" on LED modules 72
4.1 Introduction on the "Hot-plug" phenomenon 72
4.2 Experimental details 73
4.3 Current waveform analysis 74
4.4 Modelization and simulation 78
4.5 "Hot-plugging" with discrete components 80
4.6 Discussion and conclusions 81
Chapter 5: ESD on GaN-based monochromatic LEDs 83
5.1 Introduction 83
5.2 Experimental details 84
5.3 Results on BLUE LEDs (Type A) 85
5.4 Results on GREEN LEDs (Type B) 89
5.5 Discussion and conclusion 91
Chapter 6: Reliability of Remote Phosphor Light Sources 92
6.1 Introduction 92
6.2 Experimental details 94
6.3 Results 94
6.3.1 Thermal characterization 94
6.3.2 Degradation tests 96
6.4 Discussions and conclusions 101
References 102

Abstract

The role of high-power white LEDs in general lighting applications is becoming, day-by-day, increasingly important. The reliability of these devices, compared to that of conventional light sources, represents one of the keys for their development and their market penetration. It is then of fundamental importance to deeply understand the various degradation mechanisms that affect the operation of LEDs, in terms of lifetime, chromaticity characteristics and efficiency. This thesis reports the results of a research activity focused on several issues related to the reliability of LED-based lighting systems.

After an initial overview on the most important theoretical concepts necessary for the understanding of the physical results, three main sections can be identified in this thesis, concerning the presentation of research activity:

- The first section reports an extensive study on one of the most critical Electrical Over Stress (EOS) phenomena, called "Hot-plugging", which occurs when an LED module is directly connected to an energized power supply and can generate current spikes up to several tens of amperes that can potentially destroy or damage the LEDs. The aim of this section is to analyze, for the first time, the nature of the current spikes generated during hot-plugging and to present a simplified model to explain the hot plugging phenomenon. The study is based on transient electrical measurements, carried out on several LED modules (fabricated by different manufacturers), connected to three different power supplies. Results reveal that the amplitude and the time constants of the current spikes are directly determined by the number of LEDs connected in series and by the output capacitance of the current driver.
- Afterwards, the second section presents an extensive study on the effects of Electrostatic Discharges (ESD) on state-of-the-art GaN based LEDs, based on optical and electrical measurements carried out during the ESD events. ESD events were simulated through a Transmission Line Pulser (TLP), which generates voltage pulses with a duration of 100ns and increasing amplitude: during each pulse, spatially resolved electroluminescence measurements were carried out through a high speed EMCCD camera. These measurements allowed to identify the chip region where the discharge is localized and the change in the damaged area induced by consecutive ESD events. In addition, the current and voltage waveforms at the LED terminal were monitored during the tests; this analysis provided

important information about modifications the impedance of the devices. The analysis was carried out on different types of commercially available low-power GaN-based LEDs with several differences in the manufacturing technology. Thanks to these tests, we have identified two different failure behaviors during a destructive ESD event, clearly related to the different defects in the semiconductor lattice and to structure of the chip.

- The last section investigates the thermal stability of remote phosphor plates to be used in solid-state lighting systems, for the conversion of the blue light emitted by GaN-based LEDs into white light. A preliminary thermal characterization revealed that in normal conditions of blue light irradiance the phosphor plates could reach temperature levels higher than 60°C, which can affect both performance and reliability. The results of accelerated thermal stress tests indicate that high temperature levels can trigger a relevant degradation mechanism (estimated activation energy is 1.2 eV), that drastically reduces the phosphor conversion efficiency and modifies the photometric and colorimetric characteristics of the emitted white light.

Sommario

Il ruolo dei LED bianchi di potenza sta diventando, giorno dopo giorno, sempre più importante. L’affidabilità di questi dispositivi, paragonata a quella delle sorgenti di luce tradizionali, rappresenta uno dei fattori chiave per il loro sviluppo e la loro penetrazione nel mercato. E’ quindi di fondamentale importanza conoscere in modo approfondito i diversi meccanismi di degrado che possono influenzarne il funzionamento in termini di tempo di vita, caratteristiche cromatiche ed efficienza. Questa tesi riporta i risultati di un’attività di ricerca incentrata su alcune problematiche relative all’affidabilità di sistemi illuminazione allo stato solido.

Dopo una panoramica iniziale sui concetti teorici necessari per comprendere appieno i risultati, in questa tesi possono essere indentificate tre diverse sezioni che presentano l’attività di ricerca del dottorato:

- la prima parte riporta uno studio estensivo su uno dei più critici fenomeni di Electrical Over Stress (EOS), chiamato “Hot-Plugging”, che accade quando un modulo LED è direttamente connesso ad un driver LED precedentemente alimentato e può generare picchi di corrente fino ad alcune decine di ampere, che possono potenzialmente distruggere o danneggiare i LED. Lo scopo di questa sezione è analizzare, per la prima volta, la natura dei picchi di corrente generati durante l’“hot-plugging” e proporre un modello semplificato per spiegare il fenomeno. Lo studio è basato sulla misura dei transienti elettrici, svolta su diversi moduli LED (scelti tra diversi produttori), connessi a tre diversi tipi di alimentatori. I risultati rivelano che l’ampiezza e le costanti di tempo dei picchi di corrente sono direttamente determinate dal numero di LED connessi in serie e dalla capacità di uscita dell’alimentatori;

- la seconda parte presenta un completo studio sugli effetti delle scariche elettrostatiche (ESD) su LED al Nitruro di Gallio (GaN), basato su misure elettriche e ottiche svolte durante l’evento ESD. Le scariche elettrostatiche sono state simulate tramite un Transmission Line Pulser (TLP) che genera impulsi di tensione con una durata di 100 ns e ampiezza crescente: durante ciascun impulso sono state svolte misure di elettroluminescenza grazie ad una camera EMCCD (Electon Multiplying Charge Coupled Device) ad alta velocità. Queste misure permettono di identificare la regione del chip dove la scarica è localizzata e i cambiamenti nell’area danneggiata indotti da eventi ESD consecutivi. Inoltre, le forme d’onda di corrente e tensione ai terminali del LED sono state monitorate durante i test; tale analisi fornisce importanti informazioni circa le modifiche di impedenza dei dispositivi.

L’analisi è stata svolta su diversi tipi di LED commerciali a media potenza con alcune differenze nelle tecnologie di fabbricazione. Grazie a questi test sono stati indentificati due differenti comportamenti di failure durante eventi ESD distruttivi, chiaramente correlati ai diversi difetti nel cristallo del semiconduttore e alla struttura del chip;

- l’ultima sezione riporta uno studio sulla stabilità termica di piastre di “fosfori remoti” usate in sistemi di illuminazione allo stato solido per convertire la luce blu generata dai LED in luce bianca. Una caratterizzazione termica preliminare rivela che, in normali condizioni operative sotto illuminazione a luce blu, la piastra di fosfori può raggiungere temperature fino a 60°C, che possono influenzarne sia le performance che l’affidabilità. I risultati di stress termici accelerati indica che alti livelli di temperatura possono condurre ad un rilevante meccanismo di degrado (l’energia di attivazione stimata è 1.2 eV), che riduce drasticamente l’efficienza di conversione fosforosa e modifica le caratteristiche fotometriche e colorimetriche della luce bianca emessa.

List of publications

International journal papers

M. Dal Lago, M. Meneghini, C. De Santi, M. Barbato, N. Trivellin, G. Meneghesso, E. Zanoni; "ESD on GaN-based LEDs: an analysis based on dynamic electroluminescence measurements and current waveforms" Microelectronics Reliability, accepted for publication

M. Meneghini, S. Vaccari, **M. Dal Lago**, S. Marconi, M. Barbato, N. Trivellin, A. Griffoni, A. Alfier, G. Verzellesi, G. Meneghesso, E. Zanoni, ESD degradation and robustness of RGB LEDs and modules: An investigation based on combined electrical and optical measurements, Microelectronics Reliability, Volume 54, Issues 6–7, June–July 2014, Pages 1143-1

M. Meneghini, **M. Dal Lago**, N. Trivellin, G. Meneghesso and E. Zanoni; "Degradation mechanisms of high power LEDs for lighting applications: an overview", Industry Applications, IEEE Transactions on , vol.50, no.1, pp.78,85, Jan.-Feb. 2014 doi: 10.1109/TIA.2013.2268049

M. Dal Lago, M. Meneghini, N. Trivellin, G. Mura, M. Vanzi, G. Meneghesso, E. Zanoni, *""Hot-plugging" of LED-modules: electrical characterization and device degradation"*, Microelectronics Reliability, Volume 53, Issues 9–11, September–November 2013, Pages 1524-1528, ISSN 0026-2714, http://dx.doi.org/10.1016/j.microrel.2013.07.054.

M. Meneghini, **M. Dal Lago**, N. Trivellin, G. Meneghesso and E. Zanoni; "Thermally-activated degradation of remote phosphors for application in LED lighting," *IEEE Transactions on Device and Materials Reliability,* vol.PP,no.99,pp.1,0 doi: 10.1109/TDMR.2012.2214780

M. Dal Lago, M. Meneghini, N. Trivellin, G. Mura, M. Vanzi, G. Meneghesso, E. Zanoni, *"Phosphors for LED-based light sources: thermal properties and reliability issues"*, Microelectronics Reliability, Volume 52, Issues 9–10, September–October 2012, Pages 2164-2167, ISSN 0026-2714, 10.1016/j.microrel.2012.06.036.

M. Meneghini, **M. Dal Lago**, L. Rodighiero, N. Trivellin, G. Meneghesso, E. Zanoni , *"Reliability issues in GaN-Based Light-Emitting Diodes: effect of dc and PWM stress"*, Microelectronics Reliability, Volume 52, Issue 8, August 2012, Pages 1621-1626, ISSN 0026-2714, 10.1016/j.microrel.2011.10.012.

M. Dal Lago, M. Meneghini, N. Trivellin, G. Meneghesso and E. Zanoni, *"Degradation mechanisms of high-power white LEDs activated by current and temperature"*, Microelectronics Reliability, Volume 51, Issues 9–11, September–November 2011, Pages 1742-1746, ISSN 0026-2714, 10.1016/j.microrel.2011.06.057.

M. Meneghini, **M. Dal Lago**, N. Trivellin, G. Mura, M. Vanzi, G. Meneghesso and E. Zanoni, *“Chip and package-related degradation of high power white LEDs”* Microelectronics Reliability, Volume 52, Issue 5, May 2012, Pages 804-812, ISSN 0026-2714, 10.1016/j.microrel.2011.07.091.

Papers on international conference proceedings

Zanoni, E.; Meneghini, M.; Trivellin, N.; **Dal Lago, M.**; Meneghesso, G., *"GaN-based LEDs: State of the art and reliability-limiting mechanism,"* Thermal, mechanical and multi-physics simulation and experiments in microelectronics and microsystems (eurosime), 2014 15th international conference on , vol., no., pp.1,5, 7-9 April 2014 doi: 10.1109/EuroSimE.2014.6813878149, ISSN 0026-2714

N.Trivellin , M. Meneghini , M. Ferretti , D. Barbisan , **M. Dal Lago** , G. Meneghesso , E. Zanoni; *“Thermal, optical, and electrical engineering of an innovative tunable white LED light engine”*. Proc. SPIE 9003, 90031B (February 27, 2014); doi:10.1117/12.2040599.

N.Trivellin, M. Meneghini, **M. Dal Lago**, Diego Barbisan, Marco Ferretti, G. Meneghesso, E. Zanoni *“Characterization and endurance study of aluminate/silicate/garnet/nitride phosphors for high-performance SSL*” Proc. SPIE, 4-7 February 2013

N.Trivellin, M. Meneghini, **M. Dal Lago**, G. Meneghesso, E. Zanoni, *“Innovative methodology for testing the reliability of LED based systems”*, Proc. SPIE Vol. 8278, 82780W, 2012

M. Dal Lago, M. Meneghini, N. Trivellin, G. Meneghesso and E. Zanoni, *“The role of operating conditions in the chip-level degradation of white LEDs”,* presented at 35th Workshop on Compound Semiconductor Devices and Integrated Circuits, WOCSDICE 2011, June 2011, Catania, Italy, ISBN: 978-88-8080-123-8

M.Meneghini, A. Tazzoli, N. Trivellin, E. Ranzato, **M. Dal Lago**, B. Hahn, U. Zehnder, R. Butendeich, G. Meneghesso, and E. Zanoni, *“A study on the reverse-bias and ESD instabilities of InGaN-based green LEDs”*, Proc. SPIE Vol. 7617, 76170M, 2010

M.Meneghini, G. Mura, **M. Dal Lago**, L. Rodighiero, M. Vanzi, G. Meneghesso, and E. Zanoni, *“Degradation Mechanisms of white LEDs for lighting applications”*, presented at 2nd International Symposium on Reliability of Optoelectronics for Space, ISROS-2010, April 28-30 2010, Cagliari, Italy

N.Trivellin, M. Meneghini, **M. Dal Lago**, G. Meneghesso, L. Rodighiero, G. Mura, M. Vanzi, E. Zanoni, *“Effects of Electro-Thermal stress on AlGaN deep-ultraviolet LEDs”,* presented at European Workshop on Heterostructure Technology, HeTech 2009, Ulm, Germany

Other publications

"Percezione della luce, confort visivo e aspetti tecnologici dei LED"; M.Meneghini, N. Trivellin, **M. Dal Lago**, D. Barbisan, G.Meneghesso, E. Zanoni; Luce&Design, Aprile '14

"Efficienza luminosa e affidabilità dei sistemi LED"; M.Meneghini, N. Trivellin, **M. Dal Lago**, D. Barbisan, G.Meneghesso, E. Zanoni; Luce&Design, Novembre '13

"Reliability oriented design of LED-based light sources"; **M. Dal Lago**, M.Meneghini, N. Trivellin, G.Meneghesso, E. Zanoni; LED Professional Review, Sept/Oct 2013, Issue 39, ISSN 1993-890X

"Considerazioni di mercato per l'illuminazione LED"; M.Meneghini, N. Trivellin, **M. Dal Lago**, D. Barbisan, G.Meneghesso, E. Zanoni; Luce&Design, Settembre '13

"Soluzioni innovative per il miglioramento delle caratteristiche prestazional dei sistemi LED"; M.Meneghini, N. Trivellin, **M. Dal Lago**, D. Barbisan, G.Meneghesso, E. Zanoni; Luce&Design, Aprile '13

"Degradation mechanisms of high power LEDs", M.Meneghini, , **M. Dal Lago**, N. Trivellin, G.Meneghesso, E. Zanoni; LED Professional Symposium 2013 Booklet

Introduction

This thesis reports the main results obtained from the Ph.D. research activity of the candidate. The activity was focused on the study the physical mechanisms that limit the reliability of LED-based lighting technologies. A solid-state light source is a complex system that integrates electronic components, mechanical interfaces, optical structures and, then, there are many different issues that can limit the reliability of these devices. During the last years, the Gallium Nitride fabrication technology has made great progress in term of robustness of the LED chip in harsh operating condition, thanks to improved thermal performances, reduced lattice defectiveness and improved packaging materials. Despite this, lamp manufacturer are still complaining the premature failure of LED devices and the degradation of the optical performances during the light source lifetime.

Up to now, some of the most common failure causes in solid-state lighting can be ascribed to Electrical Overstresses (EOS) or Electrostatic Discharges (ESD) events. ESD and EOS are related types of over stress events but at opposite ends of a continuum of current/voltage/time stress conditions:

- ESD is a very high voltage (generally >500V) and moderate peak current(~1A to 10A) event that occurs in a short time frame (generally <1µs);
- EOS is a lower voltage (<100V) and large peak current (>10A) event that occurs over longer time frame (generally >1ms).

EOS is a very broad concept and can have many different sources, including power-on and power-off transients, inrush current, and excessive voltages or currents (in the case of LEDs, this is commonly known as overdriving). Power-on and power-off transients – also called spikes – can come from the driver of an LED circuit or system. In applications with discrete control, spikes can be generated near to the location of the

LED circuit and can be coupled in via wiring harnesses, for example. Moreover, the wiring between the driver and the LED mount can be a source of spikes. These transients can be significant and are capable of causing damage depending on the driver topology, type of protection used in the system,

and the power level. In this context, slow regulated or inadequate power supplies are also a sensitive issue. In the case of LEDs, inrush current is most common if LEDs are connected to an energized power supply, known as "hot plugging" in the electronic industry. The large amount of current that can flow during hot plugging constitutes an EOS event and can cause serious damage as extensively explained in Chapter 4.

One of the causes of ESD events is static electricity. Static electricity is often generated through tribocharging, the separation of electric charges that occurs when two materials are brought into contact and then separated. Examples of tribocharging include walking on a rug, descending from a car, or removing some types of plastic packaging. In all these cases, the friction between two materials results in tribocharging, thus creating a difference of electrical potential that can lead to an ESD event.

Another cause of ESD damage is through electrostatic induction. This occurs when an electrically charged object is placed near a conductive object isolated from ground. The presence of the charged object creates an electrostatic field that causes electrical charges on the surface of the other object to redistribute. Even though the net electrostatic charge of the object has not changed, it now has regions of excess positive and negative charges. An ESD event may occur when the object comes into contact with a conductive path. For example, charged regions on the surfaces of styrofoam cups or plastic bags can induce potential on nearby ESD sensitive components via electrostatic induction and an ESD event may occur if the component is touched with a metallic tool. It is then understandable that each LED is potentially exposed to Electrostatic discharges throughout all its lifetime, starting from the manufacturing and assembly process, to real-life operation; such ESD can lead to the catastrophic failure of the devices. Chapter 5 presents an innovative methodology to analyze the ESD failure of LEDs, based on dynamic measurements of the Electroluminescence (EL) and of current/voltage waveforms of the devices executed during the ESD event.

At the end of this thesis, Chapter 6 presents an extensive study on the reliability of light sources based on the Remote-Phosphor technology. This light source configuration has recently emerged as a viable alternative to standard chip-level conversion, for the realization of high efficiency LED-based light sources. In fact, remote phosphor approach guarantees a good extraction efficiency, a reduction of the self-heating of the phosphor layer (with consequent performance improvement), and a better diffusion of the emitted light.

Despite the excellent potential of remote phosphors, their reliability can be limited by a number of factors: the high power densities reachable by the modern power-LED modules can lead to an important temperature increase on the remote-phosphor layer, thus inducing a thermal degradation.

Environmental conditions (such as humidity and chemical interactions) can also compromise the optical characteristics of the phosphor plates. The analysis is based on the optical and thermal characterization of a number of remote-phosphor samples, which were submitted to accelerated thermal stress tests with the aim of understand the effects of operating at high temperature levels to the phosphor conversion efficiency.

Chapter 1: LED basics

1.1 History

The story of solid-state lighting start in the mid 1920s, when a young Russian scientist named Oleg Vladimirovich Losev, observed light emission from zinc oxide and silicon carbide crystal rectifier diodes used in radio receivers when a current was passed through them. Losev's first paper on the emission of silicon carbide diodes, entitled “Luminous carborundum detector and detection effect and oscillations with crystals.” was published in 1927. In the 16 papers published between 1924 and 1930, he provided a comprehensive study of the LED and outlined its applications. Losev understood the “cold” (non-thermal) nature of the emission, measured its current threshold, recognized that LED emission is related to diode action and measured the current-voltage characteristics of the device in details. In 1961, Bob Biard and Gary Pittman were working together on a project for Texas Instruments to develop gallium arsenide (GaAs) diodes. Using an infrared microscope, they found that these diodes emitted significant light in the infrared region. The first practical visible-spectrum (red) LED was developed in 1962 by Nick Holonyak Jr., while working at General Electric Company. Up to 1968 visible and infrared LEDs were extremely costly, in the order of US $200 per unit, and so had little practical application. The Monsanto Company was the first organization to mass-produce visible LEDs, using gallium arsenide phosphide in 1968 to produce red LEDs suitable for indicators. Hewlett Packard (HP) introduced LEDs in 1968, initially using GaAsP supplied by Monsanto. The technology proved to have major applications for alphanumeric displays and was integrated into HP's early handheld calculators. The first GaN LED was made in 1971 by a team at the laboratories of the Radio Corporation of America (RCA), which included Herb Maruska, Jacques Pankove and Ed Miller. This device employed a metal-insulator-semiconductor structure, and its incredibly low efficiencies prevented it from ever being a commercial success. After the research efforts of Maruska and co-workers had ended, work on GaN virtually ceased. In 1982 only a single paper was published on GaN. However, Isamu Akasaki and co-worker in Nagoya, Japan, refused to give up, and in 1989

they demonstrated the first true p-type doping and p-type conductivity in GaN. Subsequent to the attainment of p-type doping, the first GaN p-n-homojunction LED was reported by Akasaki et al. (1992). The LED that emitted light in the ultraviolet and blue spectral range was grown on a sapphire substrate and had an efficiency of approximately 1%. This was a surprisingly high value for the highly dislocated GaN material grown on the mismatched sapphire substrate. It was also the first demonstration that nitride LED efficiencies are not affected by dislocations in the same adverse manner as III-V arsenide and phosphide light emitters. At this time, Shuji Nakamura began development of a blue light emitting semiconductor device at Nichia Chemical Industries, in 1988. Nakamura had the confidence and engineering creativity to solve the technical problems stemming from GaN-based research. He began his experiment to make GaN thin film using standard equipment with a well-known substrate material, sapphire, and a well-known method, MOCVD. Nakamura repeatedly modified the MOCVD equipment by himself to change the gas flow mode, and performed experiments over 500 times in a short period. Finally, he found the most appropriate method where the main material gases, including Ga compound, flow in parallel to the substrate, and nitrogen and hydrogen are supplied vertically from the upper side to the substrate surface. In 1991, he succeeded in fabricating a GaN thin film with superior uniformity using this method, which he named the "two-flow method". Moreover, in 1992, he achieved high quality InGaN ternary compound thin film by the two-flow method. This film was necessary to optimize the emitted light wavelength and to improve the emission efficiency. In order to fabricate the p-type GaN layer, Nakamura investigated another more practical method than that with electron irradiation studied by Akasaki and Amano. Heat treatment, using a specimen doped with magnesium as the acceptor impurity, had been studied but had proven unsuccessful. Nakamura reexamined the heat treatment effect and found that a hydrogen-free atmosphere was essential to activate the doped magnesium and get the p-type layer. He clarified the mechanism of p-type formation, proposing a model based on the connection between hydrogen atoms and acceptor impurities. Using the abovementioned technologies, Nakamura fabricated p-n homo-junction blue LEDs with 0.18% light emitting efficiency and the double heterostructure type with 0.22 % light emitting efficiency in 1992. The latter one was improved to 2.7 % light emitting efficiency using the above-mentioned InGaN thin film as the light emitting layer, in 1993. Based on these results, Nichia Chemical Industries delivered the world's first high-brightness blue LEDs in 1993.

1.2 Physical mechanisms

The basic mechanism by which LEDs produce light can be summarized, however, by a simple conceptual description. The familiar light bulb relies upon temperature to emit visible light (and significantly more invisible radiation in the form of heat) through a process known as incandescence. In contrast, the light emitting diode employs a form of electroluminescence, which results from the electronic excitation of a semiconductor material. The basic LED consists of a junction between two different semiconductor materials, in which an applied voltage produces a current flow, accompanied by the emission of light when charge carriers injected across the junction are recombined. One of the two semiconductor regions that comprise the junction in the chip is dominated by negative charges (n-type region; Figure 1), and the other is dominated by positive charges (p-type region). When a sufficient voltage is applied to the electrical leads, current flows and electrons move across the junction from the n region into the p region where the negatively charged electrons combine with positive charges. Each combination of charges is associated with an energy level reduction that may release a quantum of electromagnetic energy in the form of a light photon. The frequency, and perceived color, of emitted photons is characteristic of the semiconductor material, and consequently, different colors are achieved by making changes in the semiconductor composition of the chip.

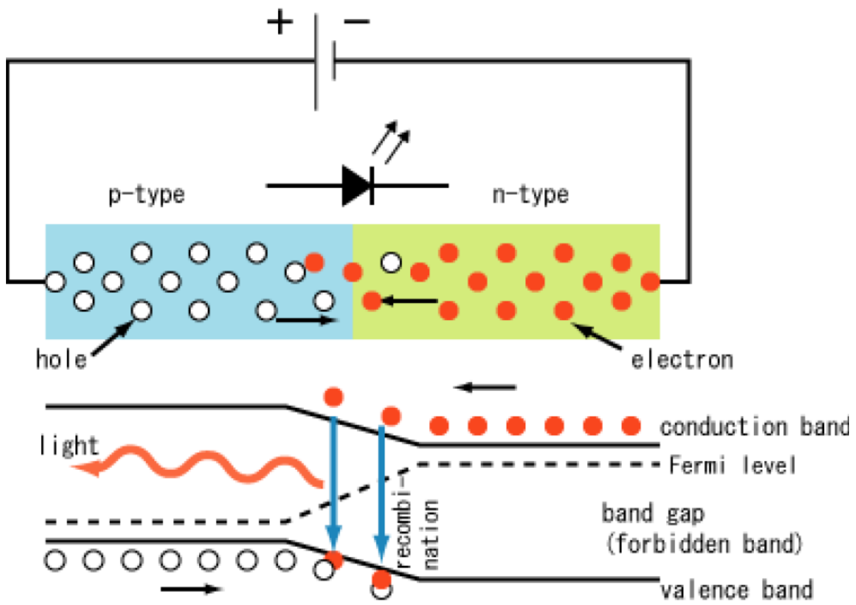

Figure 1: Simplified diagram of carrier flowing and photon generation on a biased p-n junction

1.2.1 Electrons and holes recombinations

There are several ways for producing light; an incandescent bulb for example is based on light emission from an electrically heated metal (Tungsten). Solid-state lighting is based on a much more efficient process, radiative electron hole recombination. In every semiconductor, two antagonist phenomena take place: generation and recombination of electron and hole pairs (EHP). Excess carriers can be generated by either absorption of light (with a greater energy than band-gap energy) or by injected current. During recombination electron and hole, recombine through the band-gap an energy with the band-gap value is released. There are two basic recombination mechanisms in semiconductors, radiative and non-radiative recombination. In a radiative event, one photon with energy equal to the band-gap energy of the semiconductor is emitted, while during non-radiative recombination, the electron energy is converted to vibrational energy of lattice atoms, emitting a phonon. Thus, the energy is converted in heat. In semiconductor, generally two different types of non-radiative recombination take place:

- Non-radiative recombination in the bulk due to deep level defects and auger recombination.
- Non-radiative recombination at surface.

1.2.2 Radiative recombination and absorption

Radiative recombination is based on two different mechanisms: spontaneous emission and stimulated emission. Absorption is instead the opposite mechanism, in which a photon is absorbed generating an EHP.

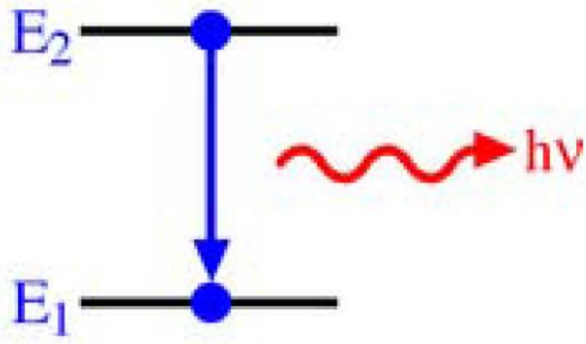

Figure 2: Spontaneous emission

Spontaneous emission

If a light radiation with a greater energy than band-gap energy hits a semiconductor, then electron from valence band will be excited and moved to conduction band, thus generating an EHP. This phenomenon is called absorption, or pumping for a laser. The excited electron will, in a time indicated as lifetime, recombine with a hole and emit a photon with a fixed wavelength. The wavelength value varies with the type of semiconductor band-gap:

$$\lambda_d = \frac{hc}{E_g} \approx \frac{1.24}{E_g} \; ; \; \lambda_i = \frac{hc}{E_g - E_{phonon}} \approx \frac{1.24}{E_g - E_{phonon}}$$

respectively in direct and indirect band-gap. Observing the emitted spectrum will reveal that the emission is not purely monochromatic, but has a spread due to distribution of electrons and holes in conduction and valence band, and by thermal agitation. Some other wavelength will be also present, caused by recombination through defect or impurity acting like transition levels inside band-gap. The phase and direction of the emitted light is random, typical of a LED. It is now possible to evaluate the spontaneous emission rate, proportional to electrons and holes density: $R_{sp} = B_{sp}np$ where B_{sp} is the spontaneous emission coefficient. Considering n_0 and p_0 intrinsic concentration of electron and holes, and n’ and p’ concentration of free carriers injected in the region, we can conclude that the actual densities of electrons and holes are respectively:

$$n = n_0 + n'; p = p_0 + p'$$

Then:

$$R_{sp} = B_{sp}(n_0 + n') + (p_0 + p') = B_{sp}[n_0p_0 + n'(n_0 + p_0n')]$$

This rate is given by the sum of two different coefficients: thermal equilibrium recombination rate R_{sp0} and excess carrier recombination rate R_r.

$$R_{sp0} = B_{sp0}n_0p_0 \; ; \; R_r = B_{sp}n'(n_0 + p_0 + n')$$

where it has been assumed that p' = n'. Considering a strong injection state: $n' \gg n_0, p_0$ we have:

$$R_{sp} \approx R_r \approx B_{sp}n'^2 \approx B_{sp}n^2$$

It is possible to appreciate the square relation with the injected carriers.

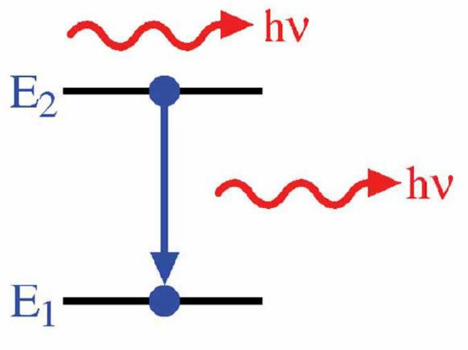

Figure 3: Stimulated emission

Stimulated emission

This type of emission is based on the presence of an “external” photon with the same energy of the band-gap. An amplification effect is then produced and the photon emitted has the same direction and phase of the “external” photon, the emission is then called “coherent”. This is the working principle of the Laser. In order to obtain stimulated emission it is needed to have a, so-called, population inversion. Electrons must be “pumped” from low energy level to high energy levels, or in the case of semiconductor from valence to conduction band.

It is important to understand the relation between stimulated and spontaneous emission, consider a system that has N1 atoms per unit volume with energy E1 and N2 atoms per unit volume with energy N2. Then the rate of upward transitions from E1 to E2 by photon absorption will be proportional to the number of atoms N1 and also to the number of photons per unit volume with energy $h\upsilon = E_2 - E_1$. Thus the rate is:

$$R_{12} \approx B_{12} N_1 \rho(h\upsilon)$$

where the proportionality factor, is called Einstein B_{12} coefficient and $\rho(h\upsilon)$ is the photon energy density per unit frequency. The rate downward transition from E2 to E1 involves spontaneous and stimulated emission. Thus can be written as:

$$R_{21} \approx A_{21} N_2 + B_{21} N_2 \rho(h\upsilon)$$

where the first term is due to spontaneous emission, while the second is related to stimulated emission with A_{21} and B_{21} Einsten coefficient respectively. To find the Einsten coefficients we consider the events in equilibrium, so that we have:

$$R_{21} = R_{12}$$

In equilibrium condition, we can use Boltzman statistic and thus we have:

$$\frac{N_2}{N_1} = \exp\left(-\frac{E_2 - E_1}{k_B T}\right)$$

where k_B is the Boltzmann constant and T the absolute temperature.

In equilibrium condition, the radiation must also reach an equilibrium photon energy density ($\rho_{eq}(h\nu)$) which is given by Plank's black body radiation law:

$$\rho(h\nu) = \frac{8\pi h\nu^3}{c^3\left[exp\left(\frac{h\nu}{k_B T}\right) - 1\right]}$$

Resolving previous equations it can be shown that:

$$B_{12} = B_{21} \quad \text{and} \quad \frac{A_{21}}{B_{21}} = \frac{8\pi h\nu^3}{c^3}$$

Consider the ratio of stimulated to spontaneous emission,

$$\frac{R_{21}(stim)}{R_{21}(spon)} = \frac{B_{21}N_2\rho(h\nu)}{A_{21}N_2} = \frac{B_{21}\rho(h\nu)}{A_{21}}$$

which can be written as

$$\frac{R_{21}(stim)}{R_{21}(spon)} = \frac{c^3}{8\pi h\nu^3}\rho(h\nu)$$

Another important ratio is stimulated emission to absorption:

$$\frac{R_{21}(stim)}{R_{12}(absorp)} = \frac{N_2}{N_1}$$

1.2.3 Non-radiative recombination in the bulk

There are several physical mechanisms by which non-radiative recombination can occur. The most common cause for non-radiative recombination events are defect in the crystal structure and Auger recombination.

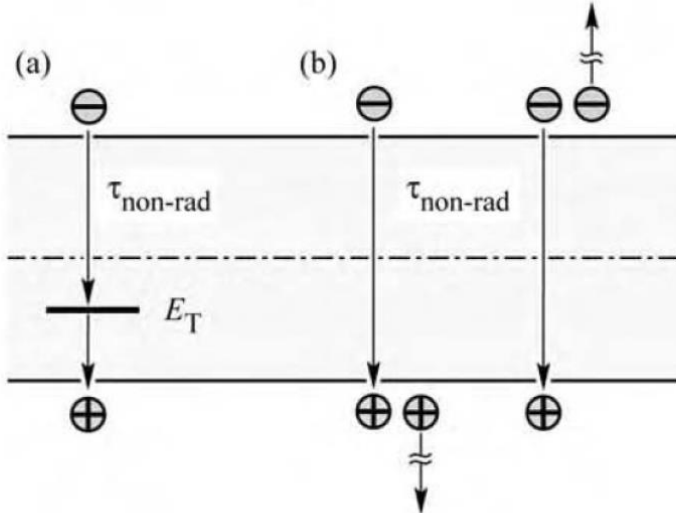

Figure 4: Band diagram illustrating non-radiative recombination: (a) via deep level, (b) via Auger process.

Deep level defect recombination

Defects in the crystal structure have energy level structure that are different form substitutional semiconductor atoms. It is quite common for such defects to form one or several energy levels within the forbidden gap of the semiconductor. These are generally called deep levels and recombination through them has been analyzed by Shockley, Hall and Read (SHR theory), the recombination ratio is:

$$R_{SHR} = \frac{p_0 \Delta n + n_0 \Delta p + \Delta n \Delta p}{\left(N_T v_p \sigma_p\right)^{-1}(n_0 + n_1 + \Delta n) + (N_T v_n \sigma_n)^{-1}(p_0 + p_1 + \Delta \mathrm{p})}$$

where Δn = Δp are the variation in electron and hole density relative to steady state; v_n and v_p are the electron and hole thermal velocities, \and σ_n, σ_p are the capture cross sections of the traps. The quantities n_1 and p_1 are the electron and hole concentrations if the Fermi energy is located at the trap levels:

$$n_1 = n_i exp\left(\frac{E_T - E_{Fi}}{kT}\right) \quad \text{and} \quad p_1 = n_i \exp\left(\frac{E_{Fi} - E_T}{kT}\right)$$

It is important to analyze the timing dynamics of the recombination generation process in order to have a powerful instrument to investigate degradation mechanism. The non-radiative lifetime of excess electrons can be deduced from the equation:

$$R_{SHR} = \frac{\Delta n}{\tau}$$

Consequently, the lifetime is given by:

$$\frac{1}{\tau} = \frac{p_0 + n_0 + \Delta n}{\left(N_T v_p \sigma_p\right)^{-1}(n_0 + n_1 + \Delta n) + (N_T v_n \sigma_n)^{-1}(p_0 + p_1 + \Delta \mathrm{p})}$$

Assuming that the semiconductor is p-type, and thus hole are majority carrier we have: $p_0 \gg n_0$ and $p_0 \gg p_1$. Assuming also a small variation from equilibrium ($\Delta n \ll p_0$), the minority carrier lifetime is given by:

$$\tau = \tau_{n0} \frac{1}{N_T v_n \sigma_n}$$

while in the case of a n-doped semiconductor we have:

$$\tau = \tau_{p0} \frac{1}{N_T v_p \sigma_p}$$

Assuming that the trap captures electrons and holes at the same rate: $v_p \sigma_p = v_n \sigma_n$ and $\tau_{n0} = \tau_{p0}$ we obtain:

$$\tau = \tau_{n0}\left(1 + \frac{p_1 + n_1}{2n_i}\right) = \tau_{n0}\left[1 + \cosh\left(1 + \frac{E_T - E_{Fi}}{kT}\right)\right]$$

where E_{Fi} is the intrinsic Fermi level, which is typically close to the middle of the gap. The cosh function has a minimum when the argument of the function is zero. Thus, the non-radiative lifetime is minimized if $E_T - E_{Fi}$ is zero; i.e. when the trap level is at or close to the mid-gap energy. For such mid-gap levels, the lifetime is given by $\tau = 2\tau_{n0}$. This result demonstrates that deep levels are effective recombination centers if they are near the middle of the gap. Close to a deep level, the luminescence intensity decreases. A single point defect will be di-cult to observe due to its relatively small effect. Frequently, however, defects group into clusters of defects or extended defects. Such extended defects are for example, threading dislocations and misfit dislocations occurring when epitaxial semiconductors are grown on mismatched substrates, i.e. substrates with a different lattice constant from that of the epitaxial layer.

Auger recombination

Another important non-radiative recombination mechanism is Auger recombination. In this process, the energy becoming available through electron -hole recombination (approximately Eg), is dissipated by the excitation of a free electron high into the conduction band, or by a hole deeply excited into the valence band. The processes are shown schematically in Figure 4-b. The highly

excited carriers will subsequently lose energy by multiple phonon emission until they are close to the band edge. The recombination rates due to the two Auger processes shown in Figure 4-b are given by:

$$R'_{Auger} = C_p n p^2 \quad \text{and} \quad R''_{Auger} = C_n n^2 p$$

Auger recombination is proportional to the square of the carrier concentration (either p^2 or n^2) since two carriers of the same type (either two holes or two electrons) are required for the recombination process. The first process (R'_{Auger}) is more likely to happen in p-type semiconductors due to the abundance of holes. The second process (R''_{Auger}) is more likely in n-type semiconductors due to the abundance of electrons. During Auger recombination, energy and momentum must be conserved. Owing to the differences in conduction and valence band structure in semiconductors, the two Auger coefficients Cp and Cn are generally different. In the high-excitation limit in which the non-equilibrium carriers have a higher concentration than equilibrium carriers, the Auger rate equations reduce to:

$$R_{Auger} = \left(C_p + C_n\right) n^3 = C n^3$$

where C is the Auger coefficient. Auger recombination reduces the luminescence efficiency in semiconductors only at very high excitation intensity or at very high carrier injection currents. This is due to the cubic carrier concentration dependence. At lower carrier concentrations, the Auger recombination rate is very small and can be neglected for practical purposes.

Non-radiative recombination at surfaces

Surfaces are a strong perturbation of the periodicity of a crystal lattice. This perturbation generate several types of defects, and the addition of electronic state inside the forbidden band-gap of the semiconductor. Atoms that are placed on the surface of crystal obviously cannot have a complete bonding structure due to the lack of neighboring atoms. This partially filled electron orbitals, or dangling bonds are electric states that can be located in the forbidden gap and act as recombination centers.

At the semiconductor, surface carriers will recombine rapidly due to surface states. Surface recombination leads to a reduced luminescence efficiency and also to heating of the surface due to non-radiative recombination at the surface. Both effects are unwanted in electroluminescent devices. An experimental test reveals that the luminescence decreases in the near-surface region. There are several methods used in order to narrow surface recombination, one generally used is passivation

layer, which cover the device, and has the function to reduce the surface recombination. The drawback of passivation layer was the high presence of Hydrogen and, for this reason, they are thought to be responsible for H passivation of Mg dopant in p-type GaN.

1.3 LED die structures

1.3.1 Homojunction LEDs

The homojunction LED is the simplest LED structure, consisting of a p-n junction realized with a single material. In such a structure, the carrier distribution de pends on the diffusion constant of the carriers. Under forward bias, electrons will diffuse from the n-side to the p-side, while holes will diffuse from the p-side to the n-side and eventually will recombine with majority carriers. The mean distance that a minority carrier diffuses before recombination is the diffusion length, which is equal to $L_n = \sqrt{D_n \tau_n}$ and $L_p = \sqrt{D_p \tau_p}$ for electrons and holes, respectively. We can see that the carrier distribution along the junction is proportional to the diffusion constant, and thus to the carrier mobility, and to their lifetime.

In typical semiconductors, the diffusion length is in the order of a several micrometers. For example, the diffusion length of electrons in p-type GaAs is equal to $L_n \approx 15\mu m$ and thus the minority carriers are distributed over a region several micrometers thick [1]. Figure 5 shows the carrier distribution in a p-n homojunction under zero bias and under forward bias, respectively. Note that minority carriers are distributed over a quite large distance under forward bias condition. Thus, recombination occurs over a large region, with a strongly changing of minority carrier concentration. The large recombination region in homojunctions is not beneficial for efficient recombination. This is due to the fact that the radiative recombination rate $R = Bnp$ is proportional both to electron and hole concentration and, as we have seen above, these concentrations are quite low in this structure. For this reason, p-n homojunction structure is not usually employed for the realization of LEDs.

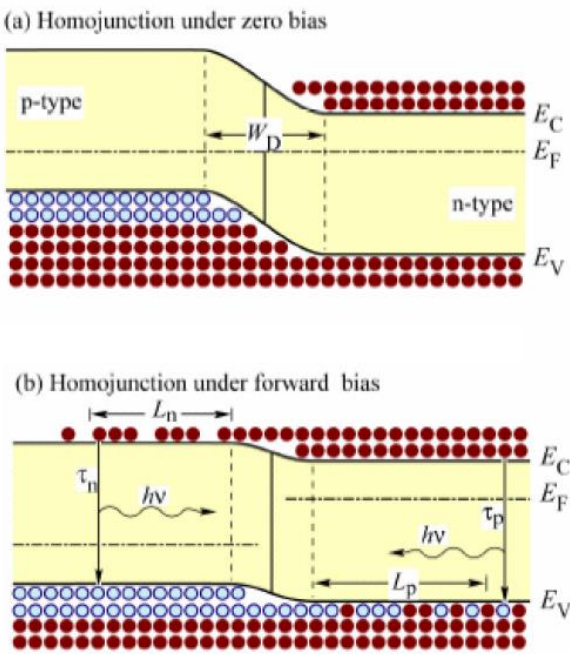

Figure 5: Carrier distribution in a p-n homojunction under (a) zero bias and (b) forward bias.

1.3.2 Heterojunction LEDs

All high-intensity light-emitting diodes do not use the homojunction design but rather employ heterojunction structures, which have clear advantages over homojunction devices. Heterojunction devices employ two types of semiconductors, with different energy gap and other physical properties, such as the dielectric permittivity. As in homojunction LEDs, also in heterojunction LEDs materials with different conductivity (i.e. both n-type and p-type doped materials) are usually employed, even if interesting results can be obtained also employing materials with different energy gap and the same type of doping.

When a p-n heterojunction is formed, electrons diffuse from the n-side to the p-side and holes diffuse from the p-side to the n-side, as in a p-n homojunctions. However, because of the different energy gap and electronic affinity between different materials, the carrier diffusion creates discontinuities both in the conduction band (ΔE_c) and in the valence band (ΔE_v), as shown in Figure 6 for a generic heterojunction between two different semiconductors. In particular, from the Anderson's theory results:

$$\Delta E_c = q(\chi_1 - \chi_2) \text{ And } \Delta E_v = \Delta E_g - \Delta E_c$$

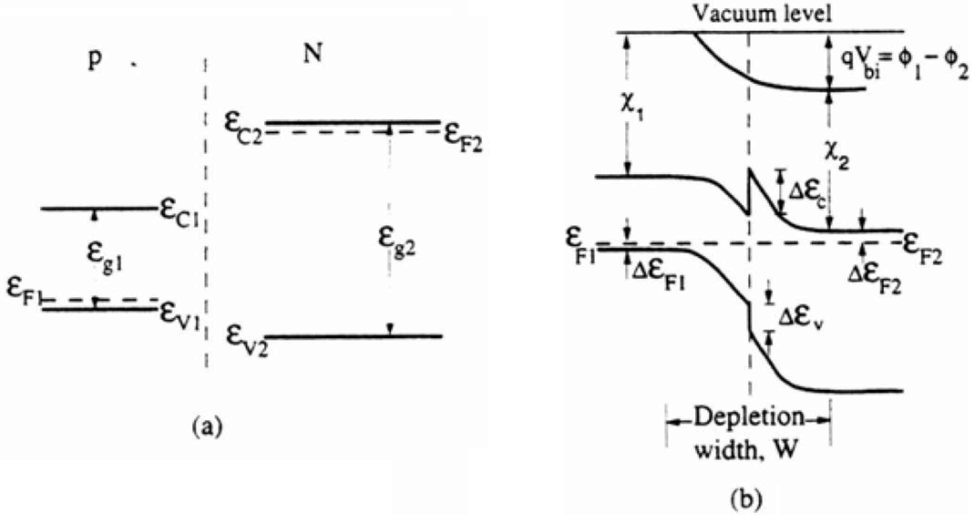

Figure 6: Band diagram (a) before and (b) after the formation of a heterojunction between two semiconductors with different energy gap. The band diagram on the right-hand is referred to the equilibrium condition under zero bias.

In order to understand how heterostructures can influence the carrier distribution in the proximity of junction, we consider the heterojunction of Figure 6 when a forward bias is applied. An increase in the forward voltage reduces the electron barrier: the results of applied bias is shown in Figure 7: as it can be noticed, the discontinuity ΔE_c in the conduction band does not slow the electron flow. On the other hand, even if also the barrier to hole flow is reduced, the discontinuity ΔE_v in the valence band does not change with increasing the forward voltage, thus strongly slowing the hole flow towards the n-side. As a result, a hole confinement was obtained in such a structure, thus increasing its concentration in proximity of the junction. Therefore, the radiative recombination probability results increased with respect to the homojunction structure. However, from Figure 7 it is clear that it is not possible to obtain simultaneous confinement of both electron and holes in the same region. For this reason, even if a single heterojunction results in an improved radiative efficiency, it is not the best solution to obtain LEDs with high efficiencies.

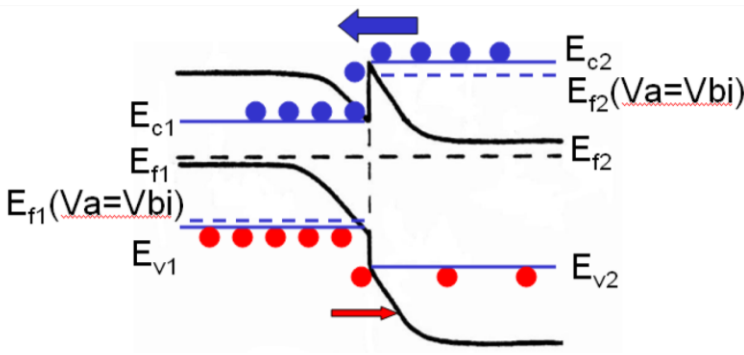

Figure 7: Carrier distribution in a p-n heterojunction under forward bias condition.

A better solution that permits to obtain very high internal quantum efficiency is the double heterostructure (DH). It consists of two barriers, which are obtained by interposing a small band-gap semiconductor, usually indicated as the active region, between two semiconductor layers having a greater energy gap with respect to the active region. The effect of heterojunctions on the carrier distribution is shown in Figure 8: as it can be noticed, carriers injected in the active region of the double heterostructure are confined to this zone by means of the barriers. As a result, the thickness of the region in which carriers recombine is given by the thickness of the active region, than rather the diffusion length. If the active region thickness is appropriately chosen, the radiative recombination rate can be strongly increased with respect to the homojunction structure, because the carriers in the active region of a double heterostructure have a much higher concentration than carriers in homojunctions. For example, the diffusion length of carriers may range from 1 to 20 μm. On the other hand, the active region of a double heterostructure may range from 0.01 to 1 μm.

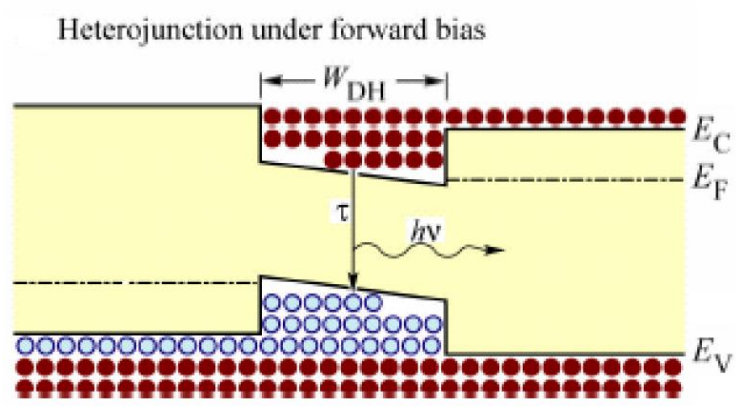

Figure 8: Carrier distribution in a double heterostructure (DH) under forward bias.

Double heterostructures can also be used to confine light to waveguide regions: this can be obtained thanks to the difference between the refractive index of active region and barrier layers. In particular, optical confinement is used for the realization of edge-emitting LEDs [1]. Moreover, due to the smaller energy gap of the active region with respect to the barrier layers, emitted photons from the active region will not be reabsorbed by barriers, thus further increasing the optical efficiency of devices.

However, hererostructures are characterized by also some drawbacks, which can limit the optical efficiency of devices, including:

- increased device resistance caused by the heterointerfaces;
- carrier loss in double heterostructures;

- carrier overflow in double heterostructures;
- lattice strain due to the lattice mismatch between different semiconductor materials.

In the following, we will briefly analyze each of these drawbacks.

Resistance caused by heterointerfaces

One of the major drawbacks introduced by heterostructures is the resistance caused by heterointerfaces. In order to understand the origin of the resistance, we refer to Figure 9, which shows the band diagram of a heterostructure consisting of two semiconductors with different band-gap energy and it is assumed that both sides of the heterostructure are of n-type conductivity.

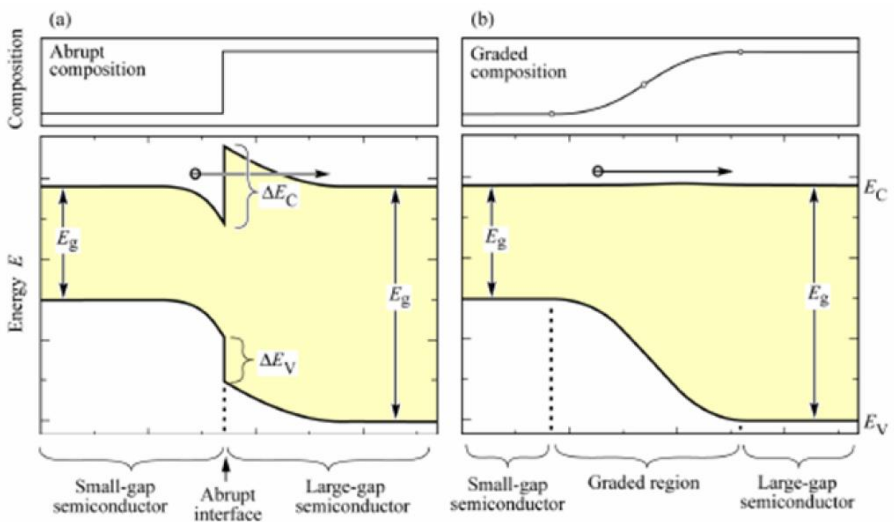

Figure 9: Band diagram of (a) an abrupt n-type-n-type heterojunction and (b) a graded heterojunction between two materials with different energy gap.

In such a structure, electrons in the large-bandgap material will diffuse over to the small-bandgap material. As a result, an electrostatic dipole forms, consisting of a positively charged depletion layer with ionized donors in the large-bandgap material, and a negatively charged electron accumulation layer in the small-bandgap material, thus inducing a band bending, as shown in Figure 9-a . Note that a barrier to the electron flow is formed in the conduction band: thus, carriers transferring from one semiconductor to the other must overcome this barrier by either tunneling or by thermal emission over the barrier. In any case, the barrier to electron flow constitutes a resistance at the heterointerface, which can have a strong deleterious effect on device performances. In fact, the thermal dissipation produced by this resistance leads to heating of the active region, thereby decreasing the radiative efficiency.

A possible solution to this problem is to eliminate heterostructure band discontinuities: this can be obtained by grading of the chemical composition of the semiconductor near the heterostructure, as shown in Figure 9-b [2]. In particular, it has been demonstrated that the resistance introduced by abrupt heterostructures can be completely eliminated by parabolic grading.

Carrier loss in double heterostructures

In this section we have seen that by means of carriers confinement in the active region of a double heterostructure, a high carrier concentration is attained, resulting in a high radiative efficiency. In an ideal structure, all injected carriers are confined to the active region by the barrier layers. The energy barriers at heterointerfaces, ΔE_c and ΔE_v, are typically of the order of several hundreds of meV, i.e. much larger than kT. Free carriers in the active region are distributed according to the Fermi-Dirac distribution and, as a result, some carriers have a higher energy than the height of the confining barrier. Thus, some of the carriers will escape from the active region, as shown in Figure 10. This phenomenon will produce a leakage current and a reduction of the optical efficiency.

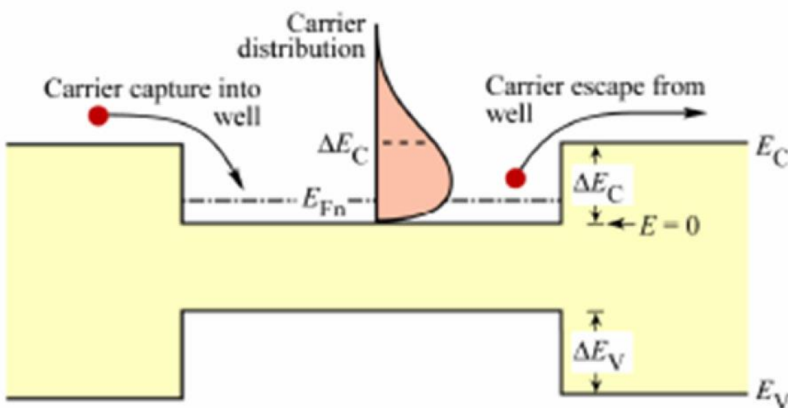

Figure 10: Carrier distribution in the active region of a double heterostructure, showing the carrier capture and escape.

The leakage current generated by carrier loss in double heterostructures depends on several factors, including the barrier heights ΔE_c and ΔE_v and the device temperature. Obviously, a reduction of barrier height induces an increase in the leakage current. Thus, a high barrier height is required to minimize the leakage current. In addition, an increase of the temperature results in an increased leakage current, due to the higher thermal energy of carriers. In fact, the leakage current increases exponentially with temperature, thus strongly limiting the radiative efficiency. To reduce the temperature dependence of the emission, high barriers are required [1].

In order to reduce carrier leakage out of the active region, blocking layers are usually inserted. Such blocking layers are regions with a high band-gap energy located at confinement-active interface. In

particular, the electron leakage current is larger than the hole leakage current, due to the usually larger diffusion constant of electrons compared to holes in III-V semiconductors. For this reason, electron-blocking layers are used in many LED structures to reduce electron escape out of the active region.

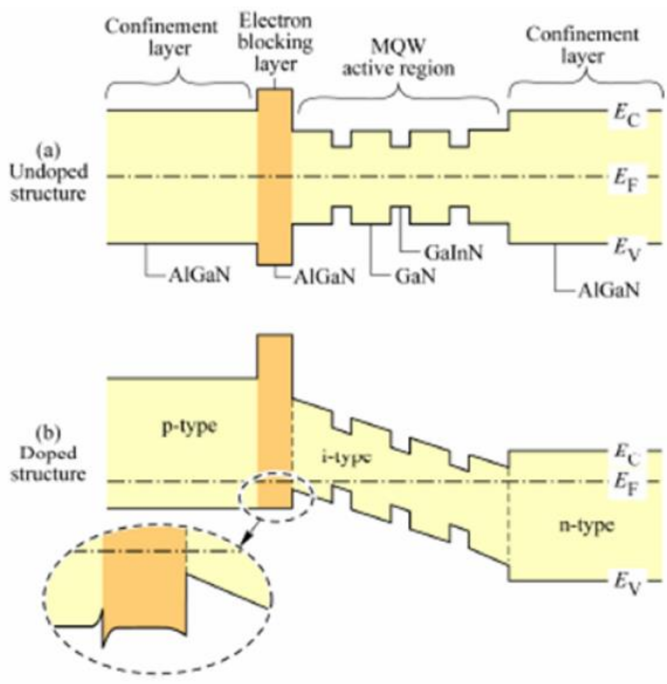

Figure 11: InGaN/GaN MQW LED structure with electron-blocking layer. (a) Band diagram without doping and (b) with doping.

An example of a InGaN-based LED structure with electron blocking layer is represented by the band diagram of Figure 11. The LED has a InGaN/GaN multi-quantum well active region and AlGaN confinement layers. An AlGaN electron-blocking layer is included in the p-type confinement layer at the confinement active interface. Figure 11-a, which is referred to an undoped structure, shows that the AlGaN electron-blocking layer creates a barrier to current both for electrons as well as for holes. However, as shown in Figure 11-b, in the doped structure the barrier in the valence band is screened by free carriers so that there is no barrier to the flow of holes in the p-type confinement layer. In particular, from the inset of Figure 11-b it can be observed that a potential spike and notch occur at the confinement-blocking layer interface. Hole must tunnel through the potential spike when propagating towards the active region. The valence band edge can be completely smoothed out by compositional grading at the confinement-blocking layer interface so that the electron blocking layer does not impede the hole flow at all [1].

Carrier overflow in double heterostructures

In a double heterostructure, as the injection current increases, the carrier concentration in the active region increases and consequently the Fermi level rises. For sufficiently high current densities, the Fermi energy will rise to the top of the barrier. At this point, the active region is filled with carriers and a further increase in the injection current will not result in an increase of the carrier concentration in the active region. This phenomenon is known as carrier overflow. As a result, the optical intensity saturates.

Generally, the problem of carrier overflow is more severe in structure with a small-active region volume. This, in turn strongly depends on the barrier heights ΔE_c and ΔE_v, and on the active region thickness. In order to limit this problem, heterostructures with high barrier heights and high thickness need to be created. However, note that a high active region thickness can reduce the optical efficiency, due to the defects introduced by lattice strain at heterointerfaces. In fact, as the thickness of active region is increased, also the lattice strain increases. For this reason, multiple-quantum well (MQW) LED structures are usually preferred. As an example, in Figure 12 are shown the experimental results of an LED structure with one, four, six, and eight quantum wells [3]: as the number of quantum wells is increases, the current level at which saturation occurs increased, and the optical saturation intensity increases as well.

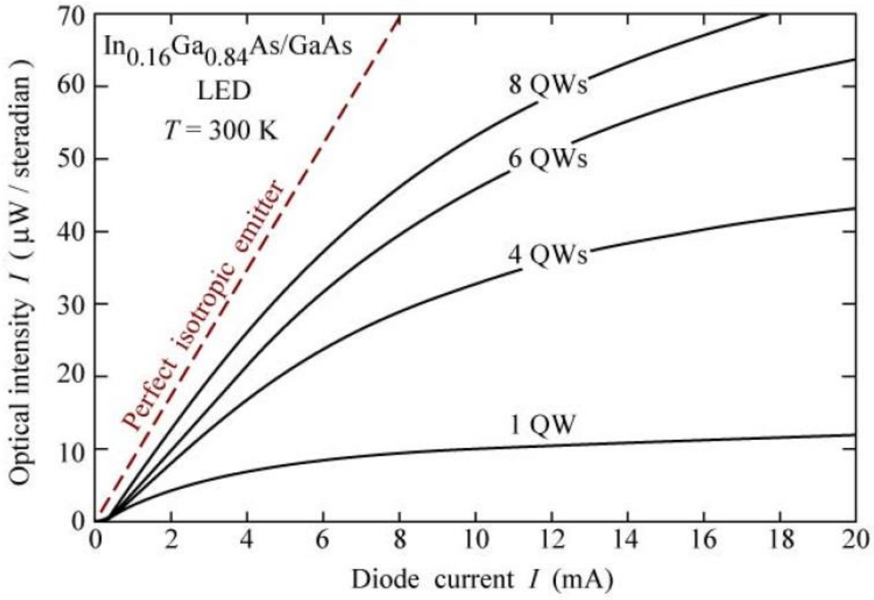

Figure 12: Optical intensity emitted by $In_{0.16}Ga_{0.84}As/GaAs$ LEDs with active region consisting of one, four, six and eight quantum wells, respectively [3]. In addition, the theoretical intensity of a perfect isotropic emitter is shown for comparison.

Lattice strain at heterointerfaces

Another problem related to heterostructures is represented by the lattice mismatch between different materials. The difference between lattice constants of the active region and the barrier layers induces lattice strain at heterointerfaces. In particular, lattice strain results in the formation of defects and dislocations in the crystal. An example is reported in Figure 13 that illustrates a crystal structure with lattice constant a1 epitaxially grown on another crystal with lattice constant $a_0 > a_1$: dangling bonds can be observed at the heterointerface as a consequence of the lattice mismatch. As cited above, lattice strain negatively influences the optical efficiency of devices, due to the formation of defects and dislocations at heterointerfaces.

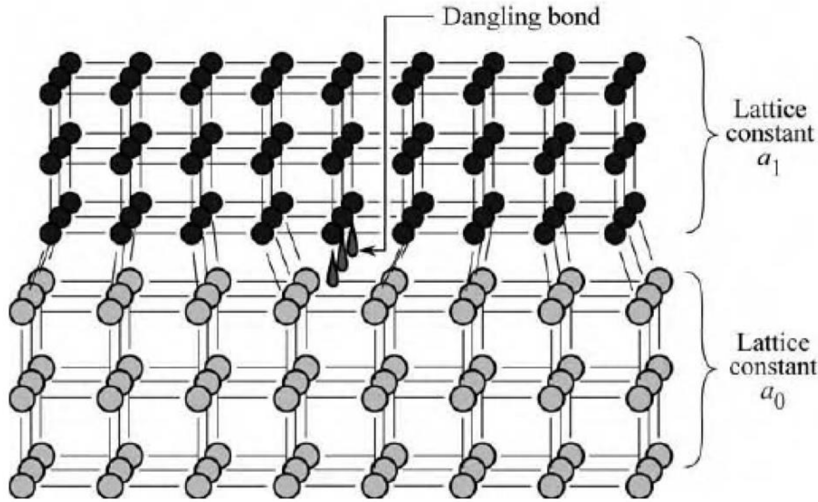

Figure 13: Schematic illustration of lattice strain between materials with different lattice constants in a crystal structure. Also dangling bonds can be observed because of lattice mismatch.

However, if the difference between the lattice constants of materials is small, it is possible to grow epitaxial layers with a small concentration of defects and dislocations. This is because the mismatched crystal grown on top of the semiconductor will initially be strained elastically and will assume the same in-plane lattice constant as the underlying substrate. Once the energy needed to strain the lattice exceeds the energy required to form misfit dislocations, the thin film relaxes to its equilibrium lattice constant by forming misfit dislocations. The layer thickness at which misfit dislocations are formed is called the critical thickness [1].

Finally, we have to consider that lattice strain induces also a piezoelectric field in the active region: this field can induce a spatial separation between electrons and holes in the active region, resulting in a decrease of the optical efficiency. This effect is particularly prominent in heterostructures with high

thickness of the active region. The problems related to piezoelectric field are reduced in quantum well structures, due to the small thickness of quantum wells.

1.3.3 Quantum well structures

A quantum well structure is a double heterostructure where the thickness of active region is very small, in the order of few nanometers. Thanks to the small active region thickness, very high carrier concentration can be obtained in a quantum well LED, thus strongly increasing the radiative recombination rate.

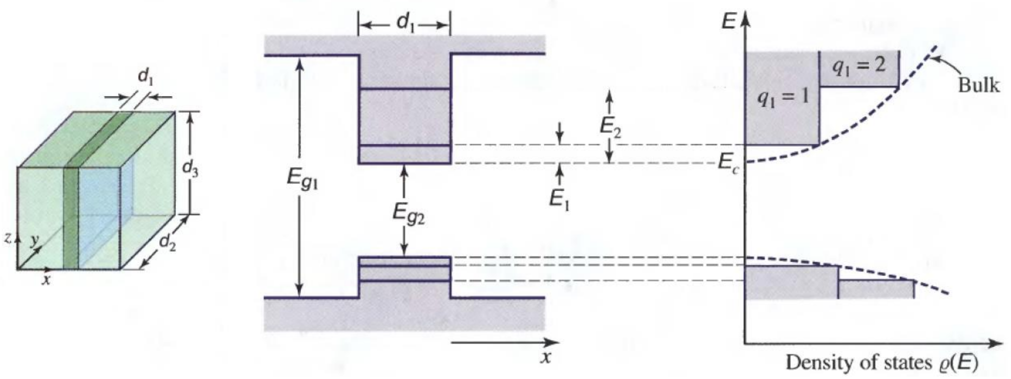

Figure 14: On the left side, tridimensional view of a single quantum well structure. On the center, band diagram of quantum well structure, showing the discrete energy states within the quantum well. On the right side, density of states in a quantum well structure.

Consider the single quantum well structure illustrated on the left side of Figure 14, where d1 is the quantum well thickness. If the quantum well thickness is comparable to the De Broglie wavelength of electrons and holes, carriers are confined along the x-direction: as a consequence of this phenomenon, allowed energy states within the active region can no longer be considered continuous, but rather they become discrete. Thus, in such a structure, the active region acts as a potential well for carriers and for this reason it is called quantum well structure. The band diagram of a quantum well structure is shown in the center of Figure 14.

Ideally, if the motion of carriers is permitted only along the x -direction, the recombination processes can occur only between discrete energy levels inside the quantum well. However, in practical cases, LED structure is tridimensional and thus, the quantum well has to be considered as a bidimensional layer: as a consequence, carriers are confined only along x -direction, but they can move freely along

the other two directions. In this case, the energy-momentum relation for electrons can be expressed as follow [4]:

$$E = E_c + E_q + \frac{\hbar^2 k^2}{2m_c}$$

where E_c is conduction band edge, E_q is the difference between a discrete energy level inside the quantum well and the conduction band edge, m_c is the effective mass of electron, and $k = (k_1, k_2)$ is the bidimensional wave vector relative to motion along y-z directions. Thus, from the previous equation, we can understand that recombination transitions do not exclusively occur between discrete energy levels. However, the quantum effect within the quantum well leads to a change in the density of energy states, as shown on the right side of Figure 14: in this case the density of energy states shows a piecewise constant trend, differently from the parabolic trend shown by a bulk semiconductor material. In particular, it is interesting to observe that the density of energy states is zero for energies lower than the fundamental level (i.e. the level with the lowest energy): this means that in a quantum well structure the lowest energy transition do not occur between the conduction and valence band edges, but rather between the fundamental discrete energy levels in the conduction and valence band of quantum well, respectively. This transition is illustrated in Figure 15.

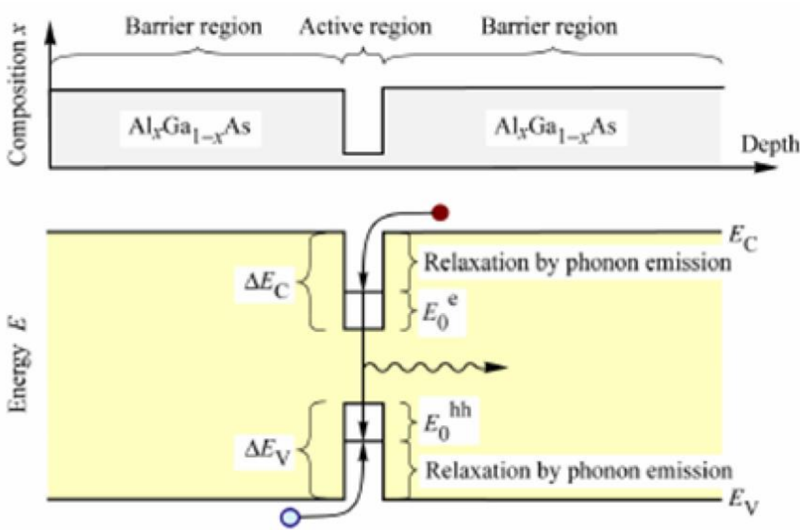

Figure 15: Material composition and band diagram of a quantum well structure. In particular, it is illustrated the radiative transition occurring between the fundamental energy levels in the conduction and valence band of quantum well.

Quantum well structures show some interesting advantages with respect to typical double heterostructures. First, the carrier concentration in a quantum well is higher than in a normal heterostructure, due to the reduced volume of active region: this determines an increase in the

radiative recombination rate. Second, thanks to the small active region thickness, quantum well structures shows a smaller lattice strain and thus they can be grown with a small concentration of defects and dislocations. Finally, also the confinement effect due to piezoelectric fields is smaller in a quantum well structure with respect to a typical double heterostructure.

However, due to the reduced volume of the active region, the problem of carrier overflow occurring at high injection current is more severe in a quantum well structure with respect to a double heterostructure. To overcome this problem, multiple-quantum well (MQW) structures are usually realized: by this way the active region volume is increased, without losing the advantages offered by quantum well structure. An example of AlGaAs/GaAs multiple-quantum well structure is illustrated in Figure 16.

If the barrier layers thickness between the quantum wells of a MQW LED is very small, some of electrons can cross the barriers via tunneling effect: as a consequence, the discrete energy levels within the quantum wells degenerate into small bands. Finally, note that quantum well structures can be realized also by spatially varying the doping concentration of semiconductor, than rather the chemical composition: by this way, spatial charge layers, and thus potential barriers, are created in order to form quantum wells [4].

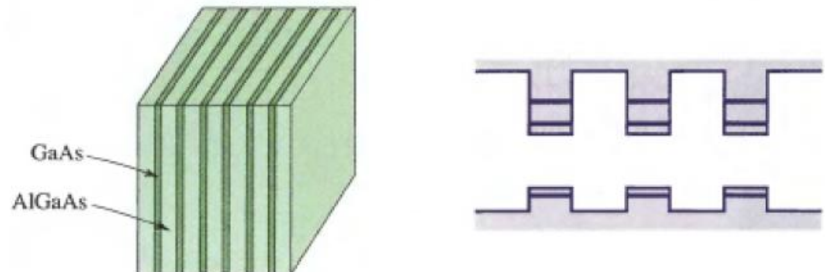

Figure 16: AlGaAs/GaAs multiple-quantum well (MQW) structure and relative band diagram. Because these materials are lattice matched in a large range of composition, they can be grown minimizing the lattice strain.

1.4 Electrical properties of LEDs

Electrical properties of LEDs are described by the current-voltage (I-V) characteristic and by the capacitance-voltage (C-V) characteristic. In this section we will briefly review the main relations that describe the electrical properties of LEDs. However, for a more detailed and specific description of all the aspects concerning the electrical characteristics of the LEDs, reader can refer to [5] and [6].

1.4.1 Current-voltage (I-V) characteristic

From the electrical point of view, a light-emitting diode is equivalent to a p-n junction diode and thus, the current-voltage (I-V) characteristic of an ideal LED is described by the well known Shockley equation:

$$I = I_s\left(e^{\frac{qV}{kT}} - 1\right)$$

where I_s is the saturation current, which can expressed by the following relation:

$$I_s = A_{pn} q n_i^2 \left(\frac{1}{N_D}\sqrt{\frac{D_p}{\tau_p}} + \frac{1}{N_A}\sqrt{\frac{D_n}{\tau_n}}\right)$$

In this equation A_{pn} represents the junction area, N_D and N_A are the donors and acceptors concentrations respectively, D_n and D_p are the diffusion constants for electrons and holes respectively, and finally τ_n and τ_p are the minority carrier lifetimes (electrons on the p-side and holes on the n-side respectively).

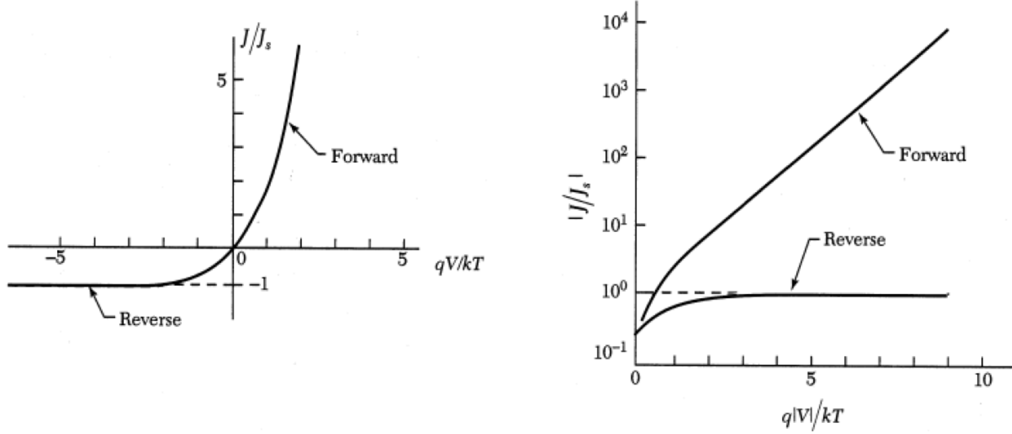

Figure 17: Current-voltage (I-V) characteristic of an ideal p-n junction diode. The characteristic is shown in a linear scale on the left side, and in a semilogarithmic scale on the right side.

Figure 17 illustrates the I-V characteristic of an ideal p-n junction in a linear and in a semi-logarithmic scale, respectively. In particular, it can be noticed that under reverse bias condition the current saturates to Is; on the other hand, under forward bias the current exponentially grows with increasing the applied voltage.

Under forward bias, for voltage levels much greater than the thermal voltage $kT = q$, the exponential term in the Shockley equation dominates and thus the Shockley equation can be simplified with the approximate relation:

$$I_s \approx A_{pn} q \left(N_A \sqrt{\frac{D_p}{\tau_p}} + N_D \sqrt{\frac{D_n}{\tau_n}} \right) e^{\frac{q(V-V_D)}{kT}}$$

where V_D is built-in potential (also called the diffusion voltage) of the p-n junction, which is given by:

$$V_D = \frac{kT}{q} ln \frac{N_A N_D}{n_i^2}$$

From these equations it can be seen that the current of p-n junction is very small, approximately equal to zero, for voltage levels lower than V_D, and it begins to exponentially grow for voltage levels greater than this value. The voltage level at which the current starts to quickly grow is also called threshold voltage V_{th} and as we have just seen, it is approximately equal to the built-in potential V_D.

In the case of pn junction with high doping levels, the distance between Fermi level and conduction and valence band edges is very small: as a consequence, the built-in potential V_D is approximately equal to E_g/q. Thus, the threshold voltage is strongly related to the energy gap of the semiconductor material:

$$V_{th} \approx V_D \approx \frac{E_g}{q}$$

For this reason, the threshold voltage typically increases with decreasing of the optical emission wavelength. For example, red LEDs usually have a threshold voltage lower than that of blue LEDs. Figure 18 reports typical current-voltage characteristics of p-n junctions realized with different semiconductor materials.

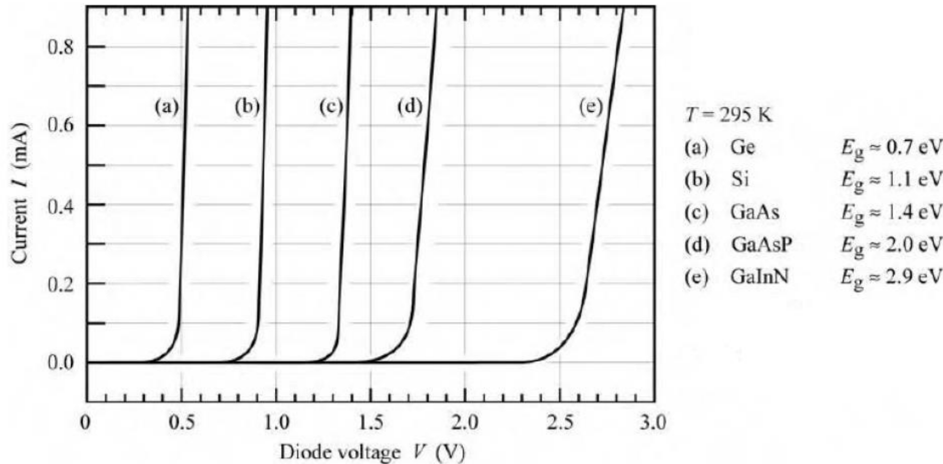

Figure 18: I-V characteristics of several pn junctions realized with different semiconductor materials. Note the increase in the threshold voltage with increasing of the energy gap.

For high reverse voltage levels, the breakdown phenomenon occurs in p-n junction: this results in an abrupt increase of reverse current. Two different breakdown mechanisms can occur: the avalanche breakdown and the Zener breakdown. The voltage level at which this phenomenon starts can range from the order of tens of volts to hundreds of volts. In LEDs the breakdown voltage is usually quite low and this fact can represent a problem in some applications. For more details about the breakdown phenomenon occurring in diodes see [5].

1.4.2 Deviations from the ideal current-voltage characteristic

The current-voltage characteristic of a p-n junction defined by the Shockley equation has been obtained under the following ideality conditions:

- negligible voltage drop across the contacts and neutral regions;
- low-injection condition, i.e. the concentration of injected minority carriers is much smaller than that of majority carriers;
- no recombination or generation processes occurs in the depletion layer.
-

In this section we will briefly analyze the non-ideality factors that can influence the electrical properties of LEDs and how they modify the current-voltage characteristic.

Generation and recombination processes in the depletion layer.

In practical diodes, there are trap levels in the depletion layer, which make generation and recombination events likely. Carrier generation and recombination causes an excess current for both forward and reverse bias.

In the reverse-bias regime, the excess current is due to the generation of carriers in the depletion layer. On the other hand, under this operating regime, the recombination probability is very low because only a few carriers are injected in the active region. When an electron-hole pair is generated, due to the influence of the electric field present in the depletion layer, generated carriers are separated and drifted to the neutral regions. This results in the generation of a reverse current. If we suppose that generation processes occurs via a deep level localized near the intrinsic Fermi level E_i, the generation current is given by:

$$I_{gen} = A_{pn}\frac{qn_iW}{2\tau_0}$$

where A_{pn} is the junction area, W is the depletion-layer thickness, and $\tau_0 = 1/(N_t\sigma_0 v_{th})$ is the minority carriers lifetime for the case of Shockley-Hall-Read recombination. At this point, the total reverse current of a p-n junctions can be defined as follow:

$$I_R = I_s + I_{gen}$$

i.e. as the sum of saturation and generation current. Thus in practical diodes, the reverse current does not saturate to the saturation current value Is, but rather it keeps increasing with reverse voltage due to the increasing depletion-layer width.

Under forward bias condition, the excess current is due to the recombination processes occurring in the depletion layer. The recombination current dominates only at low voltages. At higher voltages, the diffusion current dominates and thus the recombination current becomes negligible. Assuming that recombination transitions occur via a deep level localized near the intrinsic Fermi level E_i, the recombination current is given by:

$$I_{rec} = A_{pn}\frac{qWn_i}{2\tau_0}e^{qV/2kT}$$

where A_{pn}, W e τ_0 are the junction area, depletion-layer thickness and minority carriers lifetime, respectively, as in the case of generation current. The excess current under forward bias is also due to the surface recombination current, which is given by:

$$I_{sup} = A_{sup}Ce^{qV/2kT}$$

where A_{sup} is the external junction area and C is a generic constant that must be determined. Thus, the total forward current is given by the sum of diffusion contribution, and the two recombination currents previously reported, respectively:

$$I_F = I = I_s\left(e^{qV/kT-1}\right) + I_{rec} + I_{sup}$$

In typical silicon diodes, at low voltage levels, the recombination current in the depletion layer dominates, while in diodes based on III-V semiconductors, the dominant current at low voltage levels in due to the surface recombination [7]. In Figure 19 is shown the current-voltage characteristic of a p-n junction, in both linear and semi-logarithmic scale, when the recombination and generation contributes are taken into account.

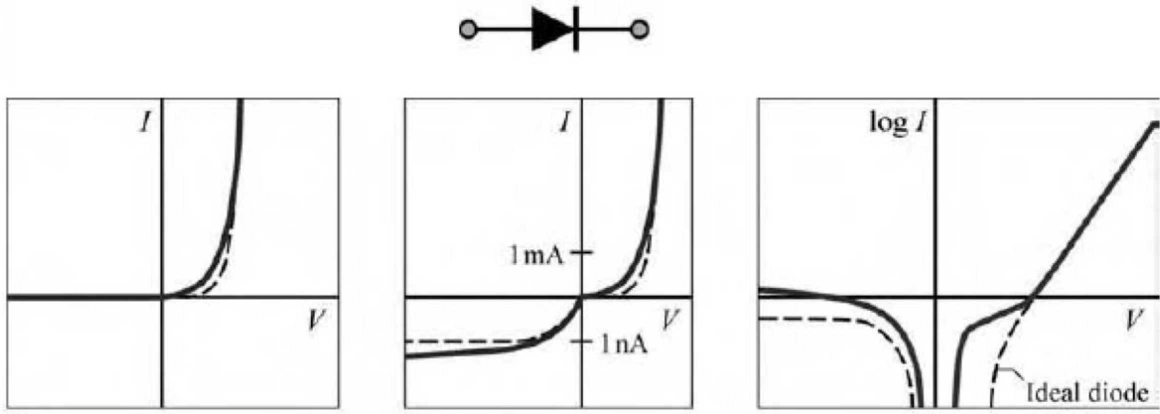

Figure 19: I-V characteristic of a pn junction, which includes the recombination and generation contributes. The characteristic is shown in the linear scale on the left side, with a particular of the curve near the origin on the center, and in semilogarithmic scale on the right side.

Photocurrent.

If a photon is incident in the depletion layer of a p-n junction, it can be absorbed, thus generating an electron-hole pair. The electrical field in the depletion layer separates the carriers and drifts them into the neutral regions. As a consequence, a photocurrent is generated, which is added to the reverse current. Alternatively, the generated electron-hole pairs can recombine, thus contributing to the excess recombination current under forward bias, at low voltage levels. In order to reduce the photocurrent contribution, measurements of I-V characteristic need to be carried out in the dark. In fact, photocurrent can negatively influence the measurements results. The effect of photocurrent on the current-voltage characteristic is reported in Figure 20.

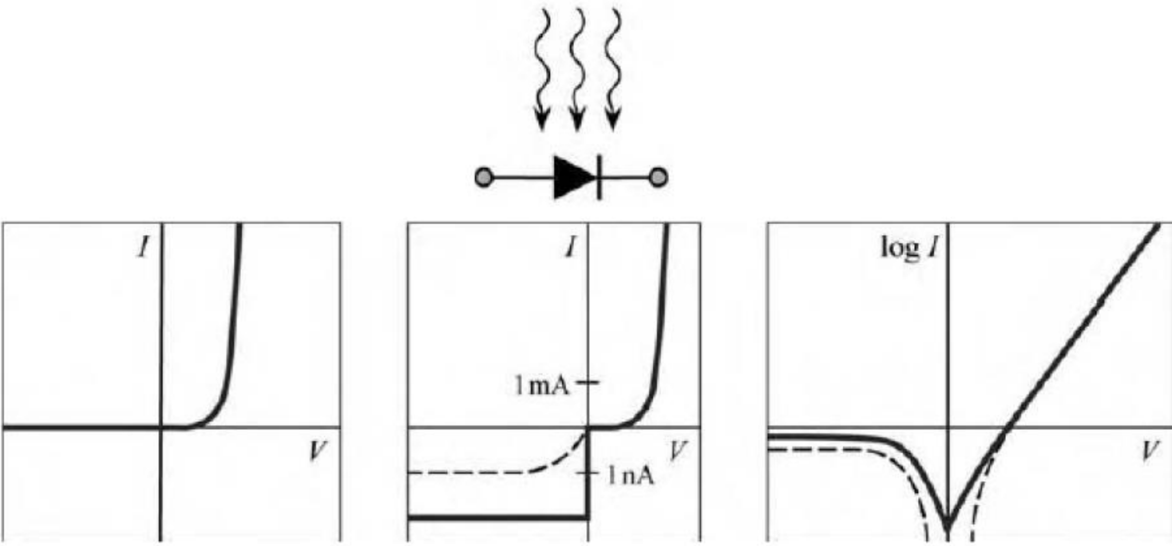

Figure 20: Current-voltage characteristic of a diode showing the photocurrent contribution. The characteristic is illustrated both on a linear and semi-logarithmic scale.

Series resistance and high-injection effects.

The resistance of contacts and neutral regions of a p-n junction can be modeled with a resistance connected in series with an ideal diode. As a consequence, an additional voltage drops across it with increasing of current level. In particular, its contribution is negligible at low current levels, but it can be dominant at high currents. In fact, the I-V characteristic shows a deviation from the exponential behavior at high forward currents, as shown in Figure 21. Note that the series resistance has a linear and a logarithmic shape on the I-V characteristic when plotted on a linear and semi-logarithmic scale, respectively. Another contribution can modify the current-voltage characteristic at high current levels, that are the high-injection effects. This is due to the fact that, in this operating regime the injected minority carrier concentration is comparable to majority carrier concentration and thus, the hypothesis used to derive the Shockley equation are no longer verified. Under these conditions, the current-voltage relation is given by:

$$I_{HI} \propto e^{qV/2kT}$$

Note the factor 2 present in the denominator of exponent [6]. As a consequence, also high-injection effects result in a decrease of the slope of characteristic with respect to the ideal case. However, at high current levels usually the dominant effect is given by the series resistance.

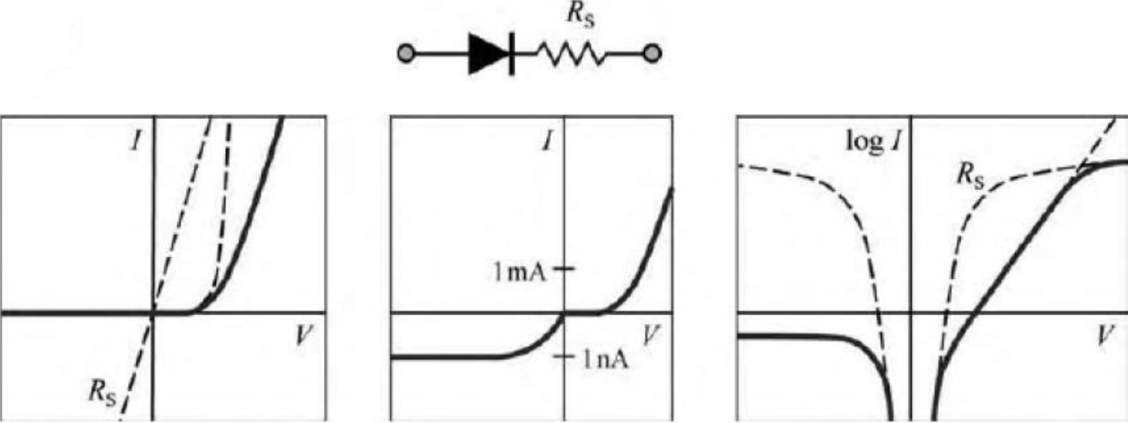

Figure 21: Current-voltage characteristic of a diode showing the contribution of a series resistance. The characteristic is reported both on a linear and semi-logarithmic scale.

Parallel (shunt) resistance.

From an electrical point of view, defective regions and surface imperfections on a light-emitting diode can be modeled with a resistance connected in parallel with an ideal diode. This shunt resistance is usually very high, differently from the series resistance, which is usually quite low. The contribution of the parallel resistance is negligible at high current levels, because in this operating regime the current flowing across the junction dominates. On the other hand, the contribution of shunt resistance can be dominant at low forward voltage levels and under reverse bias. The parallel resistance effect on the I-V characteristic is reported in **Figure 22**: note that the forward "hump" seen on the semi-logarithmic plot has about the same level as the reverse current. This is a characteristic by which a shunt can be identified.

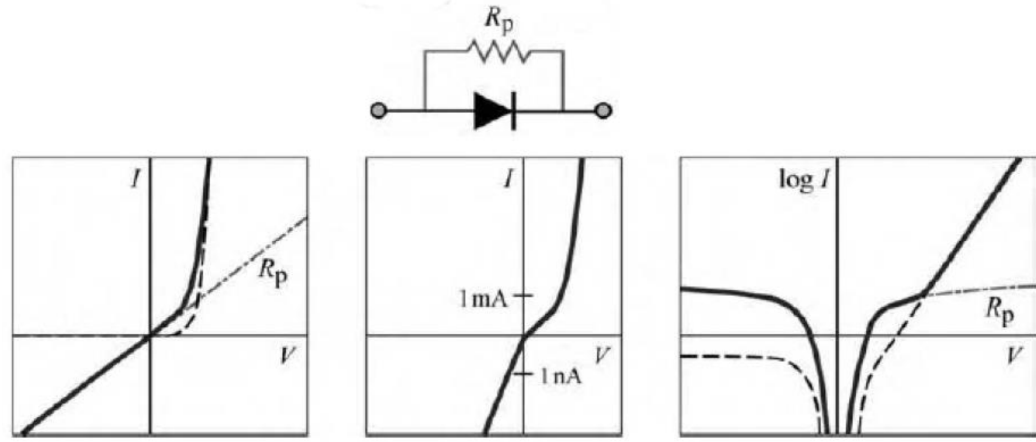

Figure 22: Current-voltage characteristic of a diode showing the contribution of a parallel resistance. The characteristic is reported both on a linear and semi-logarithmic scale.

Parasitic diode with lower barrier height and smaller area than main diode.

Surface states at the perimeter of the diode chip, or defective regions within the pn junction plane that have a lower barrier height than the main p-n junction, can be sometimes modeled as parasitic diodes connected in parallel with the main diode. In particular such diodes display premature turn-on, thus modifying the current-voltage characteristic, as shown in Figure 23. Note that the forward "hump" on the semi-logarithmic plot has much higher level than the reverse saturation current, which is not the case for diodes with a shunt [1]. Thus, the current-voltage characteristic, as given by the Shockley equation, needs to be modified in order to take into account parasitic resistances.

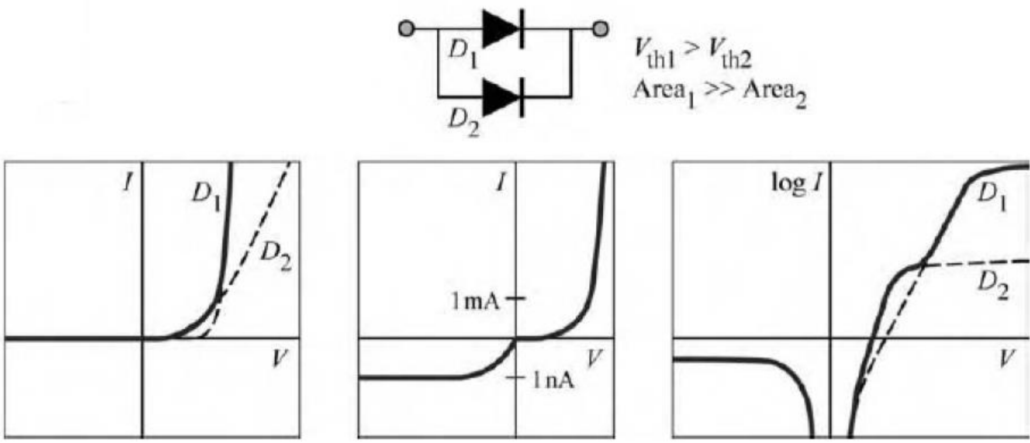

Figure 23: Current-voltage characteristic of a diode showing the contribution of a parasitic diode with lower barrier height and smaller area than main diode. The characteristic is reported both on a linear and semi-logarithmic scale.

Assuming a shunt resistance R_p (parallel to the ideal diode) and a series resistance R_s (in series with the ideal diode and the shunt), the I-V characteristic of a p-n junction diode is given by:

$$I = \frac{(V - IR_s)}{R_p} = I_s e^{\frac{q(V-IR_s)}{n_{id}kT}}$$

where n_{id} is the ideality factor : it is equal to 1 in the ideal case, while in practical diodes it is usually greater than 1. Under forward bias, $n_{id} = 2$ for low current levels, where the recombination contribute dominates. Then, $n_{id} = 2$ for medium current levels. Finally $n_{id} = 2$ for high-injection levels. However, nid values greater than 2 can be found in several optoelectronic devices: for example, in InGaN/GaN based LEDs, n_{id} values as high as 7 can be found [1]. This phenomenon has been attributed to several factors:

- as suggested by Cao, Dmitriev and Eliseev, this behavior was attributed to the fact that in heterostructure-based devices conduction is based on significant tunneling components, that must be corrected using an appropriate parameter [8] [9] [10] ;
- Franssen observed that while in simple p-n junctions recombination occurs in the neutral regions (Shockley model), in MQW structures radiative recombination takes place mostly in the middle of the depletion layer. This is expected to give rise to an increase of the ideality factor in the I-V characteristics [11];
- Shah considered that real diodes are formed by the series connection of more junctions, which contribute to the increase of the ideality factor of devices [12].

1.4.3 Temperature dependence of I-V characteristic

In this section, the temperature dependence of current-voltage characteristic will be analyzed. For the purpose, the study will be performed referring to a p-n junction, but the results can be extended also to LED heterostructures. In particular, the temperature dependence of current-voltage characteristic under reverse bias and forward bias will be analyzed separately.

In the previous section we have seen that under reverse bias the current is given by the sum of saturation current I_s and generation current I_{gen}. Moreover, both currents are proportional to the intrinsic carrier concentration n_i: in fact $I_s \propto n_i^2$, while $I_{gen} \propto n_i$. However, it is well known that the intrinsic carrier concentration increases with increasing of the temperature, as given by the following relation:

$$n_i = \sqrt{N_c N_v}\, e^{-E_g/2kT}$$

where N_c and N_v are the effective density of states at the conduction and valence band edges, respectively. It should be take into account also the temperature dependence of the energy gap E_g in the equation above, but it has been experimentally demonstrated that the term T in the denominator of exponent is dominant. Thus, an increase of the temperature results in an increase both of saturation current I_s and in the generation current I_{gen}. As a consequence, the reverse current increases with increasing of temperature.

In order to analyze the temperature dependence of current-voltage characteristic under forward bias, we calculate the temperature dependence of forward voltage across an ideal p-n junction. To do this, we modify the Shockley equation in the following form:

$$I = I_s^* \left(e^{\frac{qV - E_g}{kT}} - 1 \right)$$

where I_s^* is given by:

$$I_s^* = qA_{pn} \left(\frac{D_p N_c N_v}{L_p N_D} + \frac{D_n N_c N_v}{L_n N_A} \right)$$

Note that $L_n = \sqrt{D_n \tau_n}$ and $L_p = \sqrt{D_p \tau_p}$ are the diffusion length of electrons and holes respectively. At this point, from the equation we can derive an expression for the voltage V:

$$V(T) = \frac{kT}{q} ln \frac{I}{I_s^*} + \frac{E_g(T)}{q}$$

The first term on the right hand is related to the temperature dependence of the Fermi level: with increasing of the temperature, the separation between quasi-Fermi levels E_{Fn} and E_{Fp} in the n-side and p-side decreases, because the Fermi energy shifts towards the middle of the gap. As a consequence, the forward voltage at a given current level decreases with increasing of the temperature. Note that even though this term is proportional to T, the temperature dependence of I_s^* is dominant. On the other hand, the second term on the last equation is related to the temperature dependence of energy gap, which can be expressed by the following relation:

$$E_g(T) = E_g|_{T=0K} - \frac{\alpha T^2}{T + \beta}$$

where α and β are fitting parameters, frequently called the Varshni parameters. Thus, also this term decreases with increasing of the temperature at a given current level. In particular, it has been demonstrated that this term is usually dominant in the $V(T)$ equation [1].

Thus, the temperature dependence of the forward voltage results in a left shift of the I-V characteristic under forward bias, which correspond in a decrease of the threshold voltage. As an example, the temperature dependence of a GaAsP/GaAs LED is illustrated in Figure 24, which shows the I-V characteristic at 77 K and at room temperature. Inspection of the figure reveals that the threshold voltage as well as the series resistance of the diode increases as the diode is cooled [1].

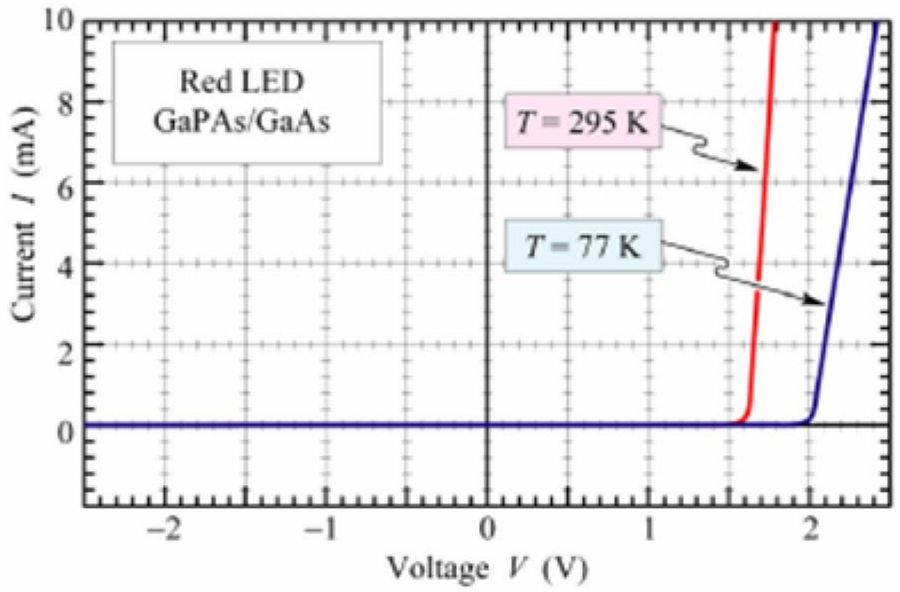

Figure 24: I-V characteristic of a GaAsP/GaAs red LED measured at 77 K and 295 K, respectively. The temperature dependence of the forward voltage can be observed from this figure.

1.5 <u>LED packaging</u>

LEDs application in different environments has led to a remarkable evolution of materials and packaging techniques, which has allowed to greatly improve the performance of solid state light sources in terms of heat dissipation, optical properties and protection from external agents.

While in common electronic devices (transistors, resistors , etc.), the "package" is a simple case that protects the chip , in the case of LEDs it is a complex system composed of different types of materials (plastics, metals, ceramics) with lot of crucial roles such as:

- to effectively convey heat outside the chip;
- to lay the role of primary optic, giving the light emitted by the chip an adequate emission spatial distribution;
- to protect the chip from external agents (mechanical, chemical or environmental);
- to bring outside the electrical contacts.

It is easy to understand the importance of these aspects if one considers that, according to recent estimates, more than 30% of the cost of a single power-LED is due to the package and will exceed 40% if one include the layer of phosphor in white LEDs (see **Figure 25**).

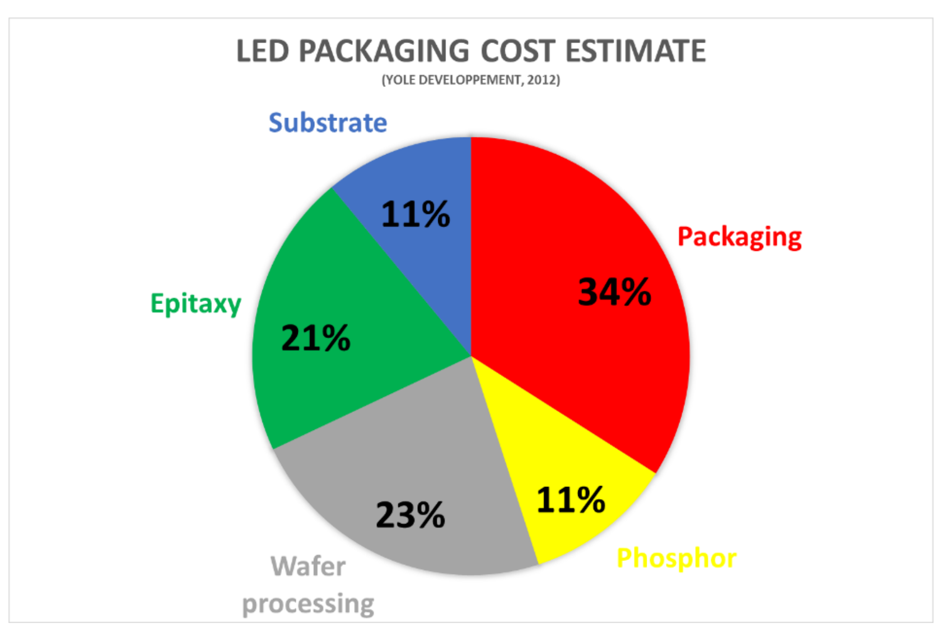

Figure 25: Cost estimate of the LED packaging components (Source: Yole Developpement,2012).

While the oldest "Through- Hole" configuration (**Figure 26**-a) is considered obsolete by now, there are currently two types of package most widely used:

- SMD (Surface Mounted) LED single or multiple die (**Figure 26**-b-c);
- Chip-on-Board (COB) Modules (**Figure 26**-d).

These two types of packages greatly differ in terms of construction techniques and in terms of thermal/optical performances and, in fact, are used in different types of applications.

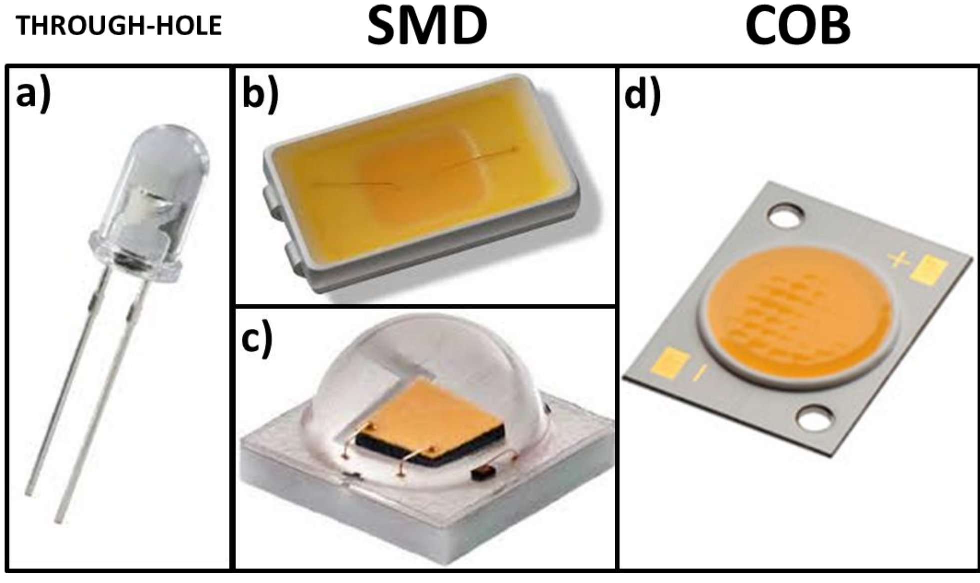

Figure 26: Package examples: a) “Through-Hole”, b) SMD Mid-power, c) SMD High-power, d) Chip-on-Board

1.5.1 SMD LEDs

SMD LEDs are the devices that have driven the technological evolution of last years and often represent the leading model of world major LED manufacturer. In lighting applications, the most used SMD LEDs can be divided in two classes: Mid-Power LEDs and High-Power LEDs.

SMD Mid-Power package

These devices are commonly used when there is not the need to concentrate high luminous intensity. Usually they work at current levels from 30mA to 150mA with electrical power levels lower than 0.5W. Despite the low luminous flux emitted (<100 lm), they can claim an extremely high efficiency (up to 150 lm/W and beyond), a very low cost e an easily manageable amount of generated heat.

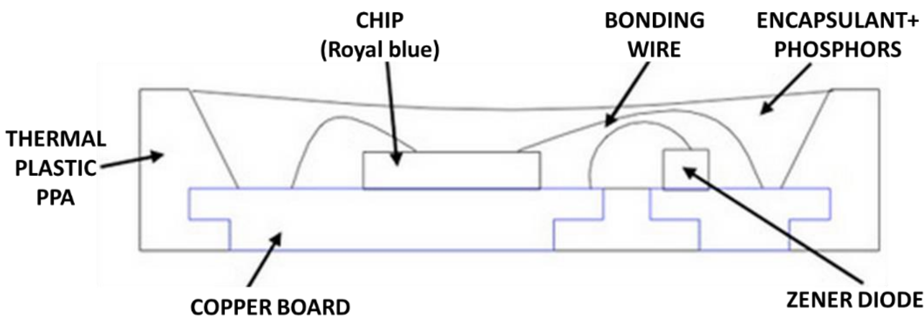

Figure 27: Typical package structure of a Mid-Power LED (Seoul Semiconductor Acrich 3030)

The typical package structure of a Mid-Power LED is showed in Figure 27. The blue chip is glued through thermo-conductive paste to a copper frame which is covered with silver in order to act as a reflector. Over the chip an epoxy resin is deposited that acts as an encapsulant, and besides it contains the phosphor particles in white LEDs. Silicone materials used as encapsulant can withstand very high temperature levels (up to 200°C) but they have the disadvantage of being more permeable to moisture and volatile compounds than, for example, epoxy resins. The package structure is then laterally supported by a thermal plastic frame, usually made of Polyphthalamide (PPA), a synthetic polymer properly engineered to withstand high temperature levels.

SMD High-Power package

The term “High-power LED” identifies a broad spectrum of devices with power levels above 1W, operating current levels up to 1.5A and luminous flux usually over 50 lm. They can be found in both single and multiple die configuration. By browsing the catalogs of the different manufacturers of

High-power LED can be seen how the features of the package of these devices are quite similar in terms both of materials and form factors, so that these type of devices are often perfectly interchangeable.

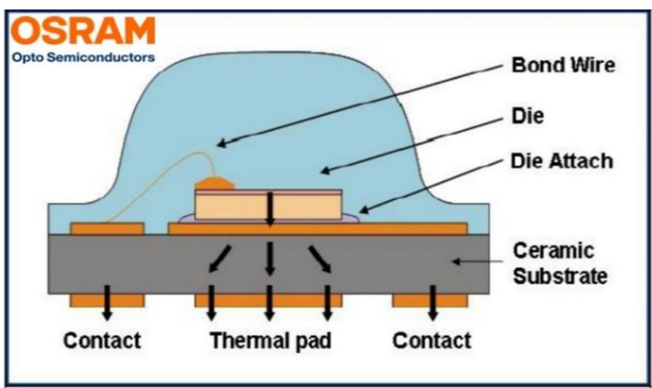

Figure 28: Schematic section of the Osram Oslon package.

By analyzing the characteristics of a typical package High-power single-chip (in the example of **Figure 28** shows the diagram of an Osram Oslon), one can see how the chip is positioned above a contact plate connected to a ceramic substrate which acts both as a dielectric and thermal conductor, while a bonding wire electrically contact the top side of the chip. Given the considerable amount of heat generated by this type of devices, the use of ceramic materials with high-thermal conductivity for the substrates has become imperative for all manufacturers worldwide.

The material used for the die attachment are of fundamental importance because they represent the first thermal interface that heat meets in its path to the outside and can act as a thermal bottleneck if these are not properly optimized. For this purpose are usually used silver pastes, epoxy adhesives or eutectic welding.

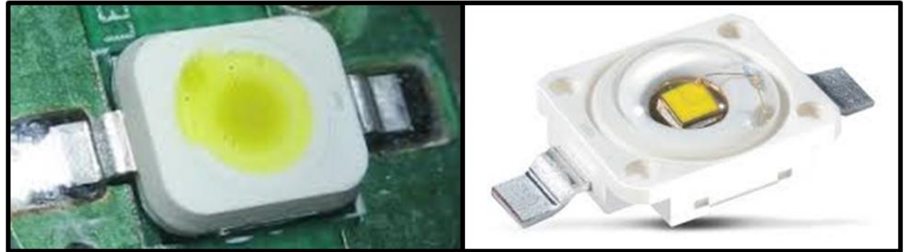

Figure 29: Comparison between two different phosphor deposition techniques on similar packages (Osram Golden Dragon)

While in the past the application of the phosphor layer was made by the dispersion of the phosphor particles within the encapsulant material (Figure 29 on the left), most recent high-power devices

adopted the "conformal coating" technique which consists in a very precise deposition of a thin layer of phosphor on the chip surface (Figure 29 on the right) which allows a better spatial uniformity of the chromatic characteristics of the emitted light. A peculiarity of this type of package is the double role of the encapsulating material, which acts both as chip protection and primary optics (see Figure 30). The materials used for the encapsulant dome may be epoxy or silicone type.

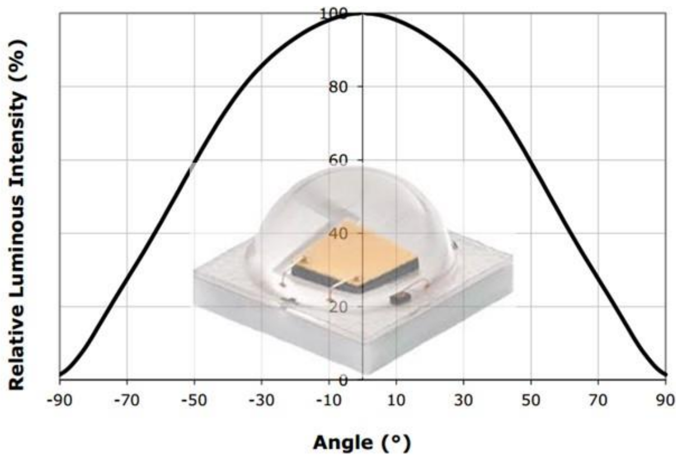

Figure 30: Normalized emission profile of a Cree XP-E2

The electrical connection of the chip can be done either by one or more bonding wires, or through the more recent "flip-chip" technology: this technique consists in the realization of the electrical connection by direct contact with the underlying plate with the die placed upside down. This technology allows to obtain both a greater robustness of the electrical device and a higher light extraction efficiency. An example of a LED that uses this technology is the Cree XB - D (Figure 31).

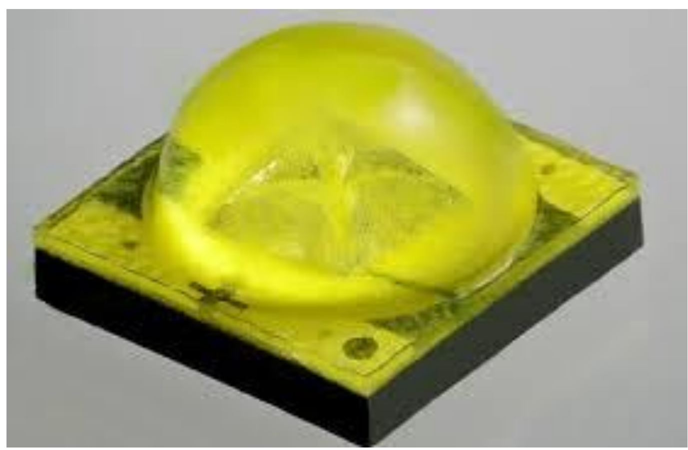

Figure 31: Cree XB-D

1.5.2 Chip-on-board (COB) modules

One of the main limits of discrete LEDs is the difficulty to concentrate high levels of luminous flux in small spaces due to package dimensions and issues of heat management . These limitations have led manufacturers to introduce the chip-on-board (COB) technology, that allows to obtain very high luminous fluxes (from 400 lm up to 12000 lm) with very small sizes. The basic idea of this technology is to mount a large number of small chips directly on the same substrate, connected together by means of bonding wires (see **Figure 32**).

Figure 32: Micrograph image of a Chip-on-Board module without the encapsulant (Source:www.globalspec.com)

This technique allows to maximize the light emitted density per unit area (see **Figure 33**-a), to reduce the overall dimensions and gives a more simple optical management: in systems that use lenses and reflectors, in fact, the best light extraction performance is obtained when the light source is as small as possible, which is difficult to achieve with discrete LEDs when there is a high flux demand. Another advantage of this technology is that it removes a thermal interface between the chip junction and the environment (**Figure 33**-b).

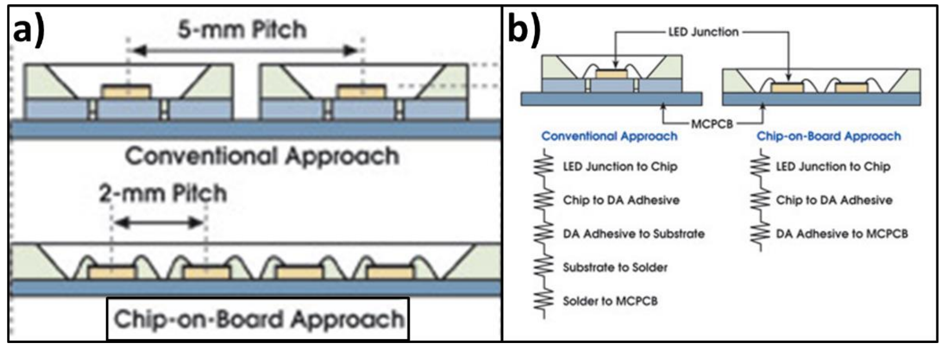

Figure 33: Comparison between the conventional discrete LEDs approach and the Chip-on-Board approach in terms of: a) spacing, b) thermal interfaces (Source: Avago Technologies).

Due to the large number of chip involved in these modules, they are usually configured in parallels of different series of LEDs, in order to maintain the operative voltage levels to values compatible with the commercially available driving systems. The entire module surface is then covered by a silicone gel that includes the phosphor particles. The substrates used in COB technology are mainly metallic or ceramic.

Chapter 2: LED metrology

2.1 Human vision

Lighting technology relies on the properties of human vision. The properties of vision determine the quantity and quality requirements for lighting. The primary process of vision occur in the eye, where the image is projected onto the retina. The retina comprises detector cells (receptors), which convert the energy of light into nerve impulses. The receptor are of two types, rods and cones. Rods exhibit higher sensitivity and play an important role in night vision, when the eye adapts to dark (scotopic vision). However, rods are not able to distinguish between colors since they contain only one type of photopigment. It is worth nothing that these receptor are concentrated outside the central part of the retina, thus being responsible for peripheral vision. Under conditions of high luminance, the response of rods is saturated, and vision is mediated entirely by cone receptor (photopic vision). Cones may contain one of three pigments: erythrolabe (long-wavelength cones), chlorolabe (middle-wavelength cones) and cyanolabe (short-wavelength cones). Owing to different spectral sensitivity, these photopigments allow us to distinguish colors. The density of cones is highest at the central part of the retina (fovea) and drops in the periphery.

Photopic vision has lower sensitivity but higher spatial diffusion. Due to the different photoreceptors involved, the spectral sensitivities of scotopic vision and overall photopic vision dier. The spectrum of scotopic sensitivity, which is determined by the photoresponse of rods and the transmittance of pre-retinal media, peaks in the blue-green region at a wavelength of 507 nm in air. The photopic spectrum is red-shifted with respect to the scotopic spectrum. The peak of the photopic sensitivity resides in the yellow-green region at a wavelength of 555 nm in air. Most human activities involve photopic vision, which is the most important from the point of view of

lighting technology. Therefore, much effort has been expended to calibrate and digitize the spectral response and color resolution of photopic vision. In 1924, the International Commission on

Illumination (CIE) introduced the relative luminous efficiency function, V(λ), for photopic vision. In 1951, a similar function, V'(λ), was introduced for scotopic vision. Both functions are depicted in Figure 34. The function V(λ) is defined in the range 380 to 780 nm. This wavelength interval of electromagnetic radiation is ultimately defined as the visible spectrum.

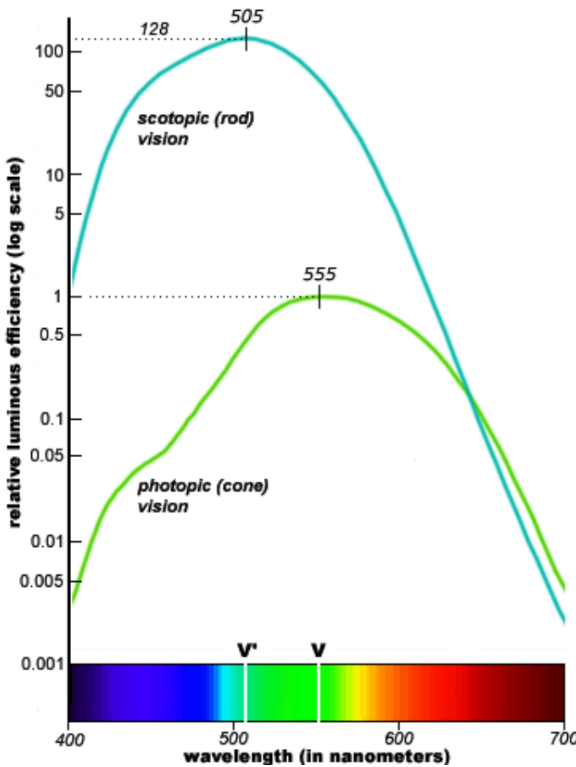

Figure 34: CIE 1951 scotopic luminous efficiency and CIE 1964 photopic luminous efficiency, normalized to the photopic sensitivity peak on semi-log scale [13].

2.2 Photometry

Photometry is the science of measuring visible light in units that are weighted according to the sensitivity of the human eye. It is a quantitative science based on a statistical model of the human visual response to light under carefully controlled conditions. The human visual system is a marvelously complex and highly nonlinear detector of electromagnetic radiation as showed in the previous chapter. Differently from radiometry, in photometry, we do not measure watts of radiant energy. Rather, we attempt to measure the subjective impression produced by stimulating the human eye-brain visual system with radiant energy.

This task is complicated immensely by the eye's nonlinear response to light. It varies not only with wavelength but also with the amount of radiant flux, whether the light is constant or flickering, the spatial complexity of the scene being perceived, the adaptation of the iris and retina, the psychological and physiological state of the observer, and a host of other variables.

Nevertheless, the subjective impression of seeing can be quantified for "normal" viewing conditions due to the CIE photometric curves showed in Figure 34, which provide the spectrum response of the eye/brain system to light radiation. These curves are used as weighting function to convert radiometric measurements in photometric quantities.

The foundations of photometry were laid in 1729 by Pierre Bouguer. In his *L'Essai d'Optique*, Bouguer discussed photometric principles in terms of the convenient light source of his time: a wax candle. This became the basis of the point source concept in photometric theory. Wax candles were used as national light source standards in the 18th and 19th centuries. England, for example, used spermaceti (a wax derived from sperm whale oil). These were replaced in 1909 by an international standard based on a group of carbon filament vacuum lamps and again in 1948 by a crucible containing liquid platinum at its freezing point. Today the international standard is a theoretical point source that has a luminous intensity of one *candela* (the Latin word for "candle"). It emits monochromatic radiation with a frequency of 540 x 1012 Hertz (or approximately 555 nm, corresponding with the wavelength of maximum photopic luminous efficiency) and has a radiant intensity (in the direction of measurement) of 1/683 watts per steradian. Together with the CIE photometric curve, the candela provides the weighting factor needed to convert between radiometric and photometric measurements.

Luminous flux is photometrically weighted radiant flux (power). Its unit of measurement is the *lumen*, defined as 1/683 watts of radiant power at a frequency of 540 x 1012 Hertz. As with luminous intensity, the luminous flux of light with other wavelengths can be calculated using the CIE photometric curve.

$$\phi_V(\lambda) = 683 \left[\frac{lm}{W}\right] * \int S(\lambda)\, V(\lambda)\, d\lambda$$

In this equation $\boldsymbol{\phi_V(\lambda)}$ is the luminous flux; S(λ) is the spectral power distribution and V(λ) is the CIE photopic luminosity function.

2.3 Colorimetry

The sensation of color is much more complex than sensation of brightness. A numerical description of colors relies on a very simplified model of human vision and therefore might disagree with certain subjective observations. Nevertheless, the basic concepts of colorimetry, such as tristimulus values, chromaticity coordinates, color temperature, and color rendering, are well formulated at present. These concepts are of crucial importance in describing light sources for lighting applications. Describing colors by certain numbers, tristimulus values emerged from the experimental fact that most color can be accurately imitated by a combination of not more than three appropriate primary colors (stimuli), such as red [R], green [G] and blue [B]. This makes possible to specify colors in amounts of three stimuli. However, some colors, which are close to monochromatic, fail to be matched by using only positive amounts of these stimuli and require negative amounts. This inconvenience was removed by introducing imaginary stimuli [X],[Y], and [Z]. The tristimulus values X,Y and Z are obtained by integrating the spectrum with the standard color-matching functions $\bar{x}(\lambda)$, $\bar{y}(\lambda)$ and $\bar{z}(\lambda)$, which are characteristics of an ideal observer (introduced by CIE in 1931):

$$X = \int S(\lambda)\, \bar{x}(\lambda)\, d\lambda \tag{1}$$

$$Y = \int S(\lambda)\, \bar{y}(\lambda)\, d\lambda \tag{2}$$

$$Z = \int S(\lambda)\, \bar{z}(\lambda)\, d\lambda \tag{3}$$

For convenience, the chromaticity coordinates (x,y) of a light source with a spectrum S(λ) were introduced:

$$x = \frac{X}{X + Y + Z} \tag{4}$$

$$y = \frac{Y}{X + Y + Z} \tag{5}$$

The third coordinate z contains no additional information since $z = \frac{Z}{X+Y+Z} = 1 - x - y$.

2.4 Color rendering

2.4.1 Metamerism

Chromaticity coordinates describe quantitatively the color of the radiating light source. Because of vision properties, the same coordinates may be obtained for a Plank radiator, for a combination of a few monochromatic sources, or for a source that irradiates a set of spectral lines. Sources with different spectrum but the same chromaticity are called metameric.

After the radiance is reflected from an illuminant object, the spectrum is altered in accordance with the reflectivity spectrum, resulting in a shift of the chromaticity coordinates (colorimetric shift). However, an object illuminated by metameric sources may appear visually as having different colors, since the reflectivity spectra will produce different colorimetric shifts for different spectral composition of the sources. Metamerism has presented a serious problem for lighting technology since discharge and fluorescent lamps were introduced. It should be noted that a quantitative description of the lighting quality is even more complicated because of the chromatic adaptation of the human eye (i.e. the ability of the human eye to correct for colors).

2.4.2 CIE Color Rendering Index (CRI)

The currently most used method of evaluating the ability of a light source to reproduce the colors of various objects is the CIE Color Rendering Index, introduced by the International Commission on Illumination in 1964 and revised in 1995. After reflecting from an illuminating object, the original radiation spectrum is altered by the reflection properties of the object (reflectivity spectrum). This results in a shift of the chromaticity coordinates, the so-called colorimetric shift. To estimate the quality of lighting, eight test samples are illuminated successively by the source to be tested and by a reference source. Other six color samples are used to provide supplementary information about the color rendering properties of the light source being tested. Of those six, four are highly saturated solids, and the other two are meant to represent a generalized Caucasian skin tone and the color of typical plant foliage. The reflected spectra from the sample are determined and the chromatic coordinates are calculated for both the tested and the reference sources. Then, the colorimetric shifts

are evaluated and graded with respect to chromatic adaptation of the human eye, using the 1960 CIE uniform chromaticity scale diagram, and the special CRI R_i for each sample is calculated. The general CRI R_a is obtained by averaging of the values of the eight CRI R_i:

$$R_a = \frac{1}{8}\sum_{i=1}^{8} R_i$$

In **Figure 35** are reported the fifteen Test Color Samples.

Name	Appr. Munsell	Appearance under daylight	Swatch
TCS01	7,5 R 6/4	Light greyish red	
TCS02	5 Y 6/4	Dark greyish yellow	
TCS03	5 GY 6/8	Strong yellow green	
TCS04	2,5 G 6/6	Moderate yellowish green	
TCS05	10 BG 6/4	Light bluish green	
TCS06	5 PB 6/8	Light blue	
TCS07	2,5 P 6/8	Light violet	
TCS08	10 P 6/8	Light reddish purple	
TCS09	4,5 R 4/13	Strong red	
TCS10	5 Y 8/10	Strong yellow	
TCS11	4,5 G 5/8	Strong green	
TCS12	3 PB 3/11	Strong blue	
TCS13	5 YR 8/4	Light yellowish pink (skin)	
TCS14	5 GY 4/4	Moderate olive green (leaf)	
TCS15	1 YR 6/4	Asian skin	

Figure 35: Reference Test Color Samples used for the CRI calculation.

Each lamp source being tested is matched to the output of a black body radiator (the standardized reference light source that can serve as a basis for lamp rating) of the same correlated color temperature (CCT), as long as that CCT is 5000K or lower. Above 5000K, the reference source is one in a series of daylight spectral energy distributions. Once plotted, the lamp is assigned a number from one to 100 on the CRI. Halogen incandescent is the only lamp source to achieve a rating of 100 since it is essentially a black body radiator. A rating of 80 or above is generally acceptable for commercial interior applications.

2.4.3 The CRI problems and the Color Quality Scale

Ohno [14] and others have criticized CRI for not always correlating well with subjective color rendering quality in practice, particularly for light sources with spiky emission spectra such as fluorescent lamps or white LEDs. Another problem is that the CRI is discontinuous at 5000 K, because the chromaticity of the reference moves from the Planckian locus to the CIE daylight locus. Davis and Ohno [15] identify several other issues, which they address in their Color Quality Scale (CQS).

The first issue is that the color space in which the color distance is calculated (CIEUVW) is obsolete and non-uniform and then they propose to use CIELAB or CIELUV instead. Also the chromatic adaptation transform used (Von Kries transform) is considered inadequate.

Another problem of the CRI method is that calculating the arithmetic mean of the errors diminishes the contribution of any single large deviation. Two light sources with similar CRI may perform significantly differently if one has a particularly low special CRI in a spectral band that is important for the application. For this reason Davis and Ohno propose to use the root mean square deviation instead. Moreover they suggest fifteen color samples with much higher chroma, which span the entire hue circle in approximately even spacing.

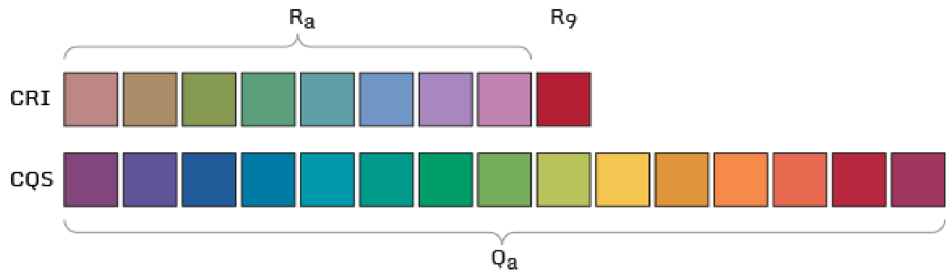

Figure 36: Comparison between the TCS used for the CRI and CQS calculation.

CRI measures the faithfulness of any illuminant to an ideal source with the same CCT, but the ideal source itself may not render colors well if it has an extreme color temperature, due to a lack of energy at either short or long wavelengths (i.e., it may be excessively blue or red). Weight the result by the ratio of the gamut area of the polygon formed by the fifteen samples in CIELAB for 6500 K to the gamut area for the test source. 6500 K is chosen for reference since it has a relatively even distribution of energy over the visible spectrum and hence high gamut area. This normalizes the multiplication factor.

2.4.4 Recent studies

Rea and Freyssinier have developed another index, the Gamut Area Index (GAI), in an attempt to improve over the flaws found in the CRI [16]. They have shown that the GAI is better than the CRI at predicting color discrimination on standardized Farnsworth-Munsell 100 Hue Tests and that GAI is predictive of color saturation. Proponents of using GAI claim that, when used in conjunction with CRI, this method of evaluating color rendering is preferred by test subjects over light sources that have high values of only one measure. Researchers recommend a lower and an upper limit to GAI. Use of LED technology has called for a new way to evaluate color rendering because of the unique spectrum of light created by these technologies. Preliminary tests have shown that the combination of GAI and CRI used together is a preferred method for evaluating color rendering. [17][18]

Pousset, Obein & Razet [19] developed a psychophysical experiment in order to evaluate light quality of LED lightings. It is based on colored samples used in the "Color Quality Scale". Predictions of the CQS and results from visual measurements were compared.

CIE [20]"reviews the applicability of the CIE color rendering index to white LED light sources based on the results of visual experiments." Chaired by Davis, CIE TC 1-69(C) is currently investigating "new methods for assessing the color rendition properties of white-light sources used for illumination, including solid-state light sources, with the goal of recommending new assessment procedures ... by March, 2010."[21]For a comprehensive review of alternative color rendering indexes see Guo & Houser [22].

Smet [23] reviewed several alternative quality metrics and compared their performance based on visual data obtained in 9 psychophysical experiments. It was found that a geometric mean of the GAI index and the CIE Ra correlated best with naturalness ($r=0.85$), while a color quality metric based on memory colors (MCRI[24]) correlated best for preference ($r=0.88$). The differences in performance of these metrics with the other tested metrics (CIE Ra; CRI-CAM02UCS; CQS; RCRI; GAI; geomean(GAI, CIE Ra); CSA; Judd Flattery; Thornton CPI; MCRI) were found to be statistically significant with $p<0.0001$.

Dangol et al [25] performed psychophysical experiments and concluded that people’s judgments of naturalness and overall preference could not be predicted with a single measure, but required the joint use of a fidelity-based measure (e.g., Qp) and a gamut-based measure (e.g., Qg or GAI.). They carried out further experiments in real offices evaluating various spectra generated for combination existing and proposed color rendering metrics (see [26] for details).

Chapter 3: LED reliability

One of the most basic decision factors for light source selection is reliability: long lifetime is a key advantage of LEDs over other light sources. However, the lighting industry currently has very limited direct experience with long-term performance and reliability of solid-state light emitting devices.

The most effective way to predict LEDs lifetime and analyze their reliability performances consists in accelerating the aging process through various stress conditions. The correct application of this aging procedure and the interpretation of results requires a deep knowledge of materials properties and of degradation/failure mechanisms of devices.

Recent research works have revealed that there are many processes that limit reliability of LEDs with respect to the lifetime values. These processes involve all physical, electrical and optical properties of the device and of the complete lighting system. Referring to GaN based LEDs, the most common degradation processes are:

- generation of non-radiative defects in the active layer;
- degradation of the ohmic contacts;
- degradation of the transparency characteristics of the epoxy and package materials due to the high temperatures and/or the short-wavelength irradiation;
- browning of the phosphorous material and the drop in their conversion efficiency as consequences of high-temperature treatment;
- shortening of the p-n semiconductor junction as a consequence of an ESD event;
- catastrophic failure due to Electrical-Overstress phenomena.

There is a significant number of works that report the results of aging tests at high-temperatures demonstrating the influence of temperature on reliability of SSL devices and highlighting the importance of thermal design of LED-based light sources.

3.1 Generation of non-radiative defects

This phenomenon occurs both at high and at low level of current injection. In that conditions hot carriers can transfer enough energy to the lattice displacing the atoms and breaking the metal-N bonds. For InGaN/GaN light emitting diodes is plausible that the thermally assisted defect formation occurs primarily in the InGaN layers because the bonding energy of InN is considerably smaller [27]. Non-radiative recombination processes in the active region could also enhance the defect formation: when an electron is captured by a defect level with a subsequent capture of a hole, multi-phonon emissions occur. This will result in strong vibration of the defect atoms and reduce the energy barrier for the defect motion such as migration, creation or clustering.

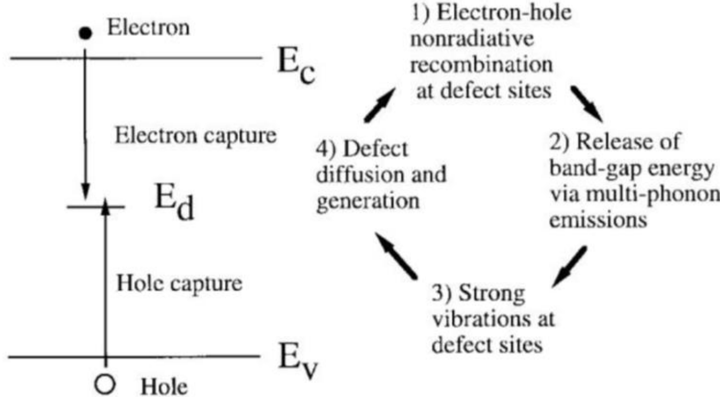

Figure 37: Energy-band diagram showing the capture of an electron with a subsequent capture of a hole at a defect site that causes strong defect vibrations and results in defect generation.[28]

At high currents, the non-radiative recombination paths can saturate and their effects on overall light output is limited, as shown in [29]. This behavior can be explained with use of the continuity equation for the injected electron density:

$$\frac{dn}{dt} = \frac{J_n}{qx} - An - Bn^2$$

where the first term $\frac{J_n}{qx}$ is the current injection rate, the second term An is the non-radiative recombination rate and the last term Bn^2 is the radiative emission rate. J_n is the current density, q the electron charge, x the thickness of the active layer, and A and B are the non-radiative and radiative recombination coefficients, respectively. It is assumed that the electron and hole concentrations are equal in the active region of the LED. At steady-state conditions $\frac{dn}{dt} = 0$, the light emission intensity

L at low forward current where non-radiative recombination of carriers is dominating ($An \gg Bn^2$) , can be defined as:

$$L = Bn^2 \approx \left(\frac{B}{A^2}\right)\left(\frac{J_n}{qx}\right)^2$$

In this last equation the light output L is quadratic with current density, J_n, representing the low current region. As the current density increases the radiative recombination of carriers start to dominate ($Bn^2 > An$), and the light intensity L increases linearly with current density until the current induced heating effect appears.

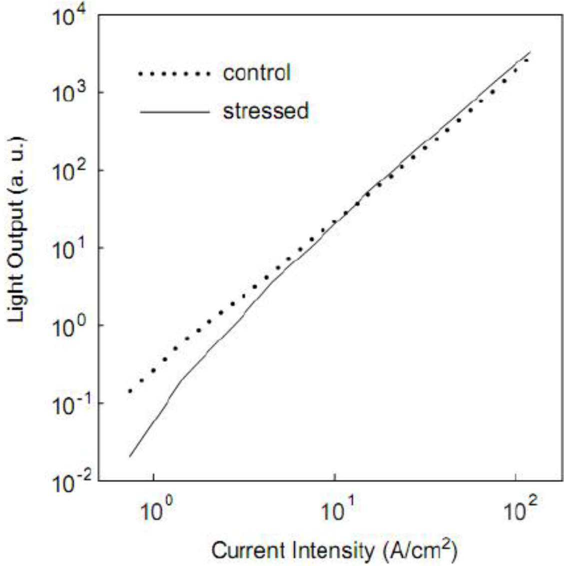

Figure 38: L–I characteristics before and after 120 h forward-current stress.[27]

In the continuity equation for the injected electron density the non-radiative recombination coefficient A can be expressed by the Shockley Hall Read recombination rate:

$$A = N_T v_{th} \sigma$$

where N_T is the defect density of traps, v_{th} the carrier thermal velocity and σ the electron capture cross section. For simplicity, we assume that the thermal velocities and the capture cross sections are equal for both electrons and holes.

From the last equations is easy to see that the total light intensity reduction, caused by an increased defect density N_T , is more relevant where non-radiative recombination of carriers is dominating, i.e. for low levels of current injection. The same behavior is visible in the I-V characteristics (Figure 39):

the defect generation in the active layer increase the non-radiative recombination rates and thus the current. This excess current component becomes less visible in the high-voltage region as the radiative recombination is dominating over the non-radiative.

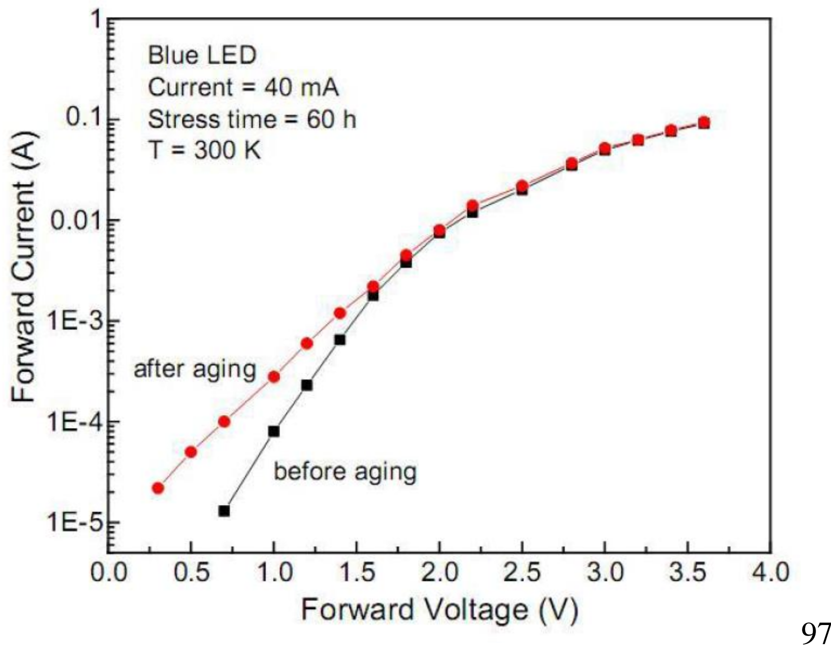

Figure 39: I-V characteristics before and after aging.[35]

3.2 Degradation of the ohmic contacts

Recently has been shown [31],[32], that a high temperature treatment induce the worsening of the electrical characteristics of the ohmic contact. Specifically, some studies [36],[37] have demonstrated the importance of interaction between the semiconductor and Hydrogen in the degradation of ohmic contact to the p-side. Due to the use of H_2 as a flow gas in MOCVD (MetalOrganic Vapour Phase Epitaxy) reaction, Hydrogen is the most present impurity in GaN layers. H_2 itself is chemical inactive, but ionic form of the element: H^+ and H^- are very reactive with Magnesium atoms. High temperatures allows this hydrogen to interact with the surface of the devices, binding with magnesium, generating Mg–H complexes and worsening the properties of the p-GaN layer and of the p-side ohmic contact.

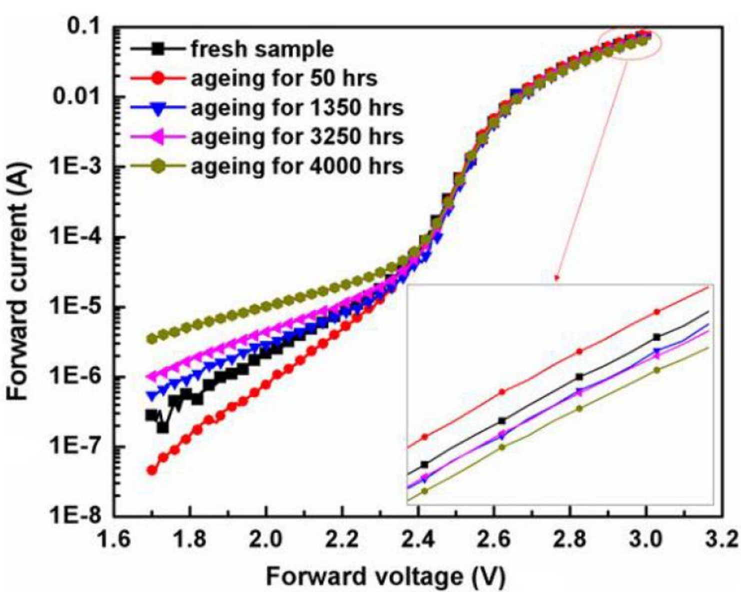

Figure 40: A semi-log plot of the I–V characteristics samples in the ageing process. The inset graph is an enlarged view of the currents at high currents.[33]

As shown in Figure 40, the thermal treatment induces an increase of both the contact and semiconductor sheet resistivity, as well as the non-linearity of the I-V curves. In this figures it is evident that the operating voltage increase is not only due to the increase of the series resistance of the device: in fact, changes in the I-V curves are present also in the low-current region (I < 1mA) i.e. where a small series resistance does not significantly affect the voltage drop across the LED. As a consequence of the modifications of the increased resistivity of the contact and semiconductor layer, emission and current crowding are detected after high-temperature treatment, since the current finds a preferential, low resistance path where the bonding pad is located (Figure 41).

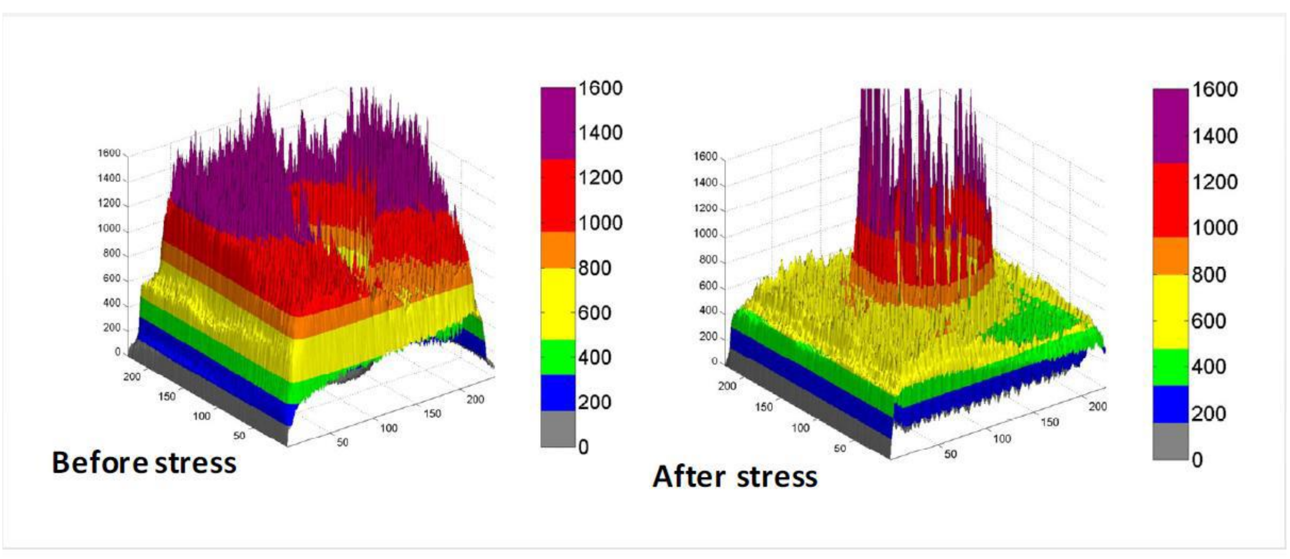

Figure 41: Emission profiles of the same LED measured before and after 250 °C stress.[30]

In [31] has been shown that the stress of the LEDs induces the degradation of the properties of the ohmic contacts, rather than a worsening of the characteristics of the p-type material. The most important degradation process is the worsening of the metal/semiconductor interface: on the other hand, the sheet resistance of the p-GaN layers is thought to be affected by stress test only in a minor way.

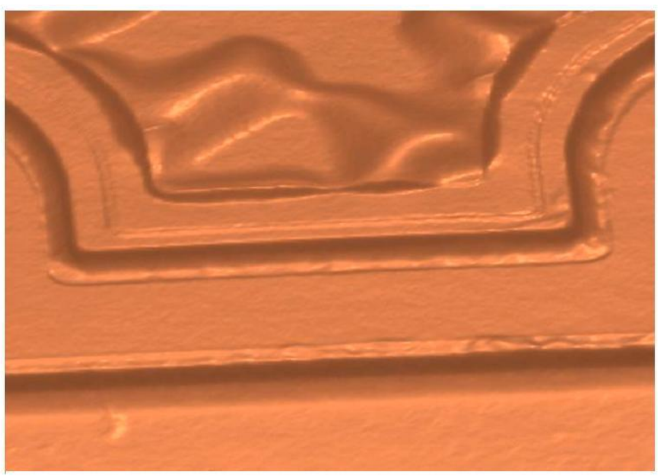

Figure 42: Partial detachment of an ohmic contact detected as a consequence of stress at high current levels.

High temperature/current flow can also induce a morphological degradation of the contact layers. Recent reports [38] highlighted that some kinds of LEDs can show a partial detachment of the contact metallization because of high stress conditions due to the poor adhesion between different metal layers and/or to the thermal mismatch between the different materials used for the realization of the contacts (Figure 42).

3.3 Changes in the optical properties of the encapsulant material

Although many studies have investigated the degradation of GaN-type LEDs, very few studies have analyzed the degradation of packaged white LEDs. According to the few that have studied the packaged devices (blue and white LEDs), the primary reason cited for the rapid degradation of light output is the yellowing of the epoxy encapsulant. Excessive heat at the p-n junction is pointed as the main cause of epoxy yellowing . Ambient temperature and the ohmic heating at the band-gap add up to create the heat at the LED junction. Polymeric materials and epoxies also yellow over time due to photo-degradation. This topic has been studied extensively by many polymer chemists. Although

ultraviolet (UV) radiation with wavelengths less than 300 nm has the strongest effect on the yellowing of polymer materials in photo-degradation, it has been shown that even visible light in the range of 400-500 nm induces photo-degradation. The amount of photo-degradation depends on the amount of radiation and time of exposure. Therefore, even visible light of sufficient quantity can cause polymer and epoxy materials to degrade.

Meneghesso et al. investigated the reliability of GaN-based blue and white LEDs in plastic package during the accelerated aging tests, and determined the package-related failure modes [39]. Hwang et al. made failure analyzes of plastic packaged LEDs and believed that the hygroscopic plastic is mainly responsible for the device failure [40]. Mura et al. observed silver-sulfur compounds on the lead frame in the plastic encapsulation and blamed it for electrically open and degradation of electrical properties [41].

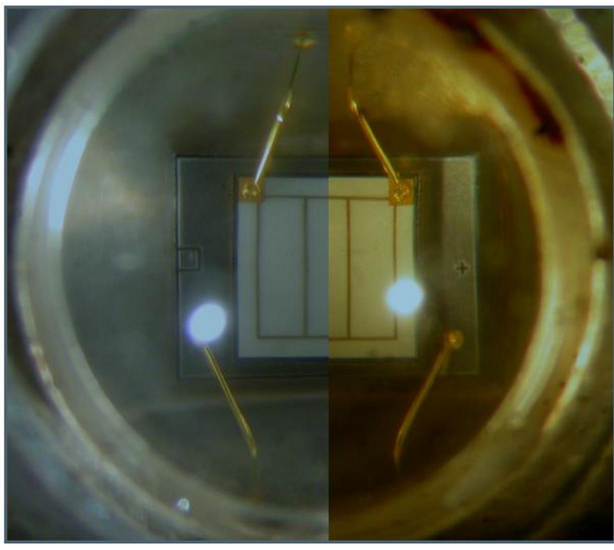

Figure 43: An example of yellowed package after stress at 200°C. [42]

The existence of a large amount of C element probably is the cause of die surface darkening and light transmittance declining. High-power blue LED has a good performance, stable surface properties and does not generate black materials. In a real LED packaging, under the circumstance of the blue light radiation, high temperature and a small amount of oxygen, epoxy resin will be gradually fading, and massive C - O and C = O bonds open, and dissociative C and O atoms occurs on the die surface. Finally a large amount of carbon or carbon oxide attaches on the interface between the die and the glue, resulting in a black zone and die surface darkening (see Figure 44).

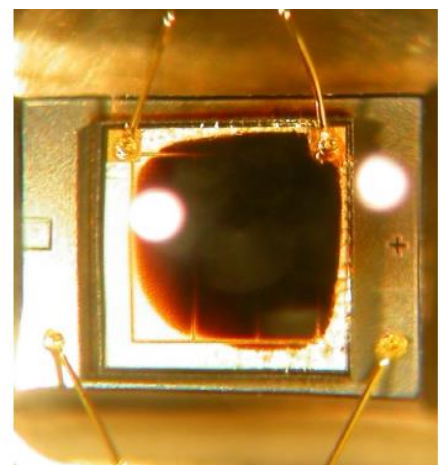

Figure 44: An example of die surface darkening.[42]

3.4 Chemical compatibility

Most of the currently available LEDs contains silicone encapsulants and silicone lenses and then care must be taken to avoid any incompatible chemicals from directly or indirectly reacting with silicone as showed in the previous section. In fact, most of the silicone encapsulants are gas permeable. Then, oxygen and volatile organic compound (VOC) molecules can diffuse into the silicone overcoat. VOCs may originate from adhesives, solder fluxes, conformal coating materials, potting materials and even some of the inks that are used to print the PCBs.

Any VOCs present in an SSL system can diffuse into the gas-permeable silicone lens and encapsulants of the LED. Within the molecular structure of these silicone materials, the VOCs will occupy a free space in the interwoven silicone polymer. With subsequent exposure to high photon energy emitted from the LED, along with the heat from the lighting system and the environment, the volatile compounds trapped in the LED‘s lens or encapsulants can discolor. This discoloration of the trapped VOCs can degrade the light emitted from the LED. This discoloration tends to occur in blue, royal blue and white-light producing LEDs that use blue wavelength LED chips with yellow phosphors for spectrum conversion. This sensitivity to VOCs is not unique to one LED manufacturer but is a known problem for all types of blue, royal blue and white-light LEDs. Chemically induced discoloration is less prevalent and not as noticeable with amber, red and green LEDs since these color LEDs have longer wavelengths and therefore a lower frequency and produce lower photonic energy compared to blue LEDs. Photonic energy (E) is defined by the Planck-Einstein equation of $E = hf$,

where h is Planck's constant and f is frequency, thus a higher frequency produces a higher photonic energy.

In Table 1 is reported a list of chemicals that can damage the silicone lenses, provided by Philips Lumileds [44].

Table 1: List of commonly used chemicals that will damage the silicone lens [].

Chemical name	Normally used as
hydrochloric acid	acid
sulfuric acid	acid
nitric acid	acid
acetic acid	acid
sodium hydroxide	alkali
potassium hydroxide	alkali
Ammonia	alkali
MEK (Methyl Ethyl Ketone)	solvent
MIBK (Methyl Isobutyl Ketone)	solvent
Toluene	solvent
Xylene	solvent
Benzene	solvent
Gasoline	solvent
Mineral spirits	solvent
dichloromethane	solvent
tetracholorometane	solvent
Castor oil	oil
lard	oil
linseed oil	oil
petroleum	oil
silicone oil	oil
halogenated hydrocarbons	misc
rosin flux	solder flux
acrylic tape	adhesive

3.5 Degradation of the phosphorus encapsulant

Many past studies have shown that the phosphor-converted white LED degrades faster than the similar type of blue LED. The main difference between a blue and a similar white LED is the phosphor that is mixed in with the epoxy or conformally coated on the chip. In [43] this phenomenon is explained by measurements of the emitted spectra: in Figure 45, where is showed the output spectra (normalized to the blue peak) of a white led during stress at 200°C, it is clear that there is a strong decrease of the yellow emission, with respect to the main blue peak.

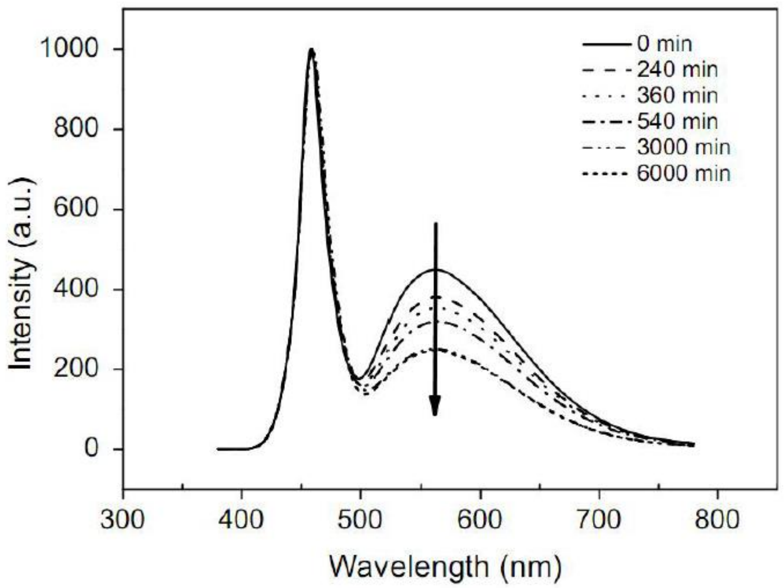

Figure 45: Normalized output spectra of a white led before and during stress at 200 C.[43]

Another estimate of the deterioration of conversion efficiency of phosphor is given by the example of Figure 46: this graph shows the kinetic of the yellow/blue ratio (the ratio between the integral of the yellow spectrum and the integral of the blue one) compared to the optical power decrease.

Furthermore, during high-current aging tests, the surface of phosphors sometimes shows a visible darkening (Figure 47) with subsequent decay of the optical power. This blackening can be attributed to excessive overheating of the chip and to the resulting high thermal gradient at the interface between chip and phosphors. In addition, also UV/blue radiations can contribute to the formation of these dark spots.

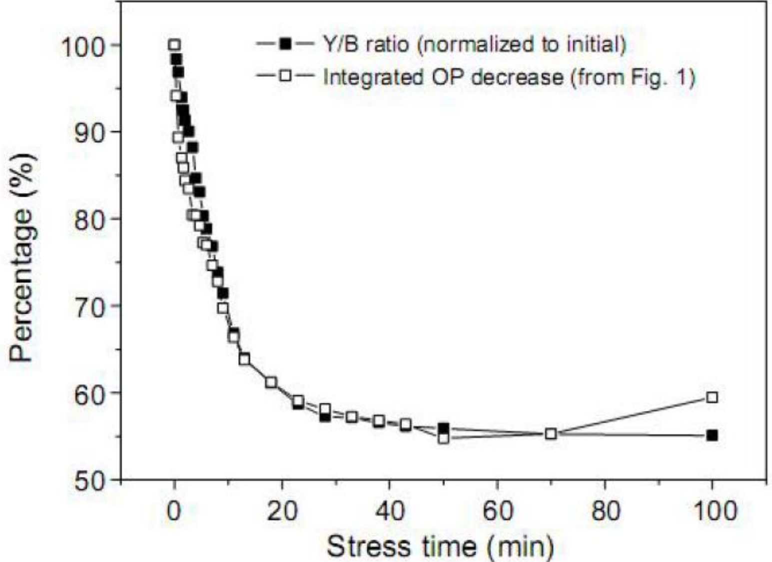

Figure 46: Typical Yellow/Blue ratio variation measured during stress at 200 C. In figure is also reported the correspondent integrated optical power loss kinetic.

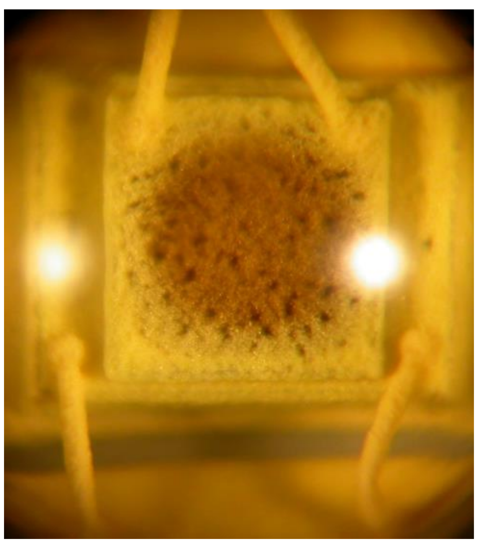

Figure 47: An example of phosphors darkening after 32h of stress at 1A/120°C. [42]

Chapter 4: “Hot-plug” on LED modules

The aim of the work presented in this chapteris to investigate on one of the most critic, but underrated, electrical overstress (EOS) event on LED modules: the “hot-plug” connection of a LED module to a previously energized power supply. This type of connection can lead to the generation of in-rush current spikes up to several tens of amperes. The characterization of the phenomenon, carried out with different types of LED drivers and LED modules, has revealed that the current spikes level and the duration are directly related to the electrical characteristics of the power-supply output stage (capacitance and open-circuit voltage) and to the number of LEDs connected in series. An equivalent electrical model is proposed, simulated and then replicated with discrete components in order to confirm the hypothesis that the in-rush current spikes during the “hot-plug” connection are generated by the discharge of the output capacitance of the LED driver through the LED chain.

4.1 Introduction on the “Hot-plug” phenomenon

Over the last decade the improvement of the performances and of the reliability of GaN-based light emitting diodes has led to a very mature technology capable to meet the needs of many different application fields in the lighting scenario. Despite the excellent robustness showed by modern LED technology, there are several limitations to the devices lifetime, especially related to the “electrical overstresses”(EOS) phenomena (i.e. power-on/power-off transients, overdriving, power surges etc.). It is well known that an excessive operating current accelerate the LED degradation mechanisms and then reduce the devices lifetime [45][46][47]; despite the limited duration of the EOS events, they can be potentially destructive due to the high current/voltage levels generated. The importance of this topic is confirmed also by the various documents published by the LED manufacturers [48][49], which suggests several methods to prevent the devices failure due to EOS events.

In this section we will show the characterization a particular type of EOS phenomenon which is generated by the so-called “hot-plug” connection: it consists by the accidental connection of a LED

module to a previously energized power supply; this lead to the generation of in-rush current spikes that can reach current levels up to several tens of amperes. Despite the importance of this topic, the scientific community has never focus its interest in understanding the real nature of the in-rush current spikes during this event. The hypothesis proposed in this work derives from the most simple interpretation of the phenomenon: the in-rush current spikes may be the consequence of the discharge of the output capacitance of the LED driver. In fact, commercially available LED driver has large capacitor (>100μF) at the output stage in order to stabilize the generated current waveform. When the power supply is energized without any load, this capacitor is charged at the maximum voltage reachable by the LED driver, which can be higher than the forward voltage required by the LED module. Then it is plausible to suppose that when the LEDs are connected, the capacitor discharge all the stored energy through the LED chain by generating a high current peak.

In order to confirm this hypothesis, we have measured the in-rush current waveforms generated by different LED drivers with different output characteristics (capacitance and maximum voltage) by varying also the configuration of the connected LED module. This has allowed to determine a correlation between the current pulse shape (peak level and duration) and the different parameters of the driver/LEDs system.

The second step of this work consists in the modelization of the LEDs electrical behavior, in order to simulate the capacitor discharge and compare the simulated waveforms with those measured. The in-rush current spikes were then successfully replicated with discrete components, such as electrolytic capacitors and LEDs.

4.2 Experimental details

In order to measure the current waveform generated during an "hot-plug" event, the experiment was carried out by means of a mono-stable DPDT (double pole, single throw) mechanical switch which simultaneously connect the two output wires of the LED driver to the anode and cathode of the LED series. The current waveforms were measured through a magnetic current clamp with a maximum current of 120 A and a bandwidth of 100 kHz connected to a digital oscilloscope.

In order to understand the relationship between the in-rush current spikes and the characteristics of the power supply, three commercially available LED driver were tested with different output voltages and different output capacitance. All the three LED driver are designed to supply a constant current of 350 mA. In Table 2 are summarized the output characteristics of the tested LED driver.

The LED modules used for the tests were constituted by series of three different white power-LEDs chosen by the catalogue of three of the leading manufacturers. The number of LEDs connected in series varies from 3 to 19, in order to study the different behavior of the LED drivers in different load conditions. The main characteristics of the three LEDs types are reported in Table 3.

Table 2: LED drivers: output characteristics.

	Output MAX Voltage	**Output capacitance Cout**
Driver 1	48 V	168 µF
Driver 2	36 V	294 µF
Driver 3	56 V	314 µF

Table 3: LEDs characteristics.

	Forward Voltage @350mA	**Maximum current**	**Flux @350mA**	**CCT**
Type A	2.9 V	1 A	114 lm	6200 K
Type B	2.95 V	800 mA	90 lm	3000 K
Type C	2.9 V	1.5 A	110 lm	2700 K

4.3 Current waveform analysis

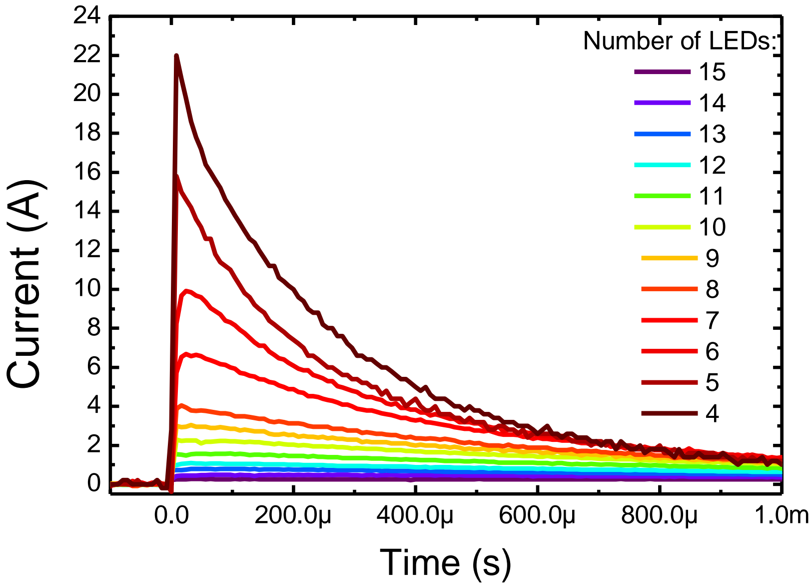

Figure 48: An example of hot-plug waveforms comparison by varying the number of LEDs connected in series (Driver 1, LED Type A White).

In order to study the in-rush current spikes characteristics in different conditions the “hot-plug” connection are repeated with the same LED driver connected to modules with decreasing number of LEDs: in Figure 48 are reported the in-rush current spikes generated by the Driver 1 with Type A LEDs. It is clear that, when the number of LED is higher, the current rise is inappreciable, whereas the peak reach levels up to 20 A at lower number of LEDs. The same behavior is visible also with Driver 2 and 3 as showed by Figure 49.

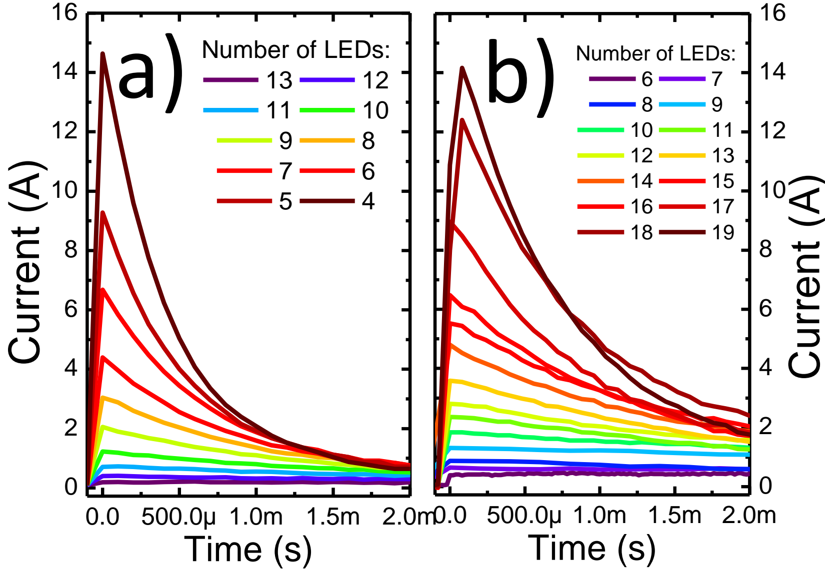

Figure 49: Hot-plug waveforms comparison by varying the number of LEDs connected in series: Type A LED - a) Driver 2 b) Driver 3

These measurements allows to plot the peak current level as a function of the number of LEDs connected in series: Figure 50 shows that there is an exponential decay of the peak current at higher number of LEDs; the comparison between the three LED drivers in Figure 50 highlights that the behaviors are almost the same, except for a right translation proportional to the output voltage of the power supplies. This behavior is compatible with the hypothesis of the capacitor discharge: as we will see in the following chapter, the current peak level during the discharge of a capacitor through a resistance depends only by the initial voltage and by the resistance value and is uncorrelated with the capacitance value as in this case.

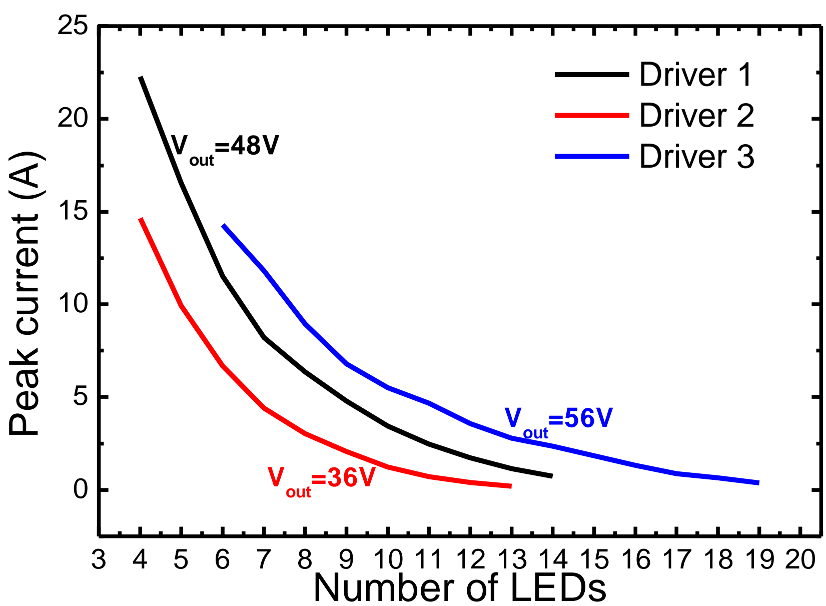

Figure 50: Comparison between the peak amplitude as a function of the LEDs number with the three different LED drivers (LED Type A).

Since the LED chain is the resistive path that allows to discharge the output capacitor, it is extremely interesting to compare the in-rush current spikes by using different types of LEDs with slightly different electrical characteristics. In Figure 51-a is reported the peak amplitude as a function of the number of LEDs carried out with the same LED driver (Driver 1) on the three different LED types. By comparing these three curves with the Voltage-Current (V-I) characteristics showed in Figure 51-b, it is evident that the device with the higher forward voltage (Type B) is the one that triggers a lower peak current level, whereas the LED with the lower forward voltage (Type C) has an higher current level during the “hot-plug” connection. This highlights that the in-rush current level is strictly related to the V-I characteristic of the load connected to the output stage of the LED driver; in other words, the resistance showed at the LED module terminals, together with the open-circuit voltage of the power supply, controls the initial part of the current transient during the “hot-plug” connection.

In the evaluation of an over-current event, the maximum current level is not the only important parameter: the duration of the current pulse is also a key factor in determine the impact of the phenomenon on the devices under test.

In the case of the in-rush current spikes generated during the “hot-plug” event, it is evident an exponential decay of the current waveform (see Figure 48); for this reason the time-based analysis of the current waveform were carried out through the calculation of the time constant associated to the first order exponential decay function.

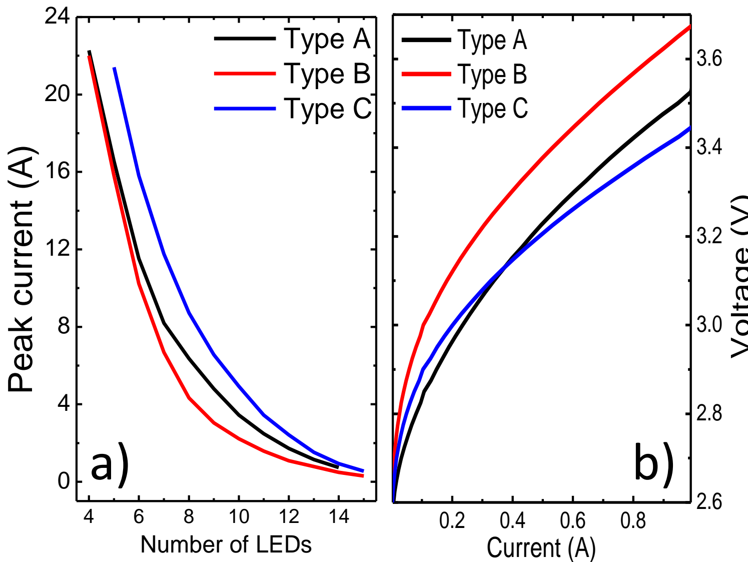

Figure 51: a) Peak current as a function of the number of LEDs; b) V-I characteristic comparison between the three tested LED types.

The comparison between the calculated time constants on the three different LED drivers (Figure 52) shows that the time constants are strictly related both to the number of LEDs and to the output capacitance value of the LED driver. Since it seems that the higher is the output capacitance, the higher are the time constants, it is natural to associate this type of current exponential decay to the discharge of the output capacitance.

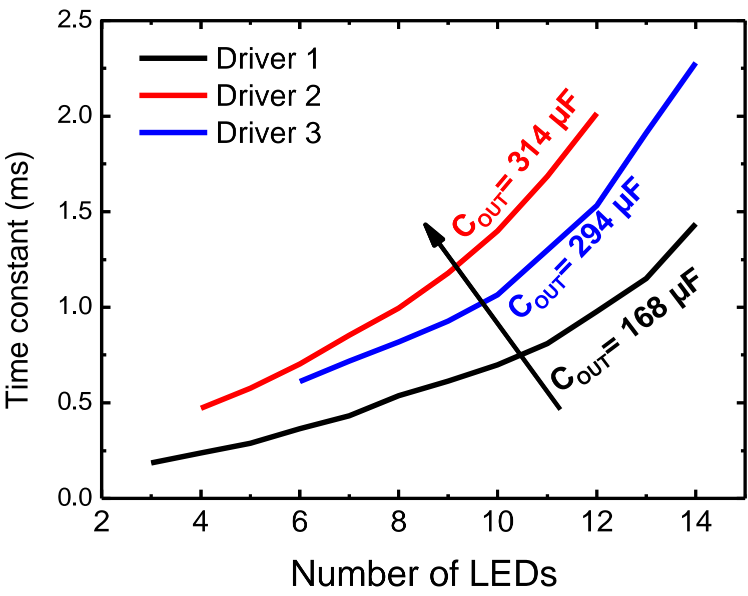

Figure 52: Time constant as a function of the number of LEDs for the three different drivers. Over the lines the corresponding output capacitance values are reported.

4.4 Modelization and simulation

The equation that rules the current waveform ($I(t)$) during the discharge of a capacitor (C) through a resistance (R) is the following:

$$I(t) = \frac{V_0}{R} \exp\left(-\frac{t}{\tau}\right)$$

where τ = RC and V_0 is the initial voltage (t=0) at the capacitor terminals; in this case V_0 corresponds to the output maximum voltage of the LED driver.

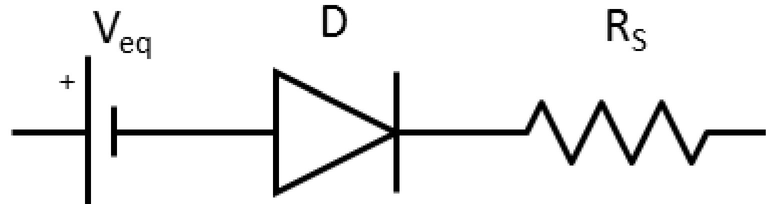

Figure 53: The proposed LED equivalent model for the in-rush current characterization.

For the modelization of the "hot-plug" phenomenon we decided to use the most simple LED equivalent circuit (Figure 53) which is constituted by the series of a resistor (R_S), an equivalent voltage generator (V_{EQ}) and an ideal diode (D). This representation of each LED was implemented in the Pspice simulator by using resistance/voltage values and diode characteristics provided by the LED manufacturer.

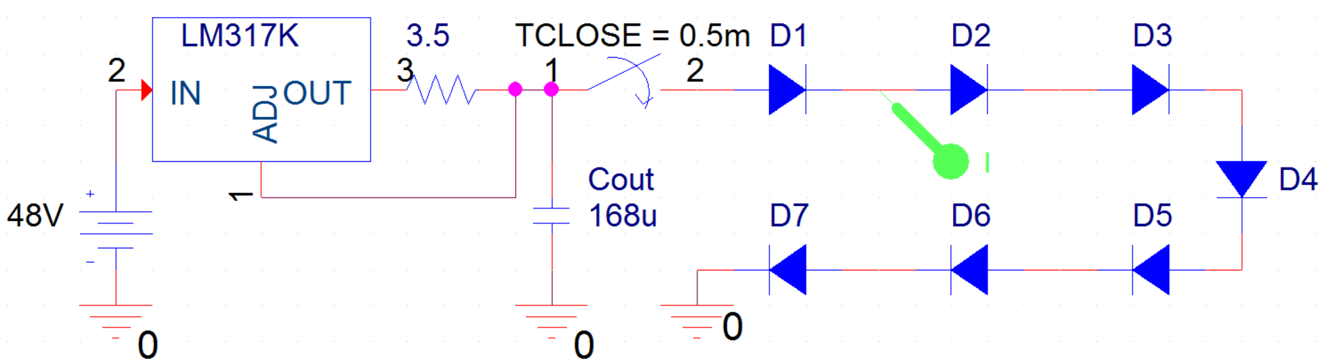

Figure 54: The Pspice schematic used for the simulation.

The Pspice schematic of Figure 54 is used to verify if the in-rush current spikes are generated exclusively by the discharge of the output capacitance; as visible in the schematic, there is a simple capacitor, with the same capacitance value of the Driver 1, charged with a linear regulator and connected to the LEDs chain through a switch. The simulation was repeated with different numbers of LEDs in series and the current spikes simulated with this model are very close to those measured both in terms of peak amplitude (Figure 55) and time constants (Figure 56). The only difference in the two results are visible in the right part of Figure 56 and it is associable to the different supply techniques adopted (LED driver/linear regulator): in fact, as the number of LEDs increases , the pulse duration is so reduced that the driver has the time to recharge the capacitor and then the time constant became slightly related to the “charging” circuitry characteristics.

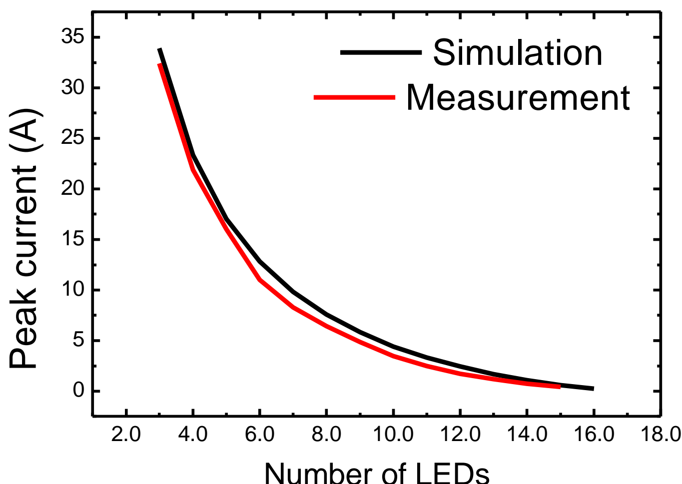

Figure 55: Comparison between the simulated and measured peak current as a function of the number of LEDs. (Type A LED – Diver 1).

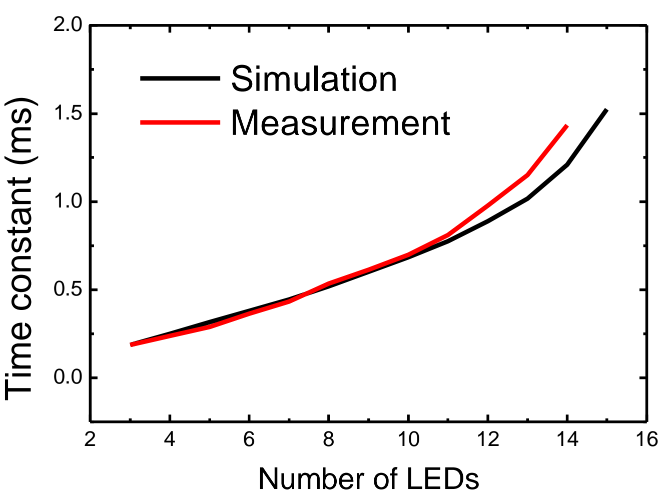

Figure 56: Comparison between the simulated and measured time constant as a function of the number of LEDs. (Type A LED – Diver 1)

4.5 "Hot-plugging" with discrete components

In order to give another confirmation of the thesis that the in-rush current spikes are generated only by the output capacitor discharge, we decided to compare the pulse time constants measured with the different LED drivers and those generated by the discharge of two discrete electrolytic capacitors, with capacitance values of 100µF and 180µF. These capacitors are charged with a laboratory power supply and then connected to the LED chain through a DPDT switch.

In order to obtain comparable values, the time constant values must be normalized by the different capacitance values $\left(\frac{Time\ constant}{C_{out}}\ [s/F]\right)$. The results of this comparison are showed in Figure 57 Figure 58; as clearly visible, the ratio $\frac{Time\ constant}{C_{out}}$ measured with the discrete capacitors are almost equal to those generated with the LED drivers, especially when the number of LEDs are lower.

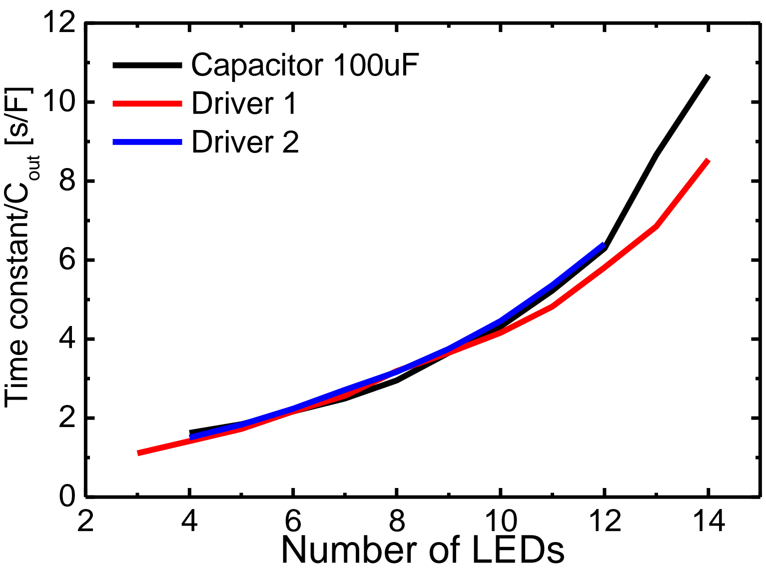

Figure 57: Comparison between the Time constant/C_{OUT} ratio measured with two LED drivers and with the 100µF capacitor.

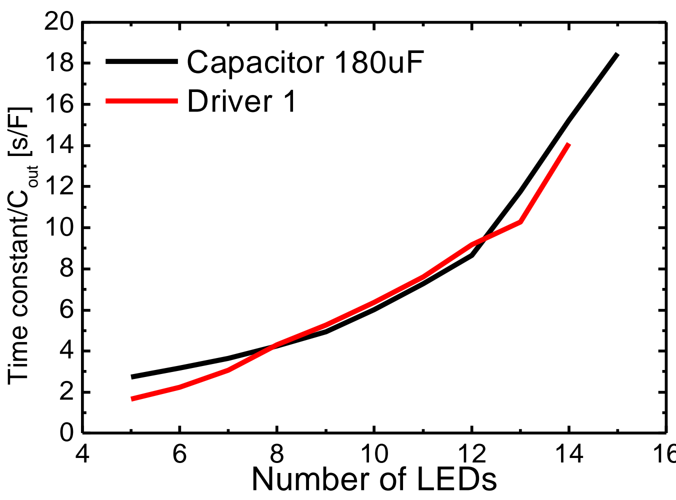

Figure 58: Comparison between the Time constant/C_{OUT} ratio measured with two LED drivers and with the 180μF capacitor.

4.6 Discussion and conclusions

This work presents an extensive analysis on the causes of the current spikes generation during the hot-plug phenomenon. A more complete knowledge of this topic can be helpful, especially in those areas where, for cost or space reasons, the protection structures or soft-start circuitry are not available.

Measurements presented in this chapter have showed that the in-rush current level is directly related to the output voltage of the power supply and to the electrical characteristics of the LED module. Moreover, the time constants analysis has revealed the influence of the driver output capacitance in the duration of the current spike.

These results suggest that the generation of the in-rush current spikes is caused only by the discharge of the output capacitor of the LED driver. In fact, commercially available LED power-supply have usually a big electrolytic capacitor (COUT > 100μF) connected in parallel to the output terminals, which has the purpose of limiting the ripple of the supplied current. When the LED driver is energized without a load, this capacitor is charged at the maximum voltage (V_{OUT}) reachable by the driver. Then, when the LED series is connected, the capacitor discharges starting from V_{OUT}; since V_{OUT} is usually higher than the voltage necessary to bias the LED chain at the selected current, the initial discharge generates high current spikes as showed in Figure 48 and Figure 49. In order to provide other confirmations to this hypothesis we decided to simulate the capacitor discharge and to reproduce the phenomenon with discrete components. Both the simulation and the measurements on a single

capacitor have showed the same exact in-rush current spikes generated during the hot-plug phenomenon.

All of the results presented in this section lead to the conclusion that the in-rush current spikes during an hot-plug connection are generated only by the discharge of the output capacitor of the LED driver. This confirmation is extremely important both for the power-supply designers and lamps manufacturers, because it allows to safely predict the behavior of the lighting system during the accidental hot-plug connection. Moreover, this suggests that the minimization of the output capacitance of the LED driver and the proper choice of the maximum output voltage can be sufficient to completely avoid the LEDs failure during an hot-plug event.

Chapter 5: ESD on GaN-based monochromatic LEDs

This chapter presents an extensive study on the effects of Electrostatic Discharges (ESD) on state-of-the-art GaN based LEDs, based on optical and electrical measurements carried out during the ESD events. ESD events were simulated through a Transmission Line Pulser (TLP) which generates voltage pulses with a duration of 100ns and increasing amplitude: during each pulse, spatially-resolved electroluminescence measurements were carried out through an high speed EMCCD camera. These measurements allowed to identify the chip region where the discharge is localized and the change in the damaged area induced by consecutive ESD events. The current and voltage waveforms at the LED terminal were also monitored during the tests; this analysis provided important information about modifications the impedance of the devices. The analysis was carried out on different types of commercially available low-power GaN-based LEDs with several differences in the manufacturing technology. Thanks to these tests we have identified two different failure behaviors during a destructive ESD event, clearly related to the different defects in the semiconductor lattice and to structure of the chip.

5.1 Introduction

The excellent robustness achieved by modern LEDs allows to reach lifetimes in excess of 30-50,000 hours ([50]-[53]) under proper operating conditions. However, electrostatic discharges (ESD) still represent one of the most critical issues affecting the reliability of GaN-based LEDs. In fact, each LED is potentially exposed to Electrostatic discharges throughout all its lifetime, starting from the manufacturing and assembly process, to real-life operation; such ESD can lead to the catastrophic failure of the devices.

Despite the importance of this topic, only few papers have investigated the physical mechanisms responsible for the failure of LEDs submitted to ESDs (see [54]-[57]); more specifically, the correlation between device structure, epitaxial quality, and ESD robustness still has to be assessed.

The aim of this work is to present an innovative methodology to analyze the ESD failure of LEDs, based on dynamic measurements of the Electroluminescence (EL) and of current/voltage waveforms of the devices executed during the ESD event.

The EL images provide a description of the chip region where the discharges are localized and the changes in the damaged region introduced by consecutive pulses. The nature of the modifications on the electrical characteristics of the devices were also evaluated by the analysis of the pulse waveforms: in fact, during the ESD failure significant variations of the LED impedance highlight the effects of the high-current flow on the semiconductor lattice structure. With this method we have identified two different failure mechanisms associated to layout and epitaxial quality of the two types of LEDs under test.

5.2 Experimental details

We studied two different types of low-power commercially available GaN-based LEDs fabricated by a leading manufacturer. Despite they belong to the same device family (same package and same chip size), the two LEDs differ both in the indium content in the quantum wells (thus having different emission wavelengths) and in the layout of the upper contact:

- Type A LEDs have an emission wavelength of 470 nm (BLUE) and a thick grid-shaped metal contact that helps to spread the current at top contact of the die;

- Type B LEDs have an higher emission wavelength (570nm, GREEN) and the upper contact is realized with a simple bond-pad (see Figure 59).

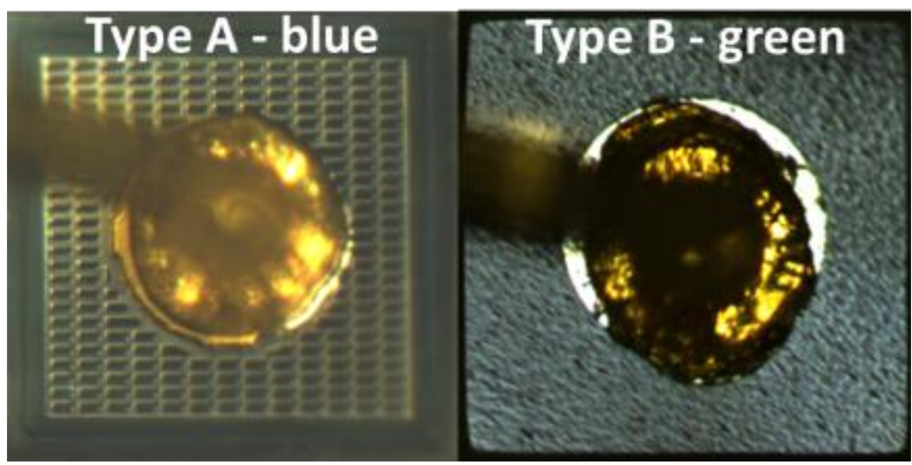

Figure 59: Picture of the chip surface of the two tested LED types

The ESD events were simulated by means of a Transmission Line Pulser (TLP) system; the operation of TLP is based on the charging/discharging of a transmission line. In this system, a high-voltage power supply charges a floating cable to a pre-determined voltage (V_{LINE}) which is then discharged into the Device-Under-Test (DUT). Each TLP measurement session consists in various reverse-bias pulses with incremented V_{LINE} from 0 V to the LED failure. Compared to other types of ESD testing methods, the Transmission-Line-Pulser allows a better control of the parameters of the current and voltage waveforms applied to the DUT and then it gives more detailed information on the failure mechanisms triggered by the ESD events. Furthermore, the rectangular shape of the TLP pulse allows to clearly identify any changes in the DUT impedance during the discharge.

During each pulse, an oscilloscope measures the voltage and current waveforms, while an high speed Electroluminescence (EL) camera (Andor Luca S) acquires the light emission during the discharge. After each pulse, the device conditions were monitored by the reverse current measurement (leakage current at -5 V) and by the EL-vs-current measurement carried out, again, with the Andor Luca S camera. Due to the differences in behavior of the two different LED types, the measurements results will be reported separately in the following sections.

5.3 Results on BLUE LEDs (Type A)

Figure 60 shows an example of the pulsed I-V characteristic during a TLP measurement on a Type A LED: it is evident that, at higher voltage levels (V_{LINE} >140 V), the current starts to linearly increase due to the reverse breakdown conduction mechanism. This rise continues until the device failure, which, in this case, happens around the pulse levels of 8 A - 240 V.

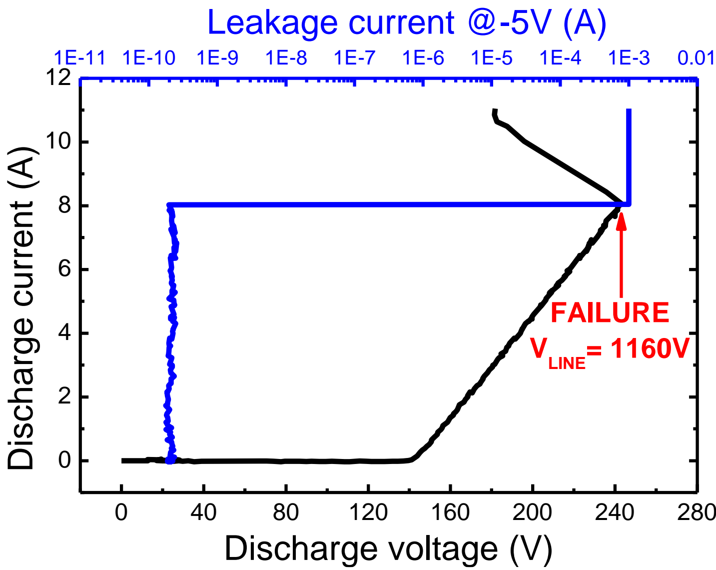

Figure 60: An example of the TLP measurement result on Type A LED. The black line represents the pulses I-V characteristic, while the blue line shows the trend of the leakage current at -5 V during the test.

The LED failure is identified by the instantaneous rise of the leakage current which indicates the generation of a low resistance path caused by the high power level reached during the pulse at V_{LINE} $=V_{CRIT} =$ 1160V. This behavior is also clearly visible in Figure 61.

The EL measurements reported in the small pictures inside the graph of Figure 61 and, for another sample in Figure 62, highlights that immediately after the catastrophic failure, a small portion of the chip surface start to emit light.

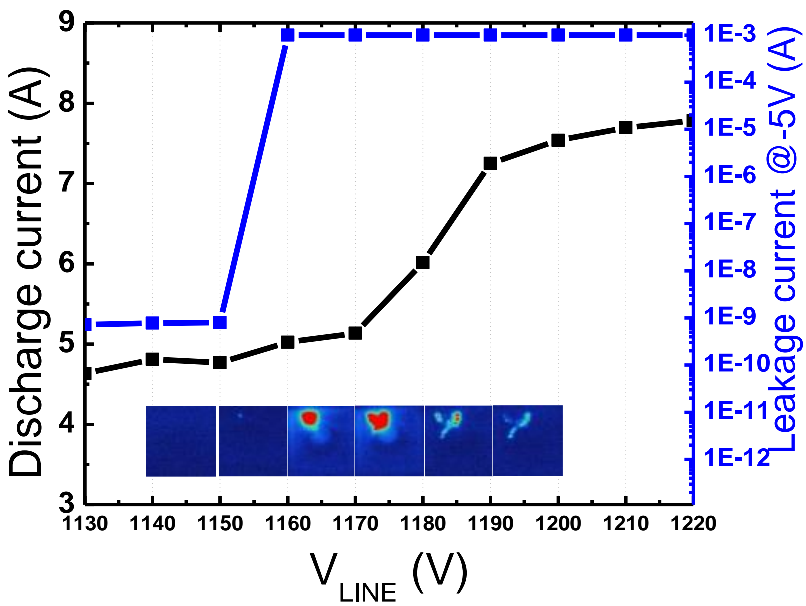

Figure 61: Comparison between the trends of the leakage current (blue line) and the discharge current (black line) corresponding to the example of Fig. 2. The small pictures shows the chip EL emission during the different pulses.

The subsequent pulses show an enlargement of the emitting area and a decrease in the emission intensity: this is a sign that, after the creation of the resistive path in the semiconductor lattice, the high-current flow limited to a small section of the chip, leads to the degradation of the surrounding region and then to the diffusion of the conductive path.

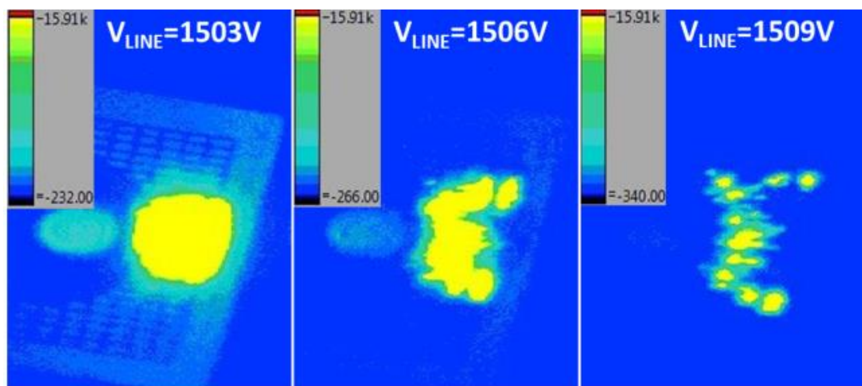

Figure 62: EL images of a Type A chip during catastrophic failure at three subsequent TLP pulses.

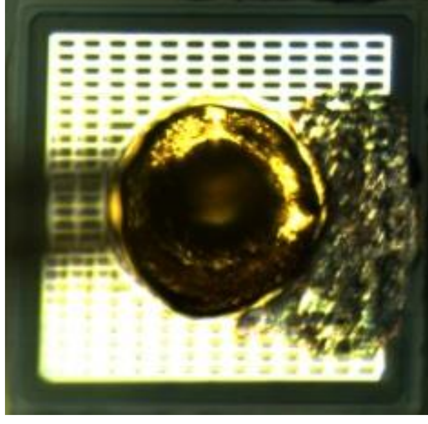

Figure 63: Image of the Type A LED after the TLP test showed in Figure 62.

As a consequence of this degradation mechanisms, the chip region interested by the current conduction melts as showed in Figure 63. This mechanisms is confirmed also by the analysis of waveform graphs of Fig. 6, which indicate that the exposure to ESD events with VLINE> VCRIT leads to a gradual decrease in the device impedance; this is well correlated to the increase in the size of the damaged area shown in Fig. 4.

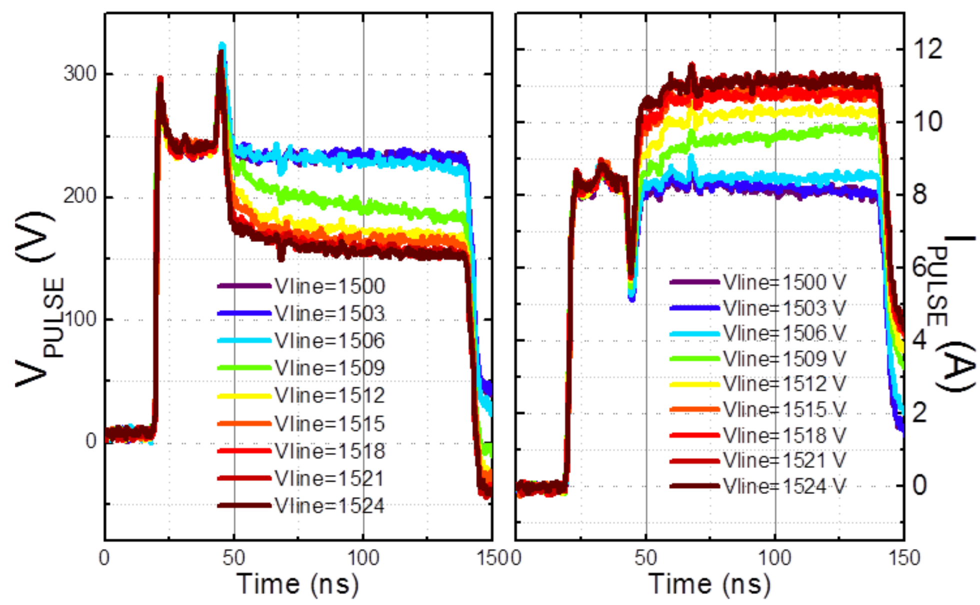

Figure 64: Voltage and current waveforms on a Type A LED during the pulses of Figure 62.

Despite the graduality of the impedance modifications showed by Figure 64, the optical characteristics of the Type A device results compromised already after the first pulse at V_{LINE}> V_{CRIT}: in fact, as visible in the example of Figure 65, the optical emission remains stable until the discharge at V_{LINE}=1160V and then it disappears, in correspondence to the increase of the leakage current. This explain that even the first, localized, generation of shunt paths is sufficient to bypass the whole active area of the chip and therefore leads to the instantaneous optical failure of the LED.

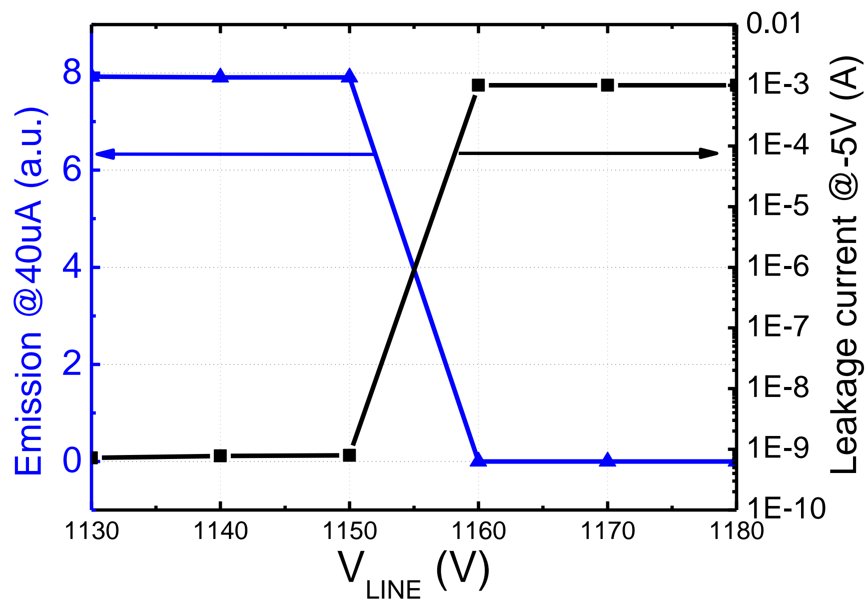

Figure 65: Comparison between the emission intensity (blue line) and the leakage current (black line) during the catastrophic failure of a Type A LED.

The EL analysis between each TLP pulse do not shows any modification neither in the emission intensity, nor in the emission surface profile before the destructive pulse.

5.4 Results on GREEN LEDs (Type B)

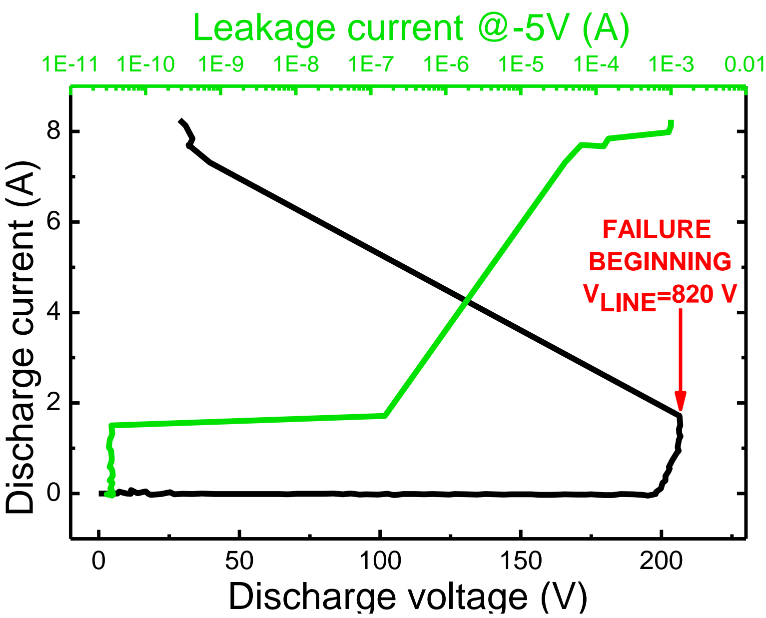

Figure 66: An example of the TLP measurement result on Type B LED. The black line represents the pulses I-V characteristic, while the green line shows the trend of the leakage current at -5 V during the test.

In Figure 66 is reported the pulsed I-V characteristic during a TLP test on a Type B (green) LED; in this graph it is evident the lower current level that this LED type can withstand with respect to the Type A LED of Figure 60. In fact at a reverse-current level below the 2 A the leakage current start to increase and then it reaches the maximum level after several pulses.

During the ESD events the EL images show very small emission spots, which, in most of the cases, are located on the chip perimeter (see Figure 67). Differently from Type A LEDs, on these samples there is a change in impedance even during the discharge itself, as visible in Figure 68.

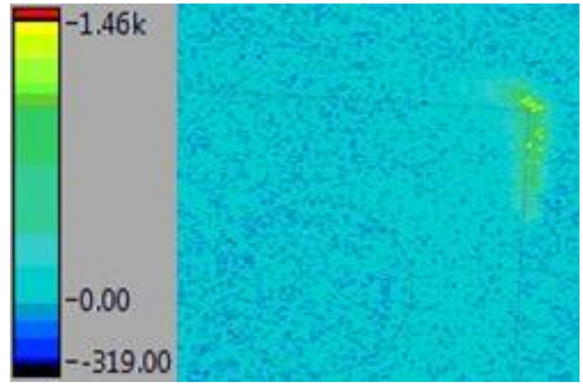

Figure 67: An example of EL image on a Type B LED (V_{LINE}=576V).

This earlier and gradual degradation is confirmed also by the graph of Figure 69, which shows that the optical emission degrades gradually, such as the leakage current increases.

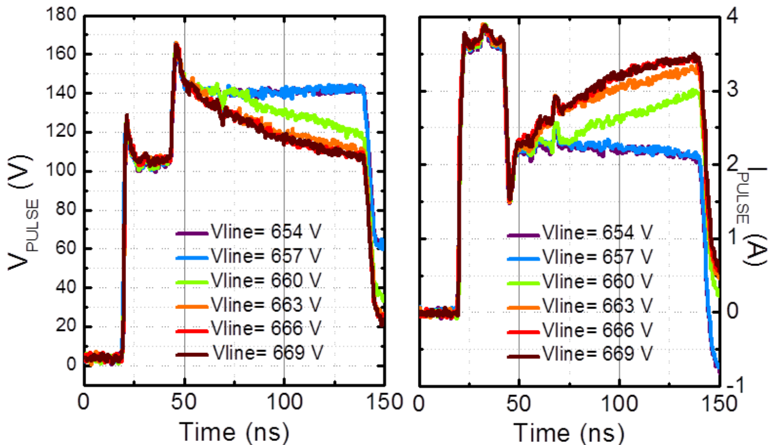

Figure 68: Voltage and current waveforms on a Type B LED during gradual failure at six subsequent TLP pulses.

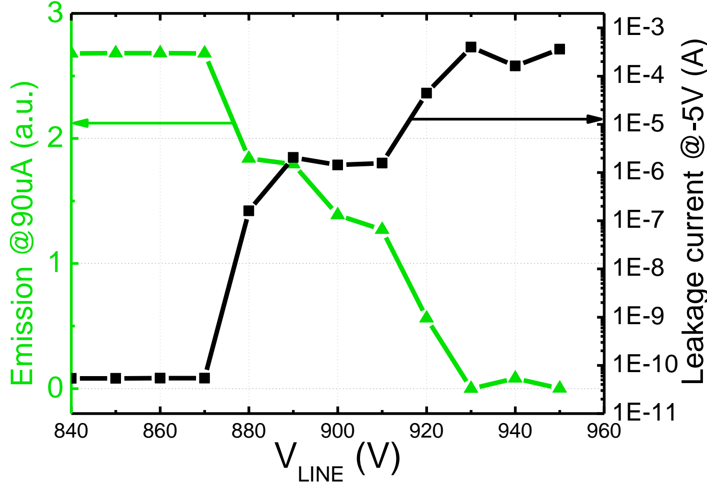

Figure 69: Comparison between the emission intensity (green line) and the leakage current (black line) during the catastrophic failure of a Type B LED.

5.5 Discussion and conclusion

The results of these tests have revealed different behaviors of the two LED types in terms of ESD robustness and degradation mechanisms. The BLUE LEDs (Type A) can withstand pulses with high power levels but a single ESD event can lead to the catastrophic failure of the device due to the generation of a shunt path, probably located in an area of the chip where the defects density is higher. The EL measurements during the TLP pulses shows that, after the destructive discharge, there is a precise area of the chip that emit light. The enlargement of the emitting area at subsequent pulses, such as the waveform analysis, confirms that the high current flow through the generated shunt path causes the degradation of the surrounding region and then to the diffusion of the conductive path.

On the other hand, Type B LEDs (GREEN) start to degrade at lower levels of TLP pulse, due to the higher defects density of the semiconductor lattice related to the higher Indium concentration. The results presented in this work indicate that the degradation mechanism of the Type B LED submitted to ESD events is gradual both in terms of electrical modifications and of optical emission decay.

The EL measurements indicate that, during a degrading ESD event, the defect-assisted current conduction happens more frequently along the chip perimeter. This is a sign that the high defect density at the edge of the chip affects significantly the ESD robustness of green LEDs with respect to the blue ones. The different configurations of the upper contact does not seem to affect the behavior of the devices submitted to reverse-bias ESDs.

This section has not only showed an interesting comparison between the ESD robustness of two different LED technologies, but also has proposed an innovative way to deeply investigate the failure mechanisms of light-emitting diodes submitted to electrical overstress events.

Chapter 6: Reliability of Remote Phosphor Light Sources

The aim of this chapter is to investigate the thermal stability of remote phosphor plates to be used in solid-state lighting systems, for the conversion of the blue light emitted by GaN-based LEDs into white light. A preliminary thermal characterization revealed that in normal conditions of blue light irradiance the phosphor plates can reach temperature levels higher than 60°C, which can affect both performance and reliability. The results of accelerated thermal stress tests indicate that high temperature levels can trigger a relevant degradation mechanism (estimated activation energy is 1.2 eV), that drastically reduces the phosphor conversion efficiency and modifies the photometric and colorimetric characteristics of the emitted white light.

6.1 Introduction

The introduction of white LEDs is driving a deep revolution in the lighting market; improved efficiency, excellent optical quality, versatility and reliability are only some of the advantages brought by this new technology. Most of the solid-state light sources for general lighting are based on phosphor-converted white LEDs: in this type of devices a InGaN blue LED is coated with a phosphorous layer (typically based on Yttrium Aluminum Garnet, YAG) which converts the blue light of the LED into a yellow emission. The combination of blue and yellow emission are perceived as white light by the human eye. While on one hand blue LED chips can have high reliability, on the other hand several reports have demonstrated that the package and phosphors of white LEDs can severely degrade during device lifetime. This is mainly due to the high temperature levels reached in proximity of the LED chip during operation [1].

For this reason, since 2005, the scientific community and the manufacturers of LEDs have begun to investigate the possibility of placing the phosphor layer far from the active region of the device; this led to the development of the so called "remote-phosphor" technology, which consists in depositing the phosphor materials onto a substrate (usually polycarbonate) placed some centimeters away from the LEDs. A typical remote-phosphor light source consists in a royal-blue (455nm) LED board, a light mixing chamber and a phosphor plate (see Figure 70). Remote-phosphor (RP) guarantees a good extraction efficiency, a reduction of the phosphors operating temperature and a better diffusion of the emitted light [2-4].

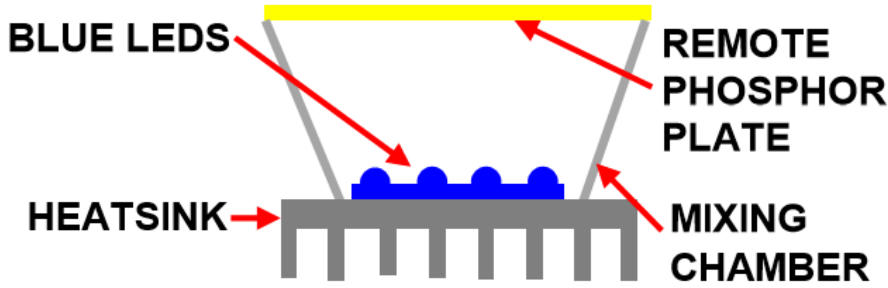

Figure 70: A schematic diagram of a typical Remote-phosphor light source.

Despite the increasing interest of the lighting market in the remote-phosphor technology, no report on the reliability of RP systems has been presented so far in the literature. The goal of this work is to report – for the first time – an extensive analysis of the thermal properties and degradation of remote phosphors for application in LED lighting: results provide information on the optical and thermal behavior of the samples, and on the degradation issues that arise at high temperature levels.

Results of thermal characterization indicate that – even in normal operating conditions - the remote-phosphor plates can reach temperature levels in excess of 60 °C, which can compromise the long-term performances of the lighting systems.

For this reason, a set of accelerated thermal stress tests was carried out with temperature levels between 85°C and 145°C. These tests revealed a significant, temperature-dependent, degradation mechanism that reduces the total luminous flux, and modifies the colorimetric characteristics of the phosphor-converted white light.

6.2 Experimental details

The remote-phosphor samples tested in this work are round plates (diameter = 61.5mm, thickness 2.1 mm) fabricated by a leading manufacturer. Combined with a royal-blue light source (usually emitting around 455nm) these plates produce a neutral white light with a Correlated Color Temperature (CCT) of 4000K and a Chromaticity Rendering Index (CRI) of 80.

The samples were submitted to thermal stress tests in climatic chambers at the following six temperatures: 85°C. 105°C, 115°C, 125°C, 135°C, 145°C; the highest temperature level has been chosen in order to not exceed the glass transition temperature of the involved materials; in fact the substrate material of the RP plates is polycarbonate, which has a glass transition temperature of 150°C. The atmosphere inside the chamber was air.

At the different stages of the stress tests, the plates were removed from the thermal chambers and placed in an appropriate test fixture equipped with royal-blue LEDs. This fixture was not submitted to any stress, so its optical characteristics were stable for the whole duration of the tests. The photometric parameters of the lighting system composed by LED fixture and remote-phosphor plates were measured at different current levels through a 65” integrating sphere equipped with an array spectro-radiometer. Thermal characterization was carried out by means of an infrared (IR) camera and a Cr-Al thermocouple placed inside the phosphor plate.

6.3 Results

6.3.1 Thermal characterization

5

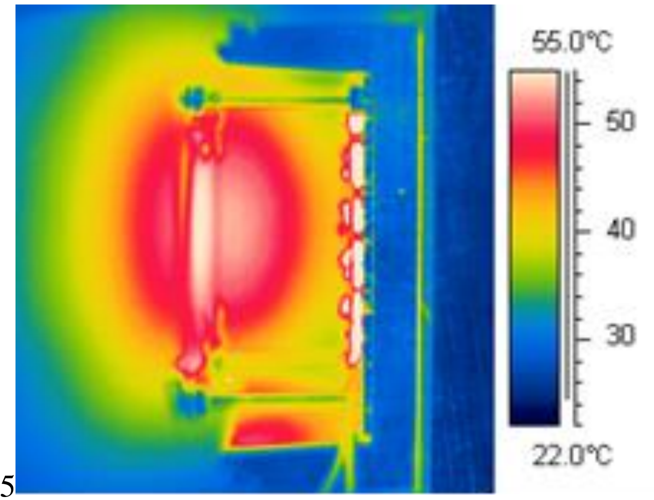

Figure 71: IR image of the phosphor plate submitted to an irradiance level of 316mW/cm^2.

Before the execution of the stress tests, the thermal characteristics of the phosphor plates were extensively evaluated: thermal measurements were executed by irradiating the phosphor plates with blue LED light (455 nm), with several irradiance levels. IR imaging (an example is reported in Figure 71) provided information on the distribution of heat on the phosphor plates, and indicated that – even during normal operation – there is a significant self-heating of the phosphor materials.

The fixture used for the thermal characterization (differently from that used for the photometric measurements) has no light mixing chamber: for this reason, the light and the thermal power emitted by the LEDs is not confined below the remote phosphor plates, and can escape from the side walls; for this reason it is plausible to consider that the self heating of the phosphors in more realistic operating conditions can be even stronger, compared to the measurements reported in this paper.

Information on the absolute temperature levels reached by the phosphors during operation was obtained by means of thermocouples, inserted within small holes in the phosphor plates (thermal coupling was realized by thermally conductive grease). In Figure 72 we report the results of this analysis: phosphor temperature shows a linear dependence on the luminous power of the LEDs used for the irradiation. It is worth noticing that, under relatively high irradiation levels, temperature can be in excess of 60 °C, and this, in principle, can limit the performance and the reliability of the materials.

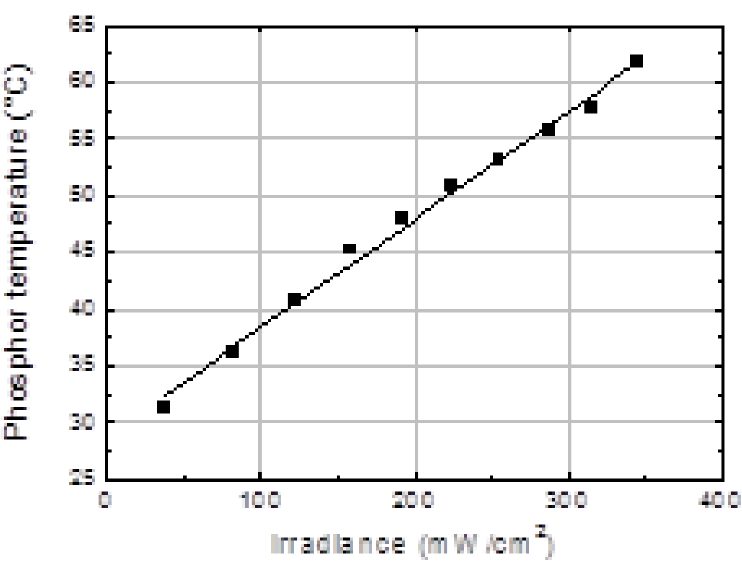

Figure 72: Thermocouple measurements as a function of the irradiance level. Solid line represent the linear fitting of the points.

6.3.2 Degradation tests

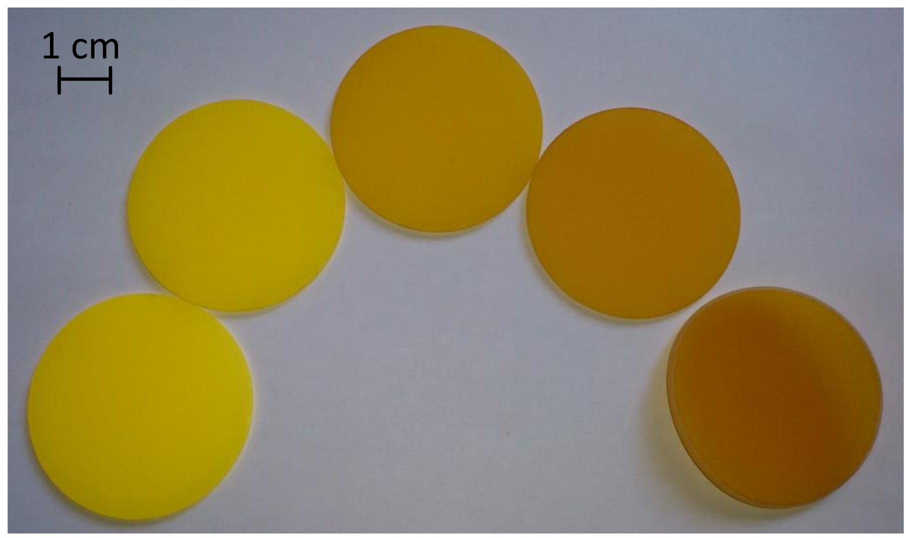

Figure 73: Picture of five remote-phosphor plates after 1000h of stress tests. Stress temperature (from left to right): 85°C, 105°C,125°C,135°C,145°C.

In Figure 73 we report a picture of a set of phosphor plates which were submitted to stress at different temperature levels. The effects of high temperatures on the physical aspect and chromatic properties of the phosphors are clearly visible: It is worth mentioning that the plate submitted to the 145°C after the first 1000 hours of stress tests is remarkably bent, such that – after stress - it does not fit the light fixture used for the measurements.

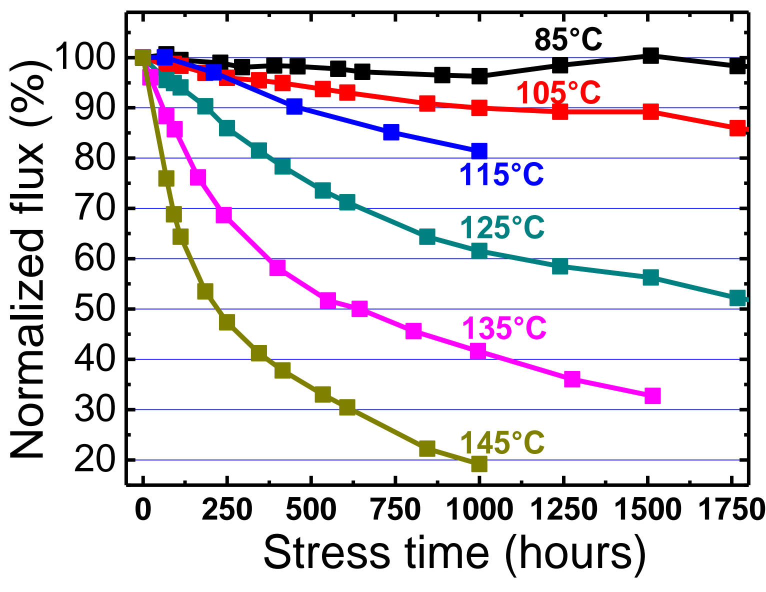

Figure 74: Normalized flux of the remote-phosphor lamp after the thermal stress tests on the phosphor plates.

A more quantitative description of the effects of thermal stress on the performance of the phosphors is given by Figure 74, which reports the degradation kinetics of phosphor plates submitted to stress at different temperature levels. As can be noticed, high temperature storage results into a decay of the emitted luminous flux of the lighting system, which leads, in a short time, to the end of the lamp's operating life. Degradation rate shows a significant dependence on the stress temperature level: from the Arrhenius plot of the TTF90% (Figure 75) it is possible to extrapolate an activation energy of Ea=1.2 eV.

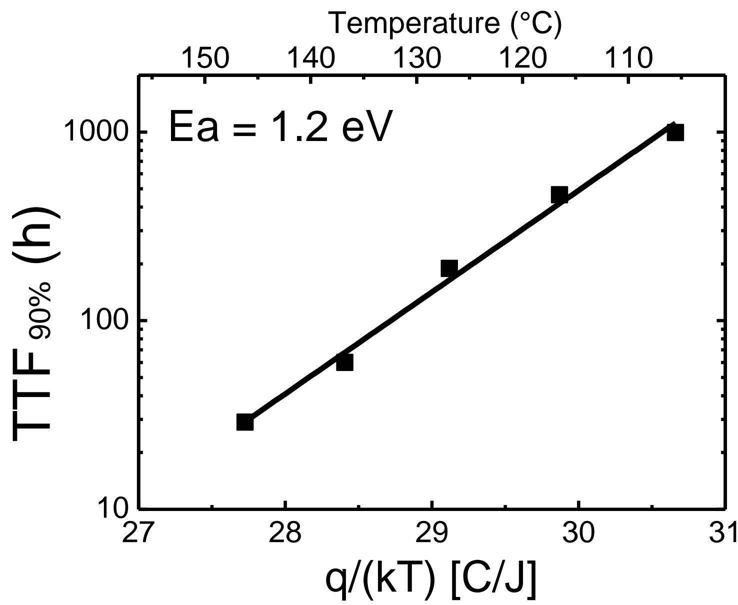

Figure 75: Arrhenius plot of the Time-to-Failure at 90% (TTF90%).

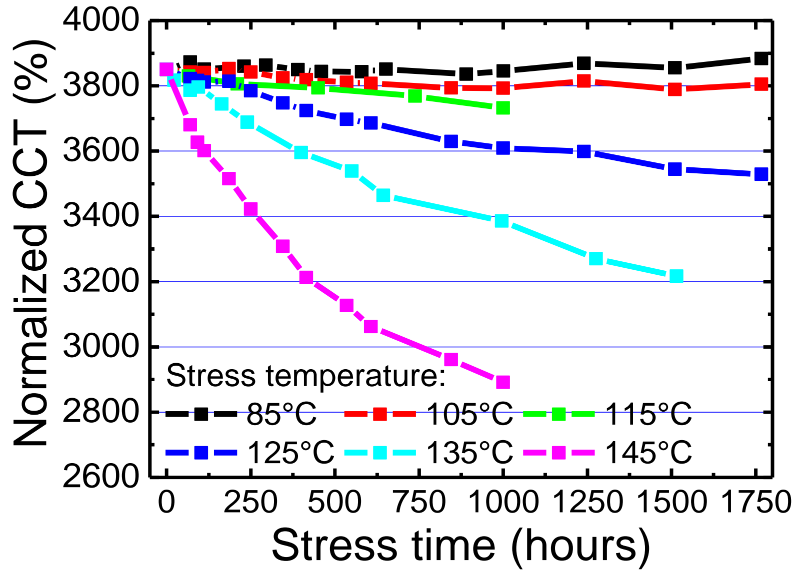

Figure 76: Correlated Color Temperature (CCT) during the reliability tests.

The decrease in the luminous flux is strongly correlated to the worsening of the chromatic properties of the phosphor plates: the photometric parameters were monitored during the stress tests and these measurements revealed significant changes also in the Correlated Color Temperature (CCT) and in the Chromaticity Coordinates (CIE x,y).

In Figure 76 we report the variation of CCT during stress time, for phosphor plates submitted to stress at different temperature levels. While at lower stress temperatures (85°C, 105°C), the Correlated Color Temperature does not show any strong change, stress tests at higher temperatures lead to a significant decay of the CCT. This phenomenon follows the same kinetics of the luminous flux decay and can therefore be ascribed to the thermally activated degradation mechanism discussed above. The drop in Color Temperature suggests that the degradation of the remote phosphor plates has consequences not only on the lighting extraction efficiency but also on the color of the emitted light.

These chromatic modifications is confirmed in the graph of Figure 77, which reports an example of variation of the Chromaticity Coordinates (CIE x,y) before and after 1000 hours of stress at 145°C. As visible from the colors on the background of the graph of Figure 8, light turns toward the red region of the chromaticity diagram.

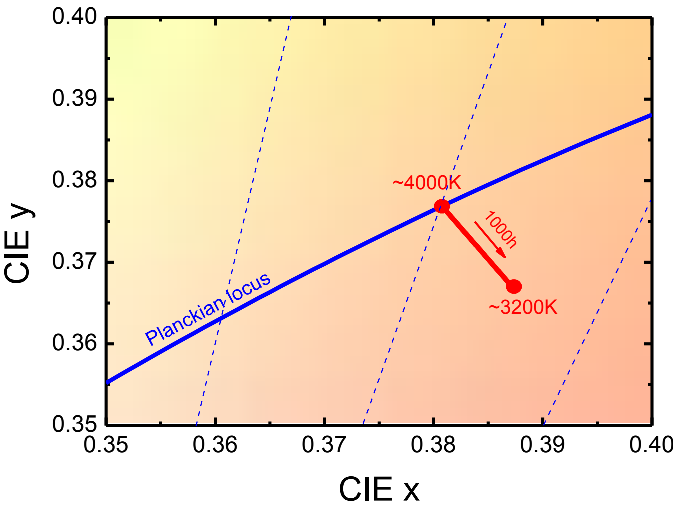

Figure 77: Chromatic variation before and after 1000 hours of 145°C thermal stress.

The analysis of the emitted spectra during degradation (see Figure 9) reveals that there is a significant decay both in the phosphor yellow emission and in the blue peak. This suggests that during thermal stress, the optical modifications are not related only to the decay of the phosphor conversion efficiency but also to a drop in the transmissivity of all the materials which form the plates.

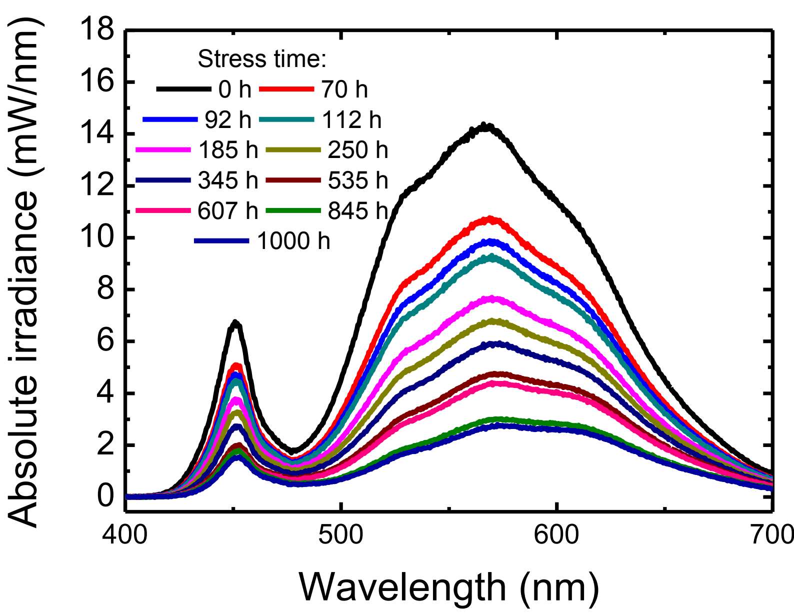

Figure 78: Emission spectra at 350mA during the 145°C stress test.

These considerations are extremely important in order to fully understand the nature of the reported degradation mechanisms, and leads to a more accurate investigation on the optical properties of the polycarbonate layer before and after the thermal stress tests.

With this purpose we mechanically removed the phosphor layer from two phosphor plates: one unstressed and one submitted to 1000 hours of 145°C thermal stress. This allowed us to evaluate the differences in the optical properties of the polycarbonate layer without the influence of the phosphor emission. Figure 79 shows two plates without phosphor: this picture clearly reveals that there is a significant difference in the appearance of the polycarbonate of the two samples. After the 145°C stress test, the polycarbonate appears darker and, obviously, the light transmissivity is drastically reduced.

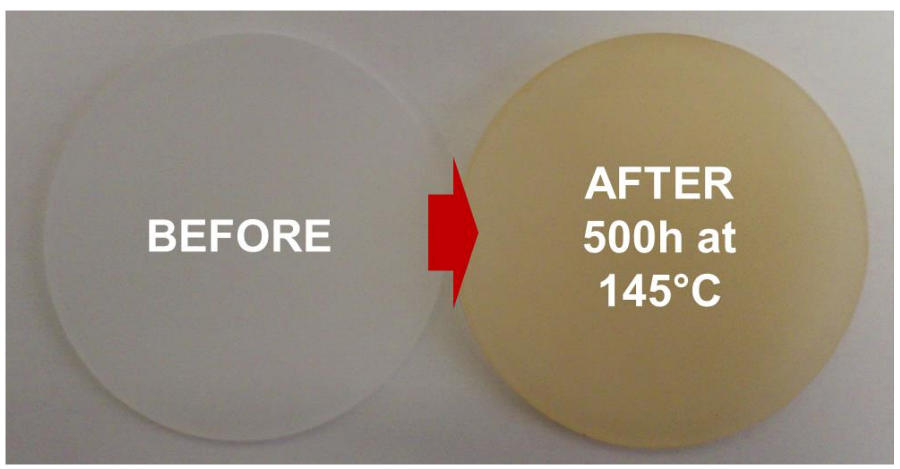

Figure 79: Picture of two remote phosphor plates without the phosphor layer. The right sample was submitted to 500 hours of 145°C thermal stress while the left sample was not submitted to any stress test.

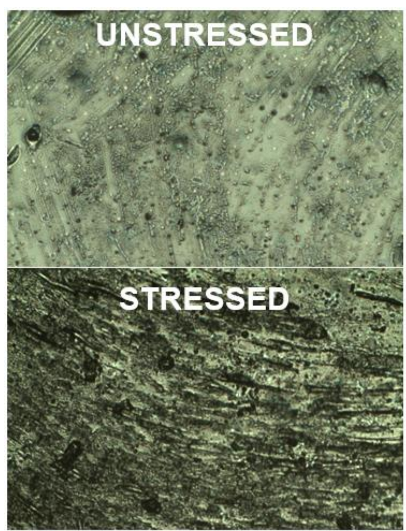

Figure 80: Images from metallographic microscope which shows the polycarbonate surface before and after the stress test at 145°C.

The differences in the appearance of the polycarbonate layers are even clearer in the microscopic images of Figure 80, which shows in detail the polycarbonate surfaces before and after the stress tests. These images confirm that after 1000 hours of thermal stress, the polycarbonate has become darker and the amount of light that crosses through its thickness is lower.

The contribution of the polycarbonate darkening to the optical degradation of the remote phosphor light source can be evaluated by comparing the optical decay trends with the remote phosphor plate and with the polycarbonate-only plate stressed at the same temperature. As visible in Figure 81 the optical power of the remote phosphor plate shows an initial exponential decay and then, after about 300 hours.

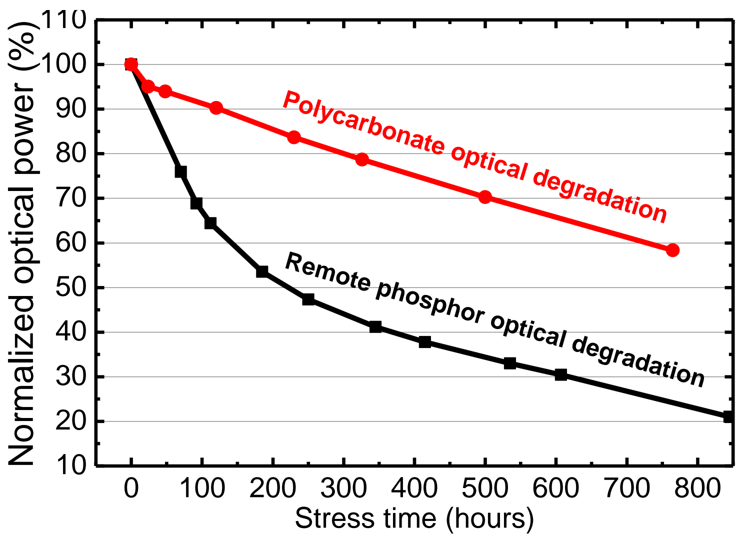

Figure 81: Comparison between the normalized optical power decay of the remote phosphor plate and of the polycarbonate plate stressed at 145°C.

6.4 Discussions and conclusions

Results therefore reveal that high temperature levels can trigger a degradation mechanism that reduces the efficiency of lighting devices based on the remote-phosphor technology. Although the remote phosphor approach is justified by the low temperature of the (remote) phosphor layers, results of thermal characterization reported at the beginning of this chapter highlight that in normal operating conditions remote-phosphor plates can reach temperature levels in excess of 60 °C. For this reason several accelerated thermal stress tests were carried out, in order to achieve information on the degradation kinetics, and to extrapolate device lifetime. Results indicate that the degradation mechanism is thermally activated, and has an activation energy of E_a=1.2 eV. From the Arrhenius plot in Figure 75 we extrapolated that at 85 °C the TTF90% is equal to 9000 h.

The detected degradation mechanism can significantly compromise the performances of light sources based on the remote-phosphor approach. In fact, after high temperature treatments on the phosphor plates, all the photometric and colorimetric parameters result changed. By the analysis of the emitted spectra during the tests (Figure 78) it is possible to conclude that degradation is due to a decay of the conversion efficiency of the phosphors, but also to a decrease in the transmissivity of the plastic materials of the plate. In fact, in Figure 78 both the 455nm blue peak and the broad phosphor emission have undergone to a dramatic decay.

After the phosphor removal the polycarbonate layer were analyzed through micrograph imaging (Figure 80): after the thermal stress tests the polycarbonate became significantly darker, and this determined a decrease in the light. This effect is clearly correlated with the optical degradation mechanisms reported in this paper. In order to separately evaluate the contribution of the polycarbonate degradation in the flux and CCT decay we have carried out several thermal stress tests on RP plates where the phosphor layers have been mechanically removed. The results of these tests allowed us to separately evaluate the contribution of the two different layers (polycarbonate and phosphors) on the optical degradation of the RP light source.

In summary, results reported in this chapter lead to the conclusion that, despite the excellent potential of the remote-phosphor approach, luminaire designers and LED lamp manufacturers must carefully consider aspects related to thermal management of the LED/Phosphor system, in order to avoid an excessive heating of the phosphor plates that can significantly limit lifetime and quality of their products.

References

[1] E. F. Schubert, Light Emitting Diodes, 2nd ed. Cambridge University Press, 2006.

[2] E. F. Schubert, L.-W. Tu, G. J. Zydzik, R. F. Kopf, A. Benvenuti, and M. R. Pinto, "Elimination of heterojunction band discontinuities by modulation doping,"Applied Physics Letters 60,466,1992.

[3] N. Hunt, E. F. Schubert, D. L. Sivco, A. Y. Cho, and G. J. Zydzik, "Power and efficiency limits in single-mirror light-emitting diodes with enhanced intensity," Electron. Lett. 28, 2169, 1992.

[4] B. E. A. Saleh and M. C. Teich, Fundamentals of Photonics, 2nd ed. Wiley,2007.

[5] R. S. Muller and T. I. K. with Mansun Chan, Device Electronics for Integrated Circuits, 3rd ed. Wiley, 2003.

[6] S. M. Sze, Semiconductor Devices: Physics and Technology, 2nd ed. John Wiley & Sons, Inc., 2001.

[7] M. Fukuda, Optical Semiconductor Devices. Wiley, 1999.

[8] X. A. Cao, J. M. Teetsov, M. P. Dévelyn, D. W. Merfeld, and C. H. Yan, "Electrical characteristics of AlGaN/GaN light-emitting diodes grown on GaN and sapphire substrates," Applied Physics Letters, vol. 85, pp. 7–9, 2004.

[9] V. Dmitriev, "GaN based p-n structures grown on SiC substrates," MRS Internet J. Nitride Semicond. Res., vol. 1, pp. 29–33, 1996.

[10] P. G. Eliseev, P. Perlin, J. Furioli, P. Sartori, J. Mu, and M. Osinski, "Tunneling current and electroluminescence in AlGaN:Zn, Si/AlGaN/GaN blue light emitting diodes," J. Electron. Mater., vol. 26, pp. 311–319, 1997.

[11] G. Franssen, E. Litwin-Staszewska, R. Piotrzkowski, T. Suski, and P. Perlin, "Optical and electrical properties of homoepitaxially grown multiquantum well AlGaN/GaN light emitting diodes," Journal of Applied Physics, vol. 94, no. 9, pp. 6122–6128, 2003.

[12] J. M. Shah, Y.-L. Li, T. Gessmann, and E. F. Schubert, "Experimental analysis and theoretical model for anomalously high ideality factors in Al- GaN/GaN pn junction diodes," Journal of Applied Physics, vol. 94, pp. 2627–2630, August 2003.

[13] Peter K. Kaiser, Robert M. Boynton, "Human Color Vision"; Optical Society of America, (1996).

[14] Ohno, Yoshi (2006), "Fifth Symposium "Optics in Industry"", in E. Rosas, R. Cardoso, J.C. Bermudez, O. Barbosa-Garcia, Proceedings of SPIE 6046, pp. 604625–1–604625–8

[15] Davis, Wendy; Ohno, Yoshi (December 2006), Color Rendering of Light Sources, NIST.

[16] Rea, M.S. and Freysinnier-Nova, JP. "Color rendering: A tale of two metrics," Color Research and Application, 33(3), 192-202 (2008).

[17] Alliance for Solid-State Illumination Systems and Technologies. "ASSIST recommends… Guide to Light and Color in Retail Merchandising," 8(1), (2010).

[18] Alliance for Solid-State Illumination Systems and Technologies. "ASSIST recommends… Recommendations for Specifying Color Properties of Light Sources for Retail Merchandising." 8(2), (2010).

[19] Pousset, Nicolas; Obein, Gael; Razet, Annick (2010), "Visual experiment on LED lighting quality with color quality scale colored samples", Proceedings of CIE 2010 : Lighting quality and energy efficiency, Vienna, Austria: 722–729.

[20] CIE (2007), Colour rendering of white LED light sources, Publication 177:2007, Vienna: CIE Central Bureau, ISBN 978-3-901906-57-2. Carried out by TC 1-69: Colour Rendering of White Light Sources.

[21] CIE Activity Report. Division 1: Vision and Color, pg.21, January 2008.

[22] Guo, Xin; Houser, Kevin W. (2004), "A review of colour rendering indices and their application to commercial light sources", Lighting Research and Technology 36 (3): 183–199.

[23] Smet KAG, Ryckaert WR, Pointer MR, Deconinck G, Hanselaer P. Correlation between color quality metric predictions and visual appreciation of light sources.

[24] Smet KAG, Ryckaert WR, Pointer MR, Deconinck G, Hanselaer P. Colour Appearance Rating of Familiar Real Objects. Colour Research and Application 2011;36(3):192–200.

[25] Dangol, R.; Islam, M.; Hyvärinen, M.; Bhusal, P.; Puolakka, M.; Halonen, L. (December 2013), "Subjective preferences and colour quality metrics of LED light sources", Lighting Research and Technology 45 (6): 666–688.

[26] R. Dangol, M.S. Islam, M. Hyvärinen, P. Bhusal, M. Puolakka, and Liisa Halonen. User acceptance studies for LED office lighting: Preference, naturalness and colourfulness. Lighting Research and Technology, December , 2013.

[27] ”Defect generation in InGaN/GaN light-emitting diodes under forward and reverse electrical stresses”; X.A.Cao, P.M. Sandvik, S.F. LeBoeuf, S.D. Arthur; Microelectronics Reliability 43 (2003) 1987–1991.

[28] “Kinetic model for degradation of light-emitting diodes”; Shun-Lien Chuang, Akira Ishibashi, Satoru Kijima,Norikazu Nakayama, Masakazu Ukita; IEEE Journal of Quantum Electronics, vol.33, no.6, June 1997.

[29] “Sixty thousand hour light output reliability of AlGaInP light-emitting diodes”; Patrick N. Grillot, Michael R.Krames, Hanmin Zhao, Seng Hup Teoh; IEEE transactions on device and materials reliability, vol.6, no.4, Dec.2006.

[30] "A Review on the Reliability of GaN-Based LEDs," Meneghini, M.; Trevisanello, L.-R.; Meneghesso, G.; Zanoni, E.,Device and Materials Reliability, IEEE Transactions on , vol.8, no.2, pp.323,331, June 2008

[31] “Reversible degradation of ohmic contacts on p-GaN for application in High-Brightness LEDs”; M. Meneghini,L. Trevisanello, G. Meneghesso, E. Zanoni; IEEE Trans. Electron Devices, vol.54, no.12, Dec. 2007.

[32] “High-temperature degradation of GaN LEDs related to passivation.”; M. Meneghini, L. Trevisanello, U.Zehnder, T. Zahner, U. Strauss, G. Meneghesso, E. Zanoni; IEEE Trans. Electron Devices, vol.53, no.12,pp.2981–2987, Dec. 2006.

[33] “Electrical, optical and thermal degradation of high power GaN/InGaN light-emitting diodes,”; J. Hu, L. Yang,and M. W. Shin; J. Phys. D, Appl. Phys., vol. 41, no. 3, p. 035 107, Feb. 2008.

[34] “Hydrogen plasma passivation effects on properties of p-GaN.”; A.Y. Polyakov, N.B. Smirnov, A.V. Govorkov, K.H. Baik, S.J. Pearton, B. Luo, F. Ren, J.M. Zavada; J.Appl.Phys., vol.94, no.6, pp.3960–3965, Sep. 2003.

[35] “Study of degradation mechanism of blue light emitting diodes.”; A. Uddin, A.C. Wei , T.G. Andersson; Thin solid Films; Jul. 2005.

[36] “Degradation mechanisms of GaN-based LEDs after accelerated DC current aging.”; G. Meneghesso, S. Levada, R. Pierobon, F. Rampazzo, E. Zanoni, A. Cavallini, A. Castaldini, G. Scamarcio, S. Du, and I. Eliashevich, IEDM Tech. Dig., 2002, pp. 103–106.

[37] “Low-frequency noise sources in as-prepared and aged GaN- based light-emitting diodes.”;Bychikhin, S.;Pogany, D.; Vandamme, L. K. J.; Meneghesso, G.; Zanoni, E.; Journal of Applied Physics , vol.97, no.12,pp.123714-123714-7, Jun 2005.

[38] “Stability and performance evaluation of high-brightness light-emitting diodes under DC and pulsed bias conditions.”; M. Meneghini, L. Trevisanello, S. Podda, S. Buso, G. Spiazzi, G. Meneghesso, and E. Zanoni, Proc. SPIE, vol. 6337, p. 633 70R, 2006.

[39] ”Reliability of visible GaN LEDs in plastic package"; Meneghesso G., Levada S. and Zanoni E., et al. , Microelectronics Reliability, Vol. 43, pp.1737-1742, (2003).

[40] "Failure analysis of plastic packaged optocoupler light emitting diodes"; Hwang N., Naidu P. S. R., and TriggA. , Electronics packaging technology, 5th conference, pp. 346-349, (2003).

[41] "Sulfur contamination of high power white LED"; Mura G., Cassanelli, and Fantini, F., et al. , Microelectronics Reliability, Vol. 48, pp.1208-1211, (2008).

[42] "The role of temperature and operating current in limiting reliability of white LEDs."; M. Dal Lago, DegreeThesis, Dec.2009.

[43] "High temperature electro-optical degradation of InGaN/GaN HBLEDs" ; M. Meneghini, L. Trevisanello, C.Sanna, G. Mura, M. Vanzi, G. Meneghesso and E. Zanoni; Microelectronics Reliability, Volume 47, Issues 9-11,September-November 2007, Pages 1625-1629.

[44] "LUXEON LED Assembly and Handling Information", Philips Lumileds, Application Brief AB32, http://www.philipslumileds.com/uploads/252/AB32-pdf

[45] M. Dal Lago, M. Meneghini, N. Trivellin, G. Meneghesso, E. Zanoni, "Degradation mechanisms of high-power white LEDs activated by current and temperature", Microelectronics Reliability, Volume 51, Issues 9–11, September–November 2011, Pages 1742-1746.

[46] T. Yanagisawa, Estimation of the degradation of InGaN/AlGaN blue light-emitting diodes, Microelectronics Reliability, Volume 37, Issue 8, August 1997, Pages 1239-1241.

[47] A. Uddin, A.C. Wei, T.G. Andersson, "Study of degradation mechanism of blue light emitting diodes, Thin Solid Films", Volume 483, Issues 1–2, 1 July 2005, Pages 378-381.

[48] Cree® XLamp® LED Electrical Overstress http://www.cree.com/xlamp_app_notes/electrical_overstress

[49] Osram "The Basic Principles of Electrical Overstress (EOS)" http://www.osram-os.com/Graphics/XPic0/00091442_0.pdf/The%20Basic%20Principles%20of%20Electrical%20Overstress%20(EOS).pdf

[50] Jiajie Fan; Kam-Chuen Yung; Pecht, M., "Lifetime Estimation of High-Power White LED Using Degradation-Data-Driven Method," Device and Materials Reliability, IEEE Transactions on , vol.12, no.2, pp.470,477, June 2012

[51] Meneghini, M.; Dal Lago, M.; Trivellin, N.; Meneghesso, G.; Zanoni, E., "Degradation Mechanisms of High-Power LEDs for Lighting Applications: An Overview," Industry Applications, IEEE Transactions on , vol.50, no.1, pp.78,85, Jan.-Feb. 2014

[52] M. Pavesi, M. Manfredi, F. Rossi, M. Meneghini, G. Meneghesso, and E. Zanoni, "Implications of changes in the injection mechanisms on the low temperature electroluminescence in InGaN/GaN light emitting diodes", J. Appl. Phys., Vol. 103, pp. 024503 -1-5, 2008

[53] M. Meneghini, L.-R. Trevisanello, U. Zehnder, G. Meneghesso, and Enrico Zanoni, "Reversible degradation of ohmic contacts on p-GaN for application in high brightness LEDs", IEEE Transaction on Electron Devices, vol. 54, no. 12, pp. 3245 - 3251, 2007

[54] M. Meneghini, A. Tazzoli, R. Butendeich, B. Hahn, G. Meneghesso, and E. Zanoni, "Soft and Hard Failures of InGaN-Based LEDs Submitted to Electrostatic Discharge Testing", IEEE Electron Device Letters, vol. 31, no. 6, pp. 579-581, 2010

[55] Y. K. Su, S. J. Chang, S. C. Wei, S.-M. Chen, and W.-L. Li, "ESD engineering of nitride-based LEDs," IEEE Transactions on Device and Material Reliability, vol. 5, no. 2, pp. 277–281, June 2005
[56] M. Meneghini, A. Tazzoli, E. Ranzato, G. Meneghesso, and E. Zanoni, R. Butendeich, U. Zehnder, B. Hahn, "Failure of GaN-based LEDs submitted to reverse-bias stress and ESD events", IRPS2010, International Reliability Physics Symposium, May 2-6, 2010 Anaheim, California, pp.522-527, ISBN: 978-1-4244-5431-0
[57] M. Meneghini, A. Tazzoli, G. Mura, G. Meneghesso, and E. Zanoni, "A review on the physical mechanisms that limit the reliability of GaN-based LEDs", IEEE Transactions on Electron Devices vol. 57, no. 1, pp. 108-118, 2010